UNIVERSITÀ DEL SALENTO

DEPARTMENT OF MATHEMATICS AND PHYSICS “E. DE GIORGI”
PhD in Physics and Nanoscience

The PADME experiment and the extraction of annihilation cross section

Candidate:
Isabella Oceano

Advisors:
Prof.ssa Stefania Spagnolo
Dott. Gabriele Chiodini

Academic year 2020-2021

Contents

1

Annihilation cross section measurement

The annihilation in two photons is a very important SM candle process for PADME. Gaining a good knowledge of this process allows to monitor with a physics candle the energy scale, the number of positrons hitting the target and detector geometry. In addition, it allows to exercise on a easy test case the strategy to fight the background for the dark search. The signature of this process in the experiment consists in the presence of two photons in the electromagnetic calorimeters. Since the SAC detector is overwhelmed by Bremsstrahlung photons, only the main calorimeter, ECAL, is used to perform this analysis. The goal of this study is to measure the cross section of $e^+e^- \to \gamma\gamma$ using the data collected by the experiment during RunII. In this chapter the entire strategy is described, including a very important and challenging step that is measurement of the efficiency. The technique applied is first described, then validated on dedicated MC samples and applied to data. Nowadays no measurements of the cross section exist at the PADME energy scale. A small review on the two photons annihilation cross section measurement at energies close to $\sqrt{s} =\sim 21$ MeVis given in Appendix ??.

1.1 The cross section measurement strategy

The total cross section, σ_T, for the process $e^+e^- \to \gamma\gamma(\gamma)$ can be measured in PADME using the following relation:

$$\sigma(e^+e^- \to \gamma\gamma) = \frac{N_{sig}}{N_{POT} \times N_{\frac{e}{S}} \times A \times \epsilon} \tag{1.1}$$

where

- N_{sig} is the number of signal processes observed after a selection based on the kinematic correlations typical of annihilation events once subtracted of the background component. In this thesis work several selection procedures for the annihilation process have been considered. In addition to searches based on the identification of a pair of photons, event selection using only one photon have been studied. The choice among the various possibilities has been taken balancing the difficulty in estimating the background from physics process and from spurious beam interaction and the difficulty in evaluating the overall selection efficiency;

- N_{POT} is the total number of positrons hitting the target measured with the active Diamond target;

- $N_{\frac{e}{S}}$ is the number of atomic electrons per unit surface in the PADME target. It is estimated as $N_{\frac{e}{S}} = \frac{\rho \times N_A \times Z \times d}{M_w} = 0,0105\ \mathrm{b}^{-1}$, where $\rho = 3,52\ \mathrm{g/cm}^3$ is the Diamond density, N_A is the Avogadro number, Z the atomic number, $d = 100\ \mu$m is the target thickness and M_w is the atomic weigh;

- A is the acceptance of the PADME detector and of the selection criteria applied. Therefore, it results from both geometric and kinematic constraints. The determination of the acceptance will be describen in Section 1.5.1. The acceptance allows to relate the total cross section σ_T to the so called fiducial cross section σ_F, corresponding to the fraction of the cross section directly visible in the experimental apparatus and lying within the kinematic selection requirements $\sigma_T = \sigma_F/A$;

- ϵ is the overall efficiency to identify signal processes. It represents the combination of the detection efficiency of the PADME calorimeter. the photon reconstruction and identification efficiency for both photons and the event selection efficiency. Therefore, when N_{sig} is measured with a selection requiring two photons in ECAL, the efficiency ϵ is the product of the identification efficiencies, $\epsilon(\gamma_1)$ and $\epsilon(\gamma_2)$ of the two photons.

Detector defects and asymmetries often prevent the performance of photon reconstruction algorithms to be uniform. Therefore, the event efficiency varies depending on the regions of the detector where the photons have been detected and, in general, the efficiency ϵ cannot be applied as a constant term in Eq. 1.1, unless it is estimated as an average value over the data sample.

Several procedures can be applied to generalize 1.1 taking into account these problems. An approach consists in measuring the fiducial cross section as follows:

$$\sigma_F = \sigma(\theta_0 < \theta_{\gamma_{1,2}} < \theta_1) = \frac{\sum W_i - N_{bkg}}{N_{POT} \cdot n_{\frac{e}{S}}} \tag{1.2}$$

Each candidate contributes to the counting with a weight accounting for all the efficiency factors that determine the probability of such event to be selected. N_{bkg} is the estimated background contaminating the sample of selected events. For the candidate annihilation event i, the weight W_i is given by the inverse probability to identify the two photons in the event:

$$W_i = P^{-1}(\theta_{\gamma_{i_1}}, \theta_{\gamma_{i_2}}) = [A_{eff}(\theta_{\gamma_{i_1}}, \theta_{\gamma_{i_2}}) \times \epsilon(\theta_{i_1}, \phi_{i_1}) \times \epsilon(\theta_{i_2}, \phi_{i_2})]^{-1} \tag{1.3}$$

where $\epsilon(\theta_{i_{1,2}}, \phi_{i_{1,2}})$ is the efficiency as a function of the position in the calorimeter for the first or second photon. The factor $A_{eff}(\theta_{\gamma_{i_1}}, \theta_{\gamma_{i_2}})$ is the visible acceptance and it represents a correction to the acceptance that takes into account resolution effects causing the migration of events from the acceptance region to the outside and vice versa. It will be discusses in more details and estimated in Section 1.5.2.

The efficiency values used in Eq. 1.2 can be estimated with simulation or can be directly measured in data if a suitable sample of reference photons can be defined and used to measure the fraction of them that is successfully detected and identified. Section reference describes that data-driven determination of the efficiency that is used in the cross section measurement, exploiting the approach of Eq. 1.2.

Data-driven efficiency measurements may be affected by biases. On the other hand, simulations are often affected by residual mismodeling of the detector response and geometry and of the beam features. Another strategy, meant to address these problems, consists in estimating the reconstruction and selection efficiency in a simulation corrected for data mismodeling. In practice, this is done by replacing ϵ in Equation 1.1 with a global efficiency factor C corresponding to the ratio of simulated to generated events inside the fiducial requirements corrected for mismodelling. The corrections are defined in terms of scale factors equal to the ratio between the event dependent efficiency measured in data $\epsilon^{data}(\theta, \phi)$ and in simulation $\epsilon^{MC}(\theta, \phi)$, the latter being obtained with exactly the same method applied in the case of data. In summary,

$$\sigma_F = \frac{N_{sel}}{C \cdot N_{POT} \cdot n_{\frac{e}{S}}}, \tag{1.4}$$

$$C_{\gamma\gamma} = \frac{N_W^{MC,gen}(\theta_{min} < \theta_{\gamma_1,\gamma_2} < \theta_{max})}{N^{gen}(\theta_{min} < \theta_{\gamma_1,\gamma_2} < \theta_{max})}, \tag{1.5}$$

$$N_W^{MC,gen}(\theta_{min} < \theta_{\gamma_1,\gamma_2} < \theta_{max}) = \sum_i f_i^{data/MC}, \tag{1.6}$$

$$f_i^{data/MC} = \prod_j f_{i,j}^{data/MC} \tag{1.7}$$

where $f_{ij}^{data/MC}$ is the data-simulation scale factor for any efficiency contribution, for example the efficiency for photon 1 in event i leads to a scale factor $f_{i1} = \epsilon_{DD}^{data}(\theta_1, \phi_1)/\epsilon_{DD}^{MC}(\theta_1, \phi_1)$, where the efficiency $\epsilon_{DD}^{data}(\theta_1, \phi_1)$ is measured with a data driven (DD) method both in data and in Monte Carlo. The quantity N_W^{MC} therefore represents the number of signal events selected in the simulation, but corrected for local mismodelling of data, and N^{gen} is the number of simulated signal events that at generator level fall in within the acceptance of the selection. Finally, the factor C would correspond to purely MC based efficiency for the selection if all scale factors were equal to 1.

In this work the cross section measurement will be derived using Equation 1.1, and Equation 1.2 as a cross check, relying on a data-driven determination of the photon selection efficiency. The possible biases of the methods are studied in dedicated simulations and found to be negligible or mitigated by compensation effects. This topic will be discussed in Section reference where the cancellation due to compensation effects will be described and in Section reference where a careful implementation of the data driven method will be shown to leave no sign of biases.

The second approach based on scale factors was also investigated and found to be a powerful methodology to validate the strategy for the data-driven efficiency measurement. However, it was not used for the measurement due to the unavailability of suitable simulation of the PADME beam line.

1.2 Theory prediction

1.3 Data sample, simulation and reconstruction

1.3.1 Data sample

The data used for this measurement have been chosen among the sample collected during RunII, because of the smallest background level, as seen in Chapter data taking. During this run the energy of the beam was $E_{beam} = 430$ MeV and the beam density ~ 100 POT/ns. A summary of the runs used for the analysis with their main features is collected in Table 1.1. The total number of positrons on target corresponding to the sample is $N^{tot}_{POT} = 3,97 \times 10^{11}$. In Figure 1.1 structure in time of the bunch is shown. As highlighted by Table and Figure the runs have different features not only in multiplicity per bunch but also in bunch structure, meaning that the runs are collected with different beam configurations. This selection of runs was chosen because of a good stability of the beam intensity in time within the each run. Indeed a data quality monitor processing of the data shows that the number of positrons on target measured by the Diamond is very stable as is shown in Figure 1.2 for run $N = 30617$.

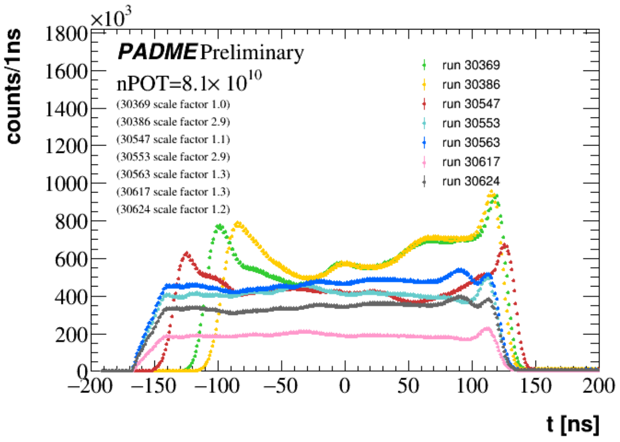

Figure 1.1: *Bunch structure for each run analysed recorded with SAC.*

A special data sample consisting of two runs, recorded with the target out of the beam line, has also been used. This sample allows to study the beam related background observed in PADME .

With a total of $N_{POT} = 4 \times 10^{11}$, assuming a product of acceptance and efficiency of the order of $\sim 5\%$ the number of detected annihilation events is about ~ 521000; if background was negligible or compatible with the signal, the relative statistical error on the cross section measurement would be $\sim 1\%$ and even if the background rate was ten times larger than

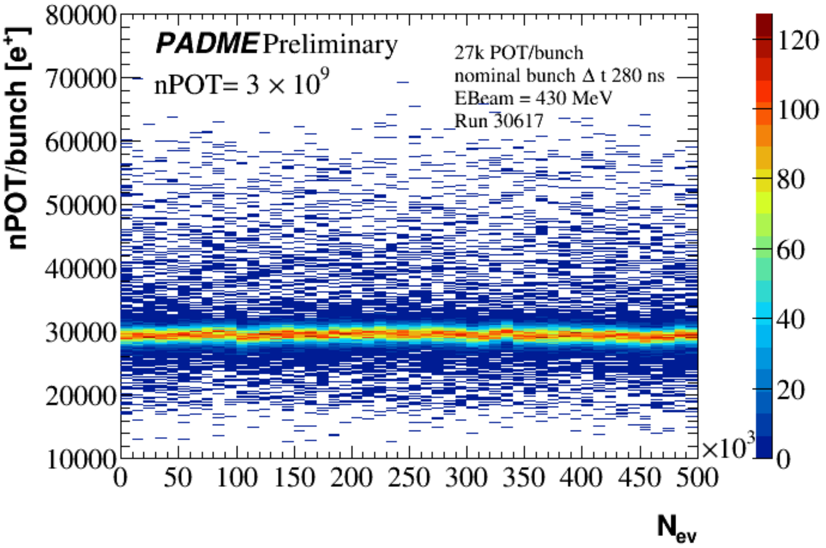

Figure 1.2: *Number of positrons per bunch as a function of the event number for run* 30617*.*

Table 1.1: *Main features of the analysed runs: run number, total N_{POT} measured by target, mean and sigma of a gaussian fit to the peak of the N_{POT} distribution, bunch length and month of data taking.*

Run number	$N_{POT}/10^{10}$	$\mu(N_{POT})$	$\sigma(N_{POT})$	bunch length [ns]	Date	
30369	$8,2$	26993	1738	260	Sept	
30386	$2,8$	19057	1385	240	Sept	
30547	$7,1$	31480	1402	270	Oct.	
30553	$2,8$	35729	1314	260	Oct.	
30563	$6,0$	26785	1231	270	Oct.	
30617	$6,1$	27380	1496	270	Nov.	
30624	$6,6$	29515	2070	270	Nov.	
30654	/	~ 27000	/	~ 270	Nov.	no target
30662	/	~ 27000	/	~ 270	Nov.	no target

the signal, the statistical uncertainty would be $\leq 1\%$ which is unlikely to be larger than the systematic uncertainties affecting the measurement. Therefore the sample selected is adequate in size to the measurement.

1.3.2 Simulation samples

The PADME MC is based on a GEANT4 [?] simulation of the experimental apparatus and of the beam. Annihilation processes are simulated when the positrons of the beam cross the Diamond target along with the other dominant QED processes: Bremsstrahlung in particular, Bhabha scattering, and others minor effects. However, similarly to what happens in PADME, a large number of positrons per bunch must be simulated in order to achieve a reasonable statistics of annihilation processes, therefore the final state from a $e^+e^- \to \gamma\gamma$ event often overlaps with other photons in the the calorimeter, and moreover, the signal photons are not labelled to be easily distinguished. In order to study the kinematics of annihilation events either in a background free simulation, or flagging the final state particles, the CalcHEP generator was used. From the $e^+e^- \to \gamma\gamma$ generation, a text file was saved with the four-momenta of all particles involved in the process. A special functionality in PADMEMC allows to plug the two photons from an event generated by CALCHEP in a point of the target where a positron from the incoming beam is killed. The photons are then propagated through the detectors like any particle managed by GEANT4.

Several MC data samples were used across the analysis:

1. CalcHEP event generator samples, used to study the MC truth and generator level properties;

2. CalcHEP samples simulated with PADMEMC with a beam consisting of a single positron. In this case the final state of each event contains only two photons from e^+e^- annihilation that can fall inside or outside the detector geometrical acceptance;

3. CalcHEP samples simulated with PADMEMC as in case two but with a beam of 25×10^3 positrons in average in a bunch. This kind of simulation allows to investigate the effect of pileup of the signal event with physics background processes originated from beam interactions in the target.

The CalcHEP generator performs all calculations in the LO approximation for the final state selected by the user, that can be in our case, $\gamma\gamma$ or $\gamma\gamma\gamma$. The same techniques was used to plug annihilation events generated by Babayaga at the NLO approximation in the PADME MC. Therefore a Babayaga generation output at LO was used to check the consistency with CalcHEP and another generation at NLO was used to evaluate the acceptance of the annihilation.

1.3.3 Event reconstruction

The selection of annihilation events uses only the PADME BGO electromagnetic calorimeter. Therefore, here a brief reminder of the main features of the reconstruction of clusters in ECAL is given, while an extensive description of the algorithms is given in Chapter reference.

The multi hit reconstruction, described in Chapter ?? Section ??, was used. For each waveform up to three hits can be identified, with energy and time estimated with a fit with a signal template obtained from clean waveforms recorded in a single positron run. The template allows to naturally account and correct for problems related to the data acquisition like the limited acquisition time window and the saturation. For signals where only one hit is identified in the waveform, energy and time determination follow the same logic applied in the single hit reconstruction, described in Chapter ?? Section ??.

Once the hit collection is defined, clusters are reconstructed merging hits in nearby crystals in time coincidence. The energy required for the cluster seed is 20 MeV, while hits contributing to the cluster must have energy above 1 MeV, a distance from the seed not exceeding three crystals, and a maximum distance in time from the seed of 6 ns.

The cross section measurement requires the determination of the number of POT. This was estimated using the calibration procedure described in Section verify that in padme chapter there is the description. This procedures rely on the absolute energy calibration of the BTF calorimeter that is verified to 5%. The systematic uncertainty on the N_{POT} measurement arises from the calibration procedure, and can be assessed by studying the stability and consistency with the energy seen in other detectors, in particular in the SAC, that collects all forward Bremsstrahlung photons produced by interactions of the beam in the target.

1.4 Experimental signature of annihilation events

The selection of annihilation processes is based on the constrained photon-photon kinematics. In the assumption of a final state consisting of exactly two photons sharing the energy and momentum of the initial state, several relationships between the energies E_1 and E_2, the polar angles[1] θ_1, θ_2, and the azimuthal angles[2] ϕ_1, ϕ_2 of the photons, can be exploited. The most relevant of them are listed in the following, adopting the convention of using the the index 1 for the most energetic photon in the pair:

1. the sum of the energies E_1+E_2 is equal to the beam energy with very good approximation;
2. the transverse momenta of the photons are back to back, therefore $\phi_1 + \pi = \phi_2$
3. for each photon the polar angle θ is a function of the energy;
4. As a consequence of properties 1 and 3 the polar angle of the two photons are strictly correlated;
5. The previous considerations also imply that knowing E_1 sets the value the polar angle of the second photon θ_2; the same is true if the role of the two photons is exchanged;
6. The momentum balance implies also the following relation between the coordinates of the impact point of the two photons in a transverse plane

$$x(y)_{CoG} = \frac{x(y)_1 E_1 + x(y)_2 E_2}{E_1 + E_2} \sim 0. \tag{1.8}$$

In Figure 1.3 the correlation between the energy and the polar angle θ of the two photons is reported along with the two photons energy correlation and the distance in ϕ between a photon and the other extrapolated in the backward direction. Figure 1.4 shows the X and Y center of gravity for a sample specify sample used are also reported.

---

[1] The polar angle θ is defined as the angle between the photon direction and the z axis of the PADME reference frame, which is assumed to match the direction of the incoming positron beam.

[2] The azimuthal angle ϕ is the angle between the direction of a photon in the plane perpendicular to the beam and a reference axis conventionally chosen to be the x axis.

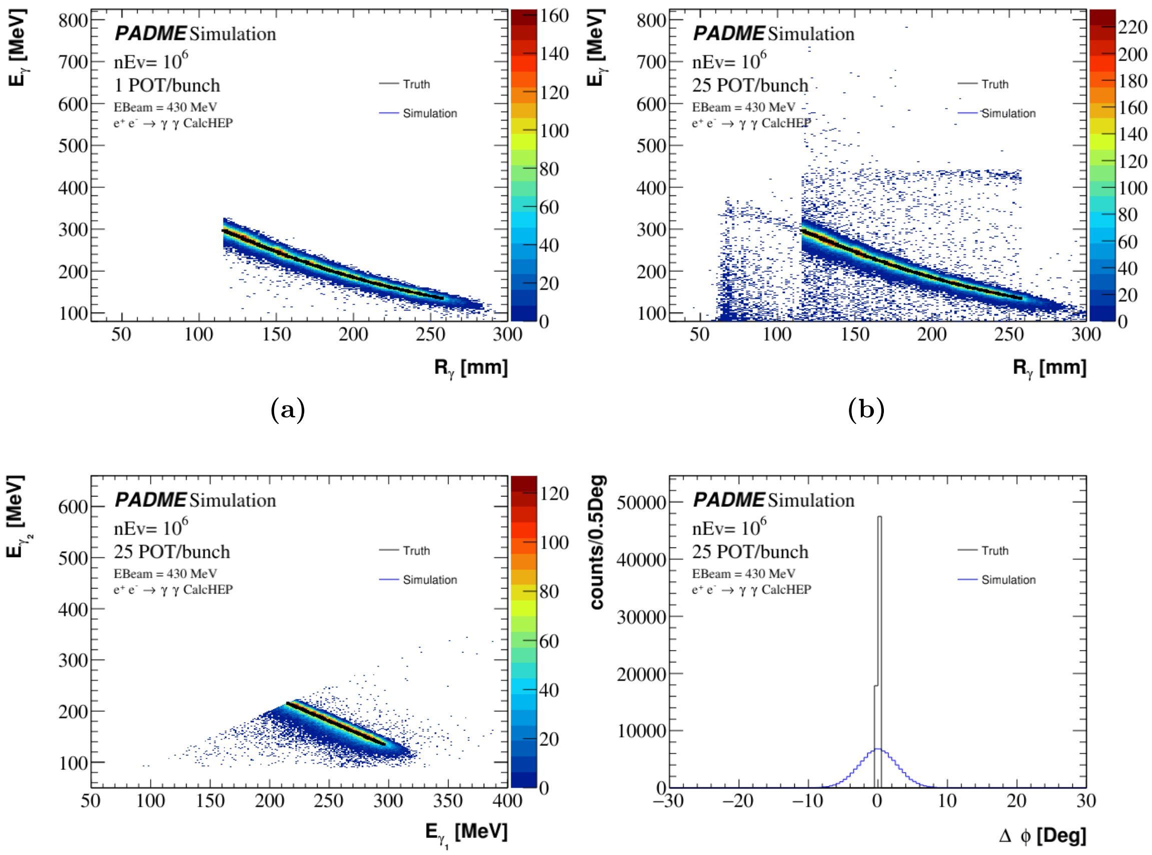

(a) (b)

(c) (d)

Figure 1.3: *Comparison of CalcHEP generation and simulation of the same events with and without pileup. Correlation between energy and radius of the photon for pure annihilation simulation (a) and adding pileup (b). Correlation between the energy of the first and second photon (c) and distribution of* $\Delta\phi$ *(d).*

When the beam intensity is of the order of $25k$ POT/bunch, the pair of photons in time coincidence produced by an annihilation event is overlapped to energy deposits in the calorimeters and hits in the veto detectors that are produced by the physics background processes due to interactions of other positrons in the bunch with the target. The background photons, positrons and possibly electrons seen in the detectors are distributed within the 250 ns time width of the bunch. Therefore, the time coincidence between the two signal photons is a powerful handle to suppress the background which can be used along with the kinematic correlations. Fig. xx, yy, zz ask show the distributions of the same variables shown in Fig. xx-nopileup - zz-nopileup for a sample of annihilation events generated with calchep and simulated in PADMEMC along with 25000 positrons.

In the PADME data the pictures is complicated by the beam induced background, which due to the high rate imply a high probability of accidental two-photon coincidence, and in

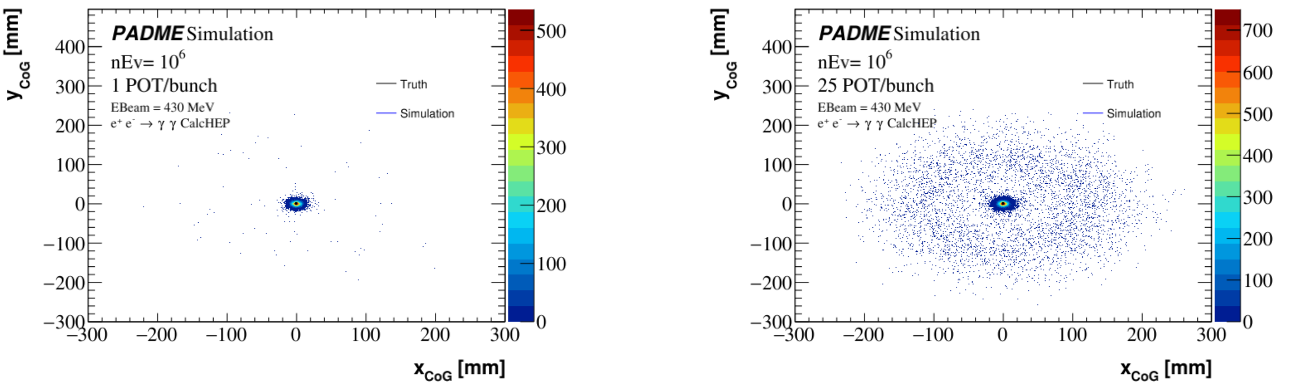

(a) (b)

Figure 1.4: *X and Y CoG map for pure annihilation simulation (a) and adding pileup (b).*

general accidental occurrence of the kinematic correlations typical of annihilation events.

The annihilation yield, i.e. the number of annihilation processes seen in the PADME detector, can be measured starting from the distribution of the sum of the two photon energies, from the CoG distributions or from the difference in the azimuthal angle $\Delta\phi = \phi_1 + 180° - \phi_2$. In all these distributions a peak corresponding to the signal events will emerge over the combinatorial background, if the other correlations are used to select the signal and suppress the background, provided the background rate is below a certain level. Additional selection criteria efficient for the signal consist in setting a minimum photon energy threshold and requiring that the photon has an energy close to the value compatible with its polar angle: $|\Delta E| = |E_\gamma - E(\theta_\gamma)| < \Delta_E^{Max}$.

In the following a sequence of selection cuts, summarized in Table 1.2, will be used to show how the annihilation signal emerges in RunII data.

Table 1.2: *Annihilation selection cut, threshold applied on each variables and cut flow for CalcHEP simulation with pileup from* 25000 *positrons per bunch and for data (run 30563).*

Cut description		Threshold	Simulation	data
Time coincidence	$\lvert t_{\gamma 1} - t_{\gamma 2}\rvert$	< 10 ns		
γ_1 in FR	$R_{\gamma 1}$	$\in]115.82\text{ mm}, 258\text{ mm}[$	0, 70	0, 73
CoG	$\lvert x_{CoG}\rvert$	< 50 mm	1, 00	0, 87
CoG	$\lvert y_{CoG}\rvert$	< 50 mm	1, 00	0, 96
γ energy	$E_{\gamma 1}, E_{\gamma 2}$	$\in [90\text{ MeV}, 400\text{ MeV}]$	1, 00	1, 00
sum of γ energies	$E_{\gamma 1} + E_{\gamma 2}$	$\in [300\text{ MeV}, 600\text{ MeV}]$	1.00	0, 98
γ_2 in FR	$R_{\gamma 2}$	$\in]115.82\text{ mm}, 258\text{ mm}[$	0, 96	0, 96

Where the energy thresholds are defined studying the CalcHEP truth, see Figure 1.5.

Ci vuole un plot di Delta T nei dati la selezione di fig 1,3 per esempio, ovviamente senza taglio in Dt e con |COG|<50 + commento Ci vuole un plot di Delta Phi nei dati la selezione di

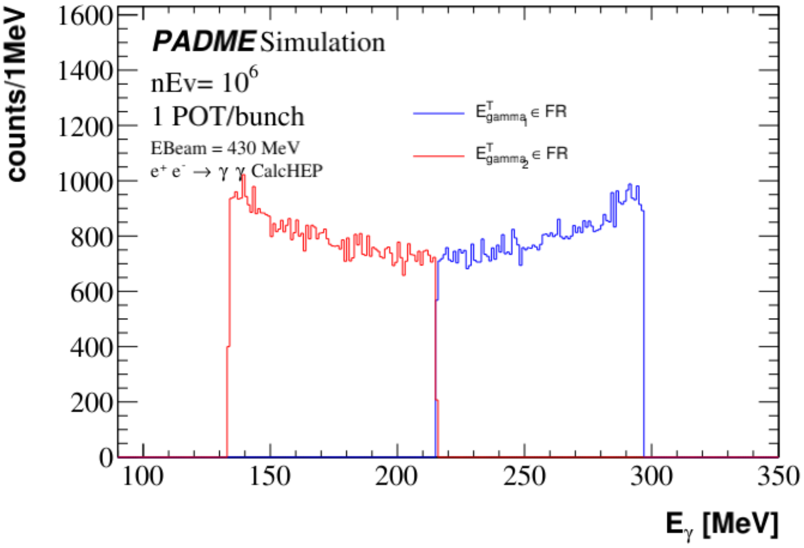

Figure 1.5: *Photon energy distributions in blue for the first photon (in energy) and in red for the second photon.*

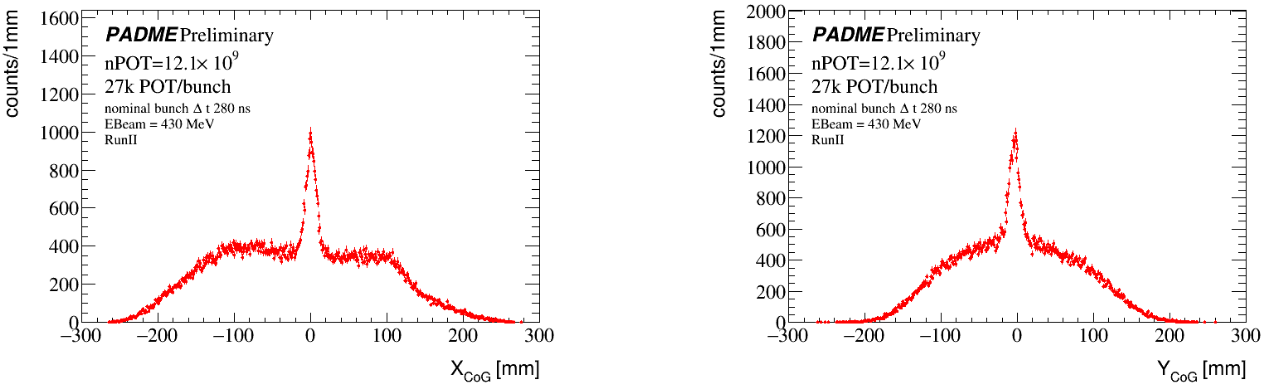

(a) **(b)**

Figure 1.6: *Distribution of the Center Of Gravity variables for the events that satisfy the following cuts, described in Table 1.2: time coincidence and first photon in FR. On the left (a) the distribution of X_{CoG}, on the right (b) the distribution of the Y_{CoG}.*

fig 1,3 per esempio, ovviamente senza taglio in DPhi e con $|COG|<50$ + commento In addition to the cuts on the kinematic variables and on the time coincidence, a geometrical requirement is introduced to ensure a reliable reconstruction of the photons. Indeed, the position of the clusters in ECAL must be at distance from the inner and from the outer border of the calorimeter equal to al least twice the width of a BGO crystal. This ensures limited shower leakage and therefore a good determination of the energy and position. Adding in sequence selection cuts improves the background rejection as demonstrated by Figure 1.7 where the sum of the energy of the two selected photons $E_{\gamma_1} + E_{\gamma_2}$ is shown the red distribution corresponds to events passing the time coincidence and the fiducial region requirement for the most energetic photon γ_1. The amount of background is strongly reduced adding the CoG request (blue distribution). The energy cuts applied to each photon help to further reduce the background. The population of events under the peak, clearly corresponding to annihilation processes, is not significantly reduced by the cuts.

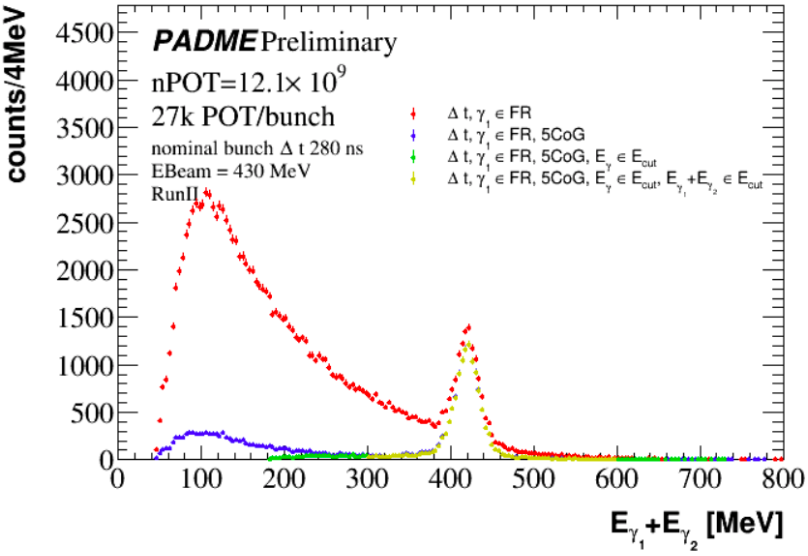

Figure 1.7: *Distribution of $E_{\gamma_1} + E_{\gamma_2}$ for pairs of photons passing various sets of cuts. In red events that pass the time coincidence request with the first photon in the FR; in blue the distribution for events passing also the CoG cut (5 cm). Finally in green (yellow) events satisfy also the energy requirements for one photon (both photons).*

Figure 1.8 (a) shows that the additional cut of the FR on the second photon (the less energetic one) reduces (of $\sim 5\%$) the yield of the annihilation. In Figure 1.8 (b) only the most energetic photon is required to be in the FR. It's interesting to notice that, because of the cut in the inner radius for the leading photon, E_{γ_1} is contrained to be > 100 MeV, on the other hand the energy of the second photon is not subject to sharp cuts, and ranges from about 50 MeV up to 300 MeV. Most of the studies performed are done with two analysis variant: selecting only events with the first photon in the FR or selecting events with both photons in the FR.

1.5 Acceptance

The acceptance has been introduced in Equation 1.1 as a global factor describing the fraction of events corresponding to the process under study that can be detected with the experimental apparatus of PADME and the kinematic requirements applied in the event selection procedure. This concept is based on the assumption of full efficiency of the PADME detectors, DAQ and data reconstruction algorithms. Indeed, in Equation 1.1 all the motivations that can lead to a

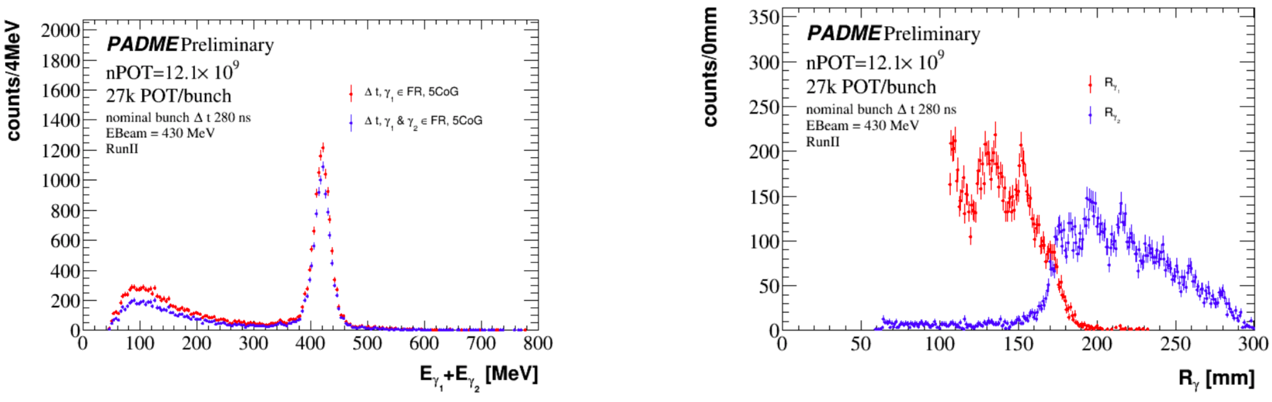

(a) (b)

Figure 1.8: *(a) Distribution of the sum of* $E_{\gamma 1} + E_{\gamma 2}$ *for the events that pass the cuts on time coincidence and CoG. In red the request of FR is applied only to the most energetic photon, while in blue on both photons. (b) Radius distribution for the most energetic photon* $\gamma 1$ *in red and for the less energetic one* $\gamma 2$ *in blue for the events that pass the time coincidence, FR on the most energetic photon, CoG, energetic cuts.*

loss of signal in the data of PADME related to instrumental effects are described through the efficiency term ϵ. As a consequence, the determination of the acceptance must be based on a generator-level simulation of the signal process, before any efficiency, resolution, miscalibration effect plays any role.

The selection cuts described in Table 1.2 are all applied to kinematic properties, involving energies and momenta, except for the requirement that the most energetic photon (or both photons) fall inside a fiducial region of the electromagnetic calorimeter described by an inner and an outer radius. This cut, apparently defined as a geometrical criterion, is dictated by the ECAL geometry but it also has an impact on the energy distribution of the signal photons due to the completely closed kinematics of the two-photon final state in a e^+e^- annihilation process. This requirement is also the only selection cut shaping the phase space of the annihilation process. Indeed, all other cuts are dictated by considerations related to the detector and reconstruction resolution. In summary, if PADME would measure with infinite resolution the photon energies, and positions, each of the selection cut, except for the FR requirement, would have no effect on any signal event with exactly two photons.Therefore, the assessment of the acceptance is strictly related to the definition of the boundaries of the fiducial region.

These boundaries need to be set inside the geometrical boundaries if the calorimeter in order to minimize the effect of the shower leakage. In addition the strong correlation of the two photons implies that for a given value of the beam energy, setting a constraint on the region where, for example, the most energetic photon can be found, directly defines the corresponding region where the second most energetic photon can lie. In order to choose a consistent definition of the fiducial region and estimate the corresponding acceptance a dedicated study was done using CALCHEP and Babayaga simulations at generator level or simulated with a single positron per bunch.

The CalcHEP generator has been used to produce a sample of 10^6 annihilation events according to the LO approximation for the process $e^+e^- \to \gamma\gamma$, with an electron momentum $\vec{P}_{e^-} \sim 0$ MeV/c and a positron energy equal to the energy of the beam $E_{e^+} = 430$ MeV. The three components of the momenta $\vec{P}$ of the two photons of the final state are saved on a text file and used directly to study the events before any detector effect. The same events simulated in PADMEMC allow to assess detector and resolutions effects.The truth information can easily be compared with the simulated event.

A crucial quantity is the radial distance from the original beam direction of the cluster produced by the photon in the calorimeter. In data and in simulation this quantity is computed from the energy weighed position of the BGO crystals in the cluster (see Section reconstruction.. for a detailed discussion).

The measured R_γ allows to measure the polar angle of the photon through the relation

$$R_\gamma = tan(\theta) \times D = \frac{p_T}{p_z} \times D \tag{1.9}$$

where p_T and p_z are the transverse ad longitudinal components of the photon momentum and D is the distance between the target and the plane perpendicular to the z axis representing the ECAL measurement plane.

The parameter D does not match the distance between the target and the entrance surface of the crystals in ECAL. The position of the target and of the ECAL calorimeter in the PADME reference framework are known from design and from survey measurement. The first is $z_{Target} = 1030$ mm and, due to the fact that the thickness of the target is very small it is also considered as the distance of the annihilation production point and the origin of the z axis of PADME that is defined as the center on the dipole magnet. Concerning the z coordinate of ECAL, there are three options to consider: the ECAL front face, the plane where the shower reaches the maximum development and the one corresponding to the mean multiplicity of charged particles in the shower. In Figure 1.9 the distribution of the z coordinates of the GEANT4 hits produced by charged particles in the electromagnetic shower is shown. Thus the options for the coordinate of the ECAL measurement plane are:

- target - ECAL front face, equal to 2440 mm;
- target - most probable value of the shower maximum, equal to 2483 mm, obtained from a fit of the shower longitudinal profile with a landau function;
- target - mean of the shower profile, equal to 2513 mm.

The value of the distance $D = 1030 + 2513$ mm using the mean of the shower z profile if finally chosen. This value statistically guarantees a good match between the radius R_γ computed from the true photon directly with Equation 1.9 and the R_γ corresponding to the cluster position in the simulation. The distributions of the differences between $R_{truth}(3543\ \text{mm})$ and $R_{cluster}$ for the most energetic photon and the least energetic one are shown in Figure 1.10 right and left

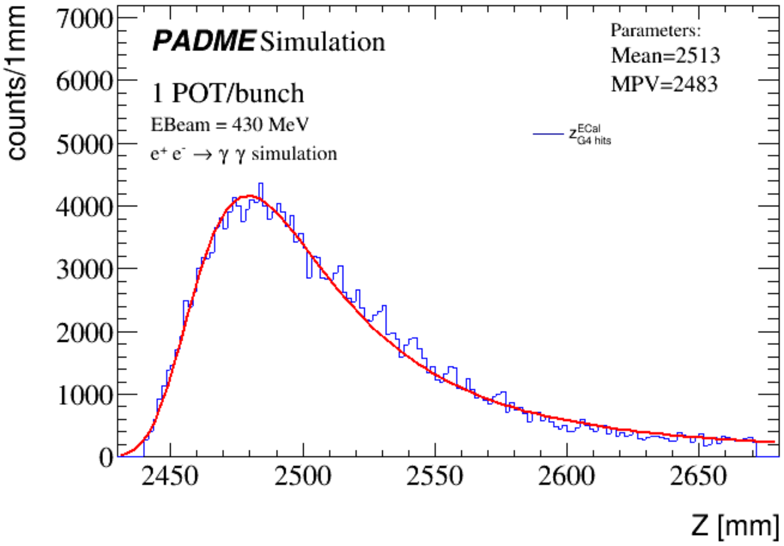

Figure 1.9: *Distribution of the z coordinate of all the hits generated in the BGO crystals of ECal superimposed by a fit using a landau function. The simulation used CalcHEP events simulated in PADMEMC.*

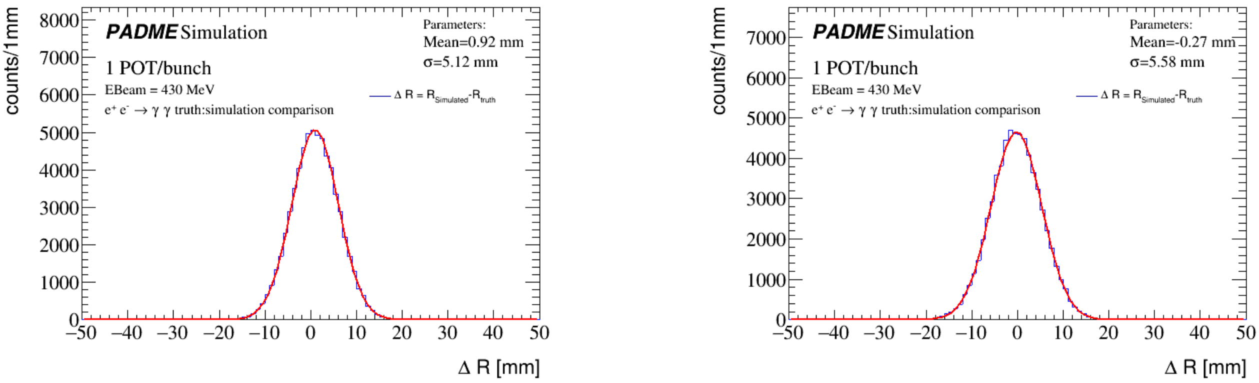

(a) **(b)**

Figure 1.10: *Distribution of the difference between the radius of the photon simulated in PADMEMC and the radius of the truth in the plane at a distance* $D = 3543$ mm *from the diamond target for the most energetic photon (a) and for the second energetic photon (b).*

respectively. Both the distributions, for this value of D, have the mean of the gaussian fit close to 0 and a standard deviation of ~ 5 mm.

Clusters in ECAL may be used as photon candidates if the measured energy and position are reliable. For photons hitting the calorimeter in a peripheral regions, energy and positions are likely biased. The features of the clusterization algorithm implemented in the reconstruction suggest that the bias due to transversal shower leakage is small if the cluster position (computed as the energy weighted position of the crystals contributing to the cluster, that must be at a distance from the seed of no more than two crystals) is reconstructed at a distance at least equal to twice the pitch of the BGO crystal matrix. Using this criterion, the maximum radius of a reliable cluster is equal to 258 mm. Due to the fact that the first and the second photon are correlated in energy, thus in space, the corresponding minimum radius is constrained by the kinematics. In practice it is extracted with a scan on R_{min} studying the number of γ_1 and γ_2 with radius inside the range according to MC truth in a CALCHEP $e^+e^- \to \gamma\gamma$ sample. The value of R_{min} that gives a number of first (most energetic) photons equal to the number of second photon is chosen. As a result the fiducial region for the selection of annihilation photons in the PADME calorimeter is defined as the interval $FR = [115.82, 258]$ mm. Another important parameter is the value of the radius $R_{mid} = R_{\gamma_1}(E_{mid}) = R_{\gamma_2}(E_{mid})$ where the two photons have the same energy and therefore the same radius. This parameter, for an energy of the beam $E_{beam} = 430$ MeV, is equal to $R_{mid} = 172.83$ mm. Table 1.3 reports the number of γ_1 and γ_2 ($N_{\gamma_{1(2)}}$) found in ECAL regions defined in terms of the parameters R_{min}, R_{max} and R_{mid}. The counters shows the consistency of the definition for the three parameters, since the number of N_{γ_1} is equal to N_{γ_2}, and all the most energetic photons fall in the inner ring of ECAL while all those with a lower energy fall in the outer ring as expected by kinematics. In addition in Table 1.3 the number of photons in the upper and lower ECAL region are reported. This number show as for each γ_1 correspond a γ_2 in the opposite ECAL region (e.g. all the γ_1 belonging to the inner ring of ECAL and the upper region have a corresponding γ_2 in the outer ring in the lower region of ECAL).

Table 1.3: *Yield of the most energetic photon γ_1 and the less energetic one γ_2 in the ECAL regions. The radius range $]115.82, 258[$ mm is considered be the fiducial region, the radius $R_{mid} = 172.83$ mm is the radius where the two photon has the same energy. The counters are reported also for the upper and lower parts of the detector.*

Cuts	N_{γ_1}	N_{γ_2}
$\gamma \in]115.82, 258[$ mm	65320	65318
$\gamma \in]115.82, 172, 83[$ mm	65320	0
$\gamma \in [172, 83, 258[$ mm	0	65318

A confirmation that the distance target-ECAL considered is the appropriated, is given by the fact that the the same value for R_{mid} is determined by applying the same considerations to the CALCHEP sample simulated in PADMEMC. Figure 1.11 shows the distribution of R_γ for the first (most energetic) and the second photon. Two selections of events are represented: the first defined by the request that $R^T_{\gamma_1}$, i.e. the true radius of the first photon is in the FR (i.e. in the range R_{min}, R_{max}); the second defined by the request that $R^R_{\gamma_1}$, i.e. the radius of the first photon as reconstructed in simulation is in the FR. For the first case the distribution of $R^T_{\gamma_1}$ and $R^T_{\gamma_2}$ are shown in blue by the solid and dotted line respectively. The two distributions do not overlap and span the entire range of the FR with the first (second) photon well contained below (above) R_{mid}. For the second selection, the distributions of $R^R_{\gamma_1}$ and $R^R_{\gamma_2}$ are shown by the green solid and dotted line respectively. As expected, the distribution of $R^R_{\gamma_1}$ is sharply defined at R_{min}, but some migration above R_{mid} is induced by resolution; similarly, the corresponding $R^R_{\gamma_2}$ distribution starts before R_{mid} and ends after R_{max}. Finally, for the second selection the distributions of $R^T_{\gamma_1}$ and $R^T_{\gamma_2}$ are shown by the cyan histograms with solid and dotted line respectively, showing migration of events at the edges of the FR due to resolution.

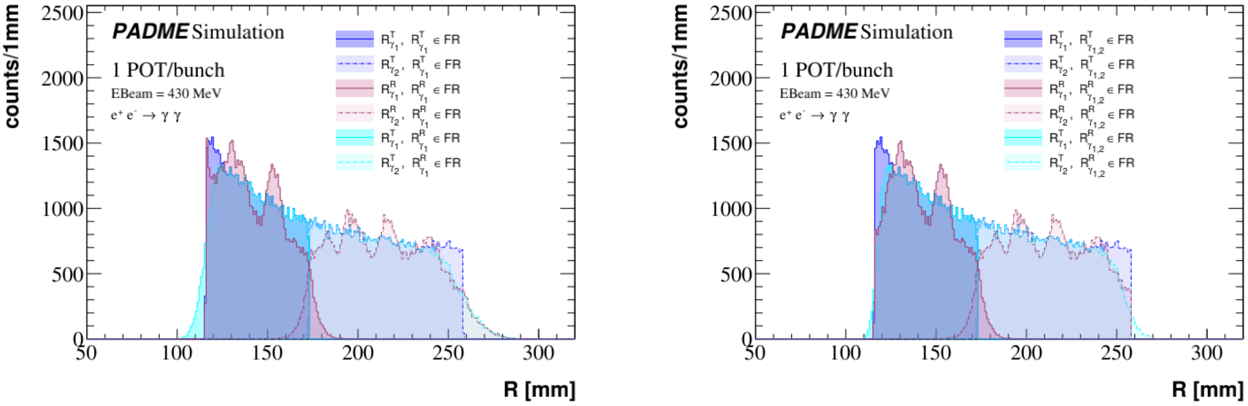

(a) **(b)**

Figure 1.11: *Distribution of true and reconstructed radius of photons from annihilation events. Continuous lines refer to the most energetic photon γ_1, dotted lines to the other photon γ_2. Events are selected either for the first photon (a) and both (b) belonging to the fiducial region at MC truth level or at reconstruction level.*

The same correlation between the radius of the first and second photon predicted by the simulation should be observed if beam energy and detector geometry are well known. In Figure 1.12 the points show R_{γ_2} as a function of R_{γ_1} in PADME annihilation events. The annihilation photon candidates are selected with the application of the cuts presented in the Section 1.4 (in particular cuts a,b,c,d,e are applied). The black continuous line is correlation between observed in CalcHEP sample using MC truth. The agreement is a check of the good description of the geometry.

1.5.1 The acceptance at leading order

The acceptance of the fiducial region defined for the measurement was extracted as a global factor telling what fraction of the annihilation events reach ECAL in the FR. The effect of event migration at the boundary of the FR, which instead is a function of polar angle of the photons, will be estimated later and treated as a correction to the efficiency.

The global acceptance is given by

$$acc = \frac{N^{gen}_{\gamma\gamma} \in FR}{N^{gen}_{\gamma\gamma}} \tag{1.10}$$

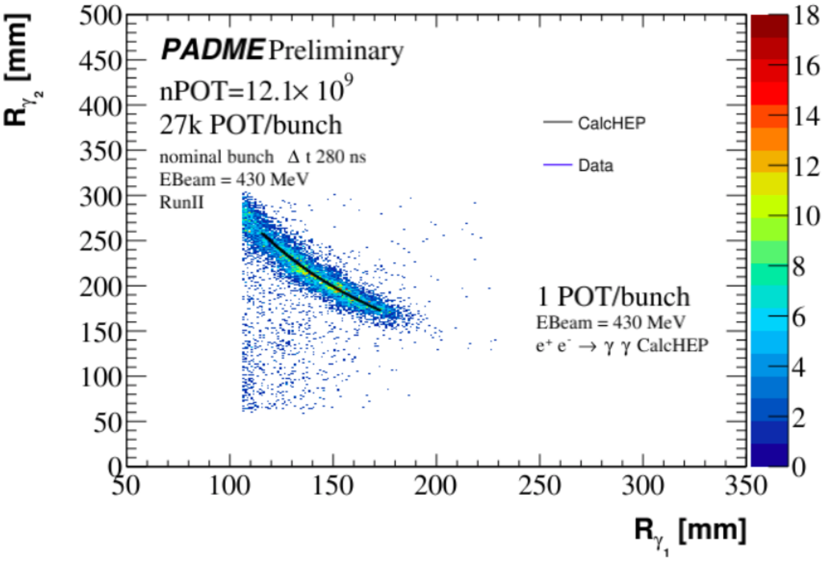

Figure 1.12: *Correlation between the radius of the first and second photon. Points are PADME data after a tight selection of annihilation events, corresponding to cuts a,b,c,d,e presented in Section 1.4. The black line is the same correlation according to MC truth in CalcHEP.*

where $N^{gen}_{\gamma\gamma} \in FR$ if the number of the annihilation events generated by CalcHEP generation that fall in the FR, and $N^{gen}_{\gamma\gamma}$ is the total number of the generated events. The sample used for this study consist of 10^6 annihilation events, and the number of the annihilation events observed in the FR is $\sim 65,3 \times 10^3$, thus the global acceptance is $A = 0.0653 \pm 0.0003$ where the error comes from the statics of the MC sample.

1.5.2 A correction for migration effects

In the PADME data the cut used to decide if an event belongs to the FR are applied to values of R_γ that are reconstructed from quantities measured by the detector. The simulation of the CALCHEP sample can be used to understand how the number of events that are truly in the FR, $N^{gen}_{\gamma\gamma} \in FR$, relates to the number of events that are reconstructed, in the assumption of full efficiency, within the FR, $N^{reco}_{\gamma\gamma} \in FR$. The ratio,

$$A_{mig}(\theta_1, \theta_2) = \frac{N^{reco}_{\gamma\gamma} \in FR}{N^{gen}_{\gamma\gamma} \in FR} \qquad (1.11)$$

will need to multiply the event dependent efficiency at the denominator of Equation 1.1.

In order to disentangle the efficiency effects from migration effects, the correction A_{mig} has been estimated using a smearing of the polar angle of the photons from the MC truth and comparing with distributions at generator level. The gaussian smearing was defined using the data, and looking at the width of the distribution of the reconstructed polar angle of a given photon, once the value of theta for the other is set to a constant value. This width of the distribution was found to have a negligible dependence on the polar angle and to be equal to $\sigma_\theta = 2.04$ mrad. After that, the following samples of events are in hands:

1. annihilation at generator le events from CalcHEP in the entire phase space;
2. annihilation at generator leevents from CalcHEP in the entire phase space with both photon polar angles smeared by σ_θ.

The correction is measured as:

$$A_{mig}(\theta) = \frac{N^{smeared}_{\gamma\gamma}(\theta_i)}{N_{\gamma\gamma}(\theta_i)} \tag{1.12}$$

where $N^{smeared}_{\gamma\gamma}(\theta_i)$ is the number of photons of the smeared sample with a polar angle equal to θ_i, and $N_{\gamma\gamma}(\theta_i)$ is the number of photons generated with a polar angle equal to θ_i.

The first step is to select all the events in the samples 1. and 2. that have $R_{\gamma_1} \in FR$ and study the distributions of the polar angle of both photons. These are shown in Figure 1.13 (a), in blue for MC truth and in red for the smeared sample. The ratio of the two distribution, as described in Equation 1.12, is represented in Figure 1.13 (b). This shows that if the event selection enforces the FR cut corresponding to the acceptance through a request applied only to one photon[3], in this case the most energetic one, the correction for migration effects it be applied as function of θ_{γ_1} is always compatible to one.

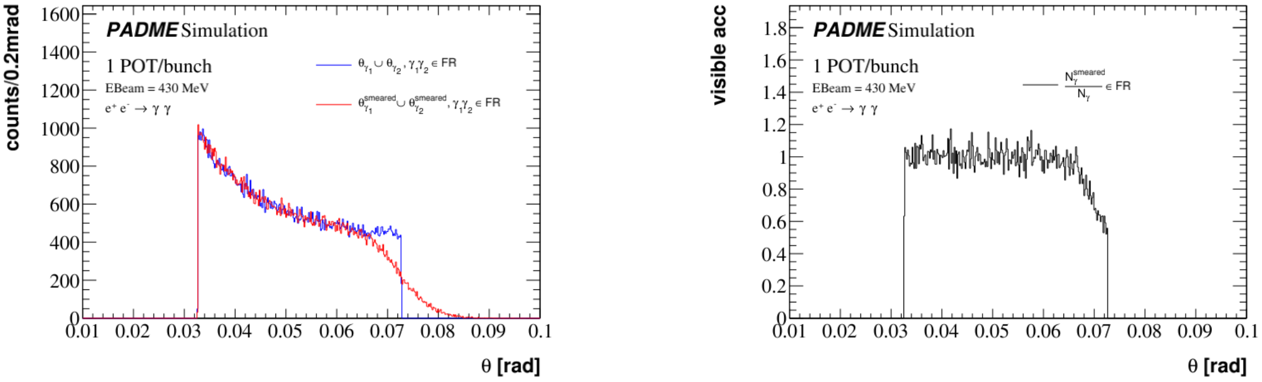

(a) **(b)**

Figure 1.13: *(a) Distribution of the polar angle of the two photons of the annihilation sample, in blue the CalcHEP generation, in red the same sample after the smearing in theta. The selection for this events is* $R_{\gamma_1} \in FR$. *(b) The visible acceptance calculated as the ratio between the number of annihilation in a single bin for the sample with the smearing over the sample from the generator (red line / blue line of the Figure (a)).*

On the other hand if the event selection requires that both photons are reconstructed in the FR, the correction for migration effects, applied again per event as a function of θ_{γ_1} (or

---

[3] One has to remember that in terms of acceptance, i.e. when considering generator level quantities, requiring only one photons in the FR is perfectly equivalent to requiring both photons in the FR.

$\theta_{\gamma 2}$), depends on the event topology, as shown in Figure 1.14. Here, the distributions of the polar angles for both photons are shown after selecting all the events in both smeared and MC truth samples with both photons in the FR. The ratio of the two distributions, as described in

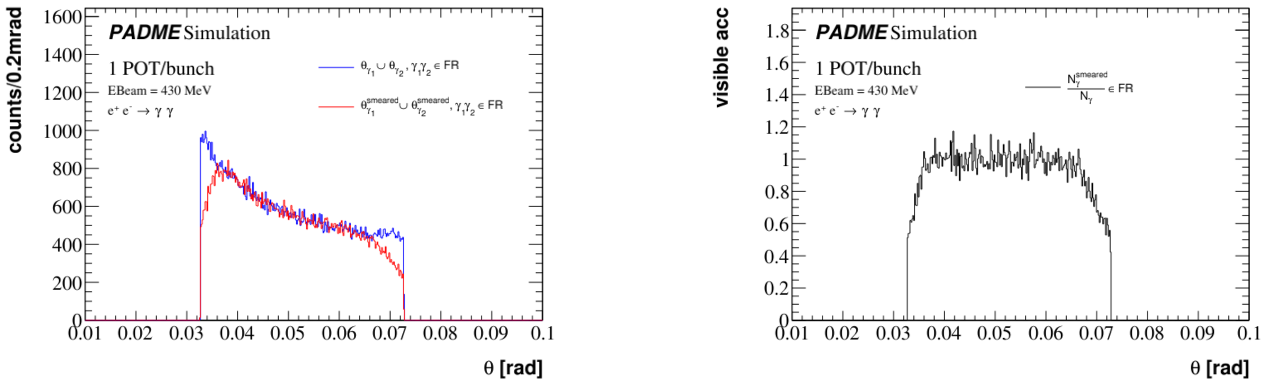

(a) (b)

Figure 1.14: *(a) Distribution of the polar angle of the two photons of the annihilation sample,for CalcHEP generation (blue) and after the smearing in polar angle (red). The selection for this events is both the photon $R_{\gamma 1}, R_{\gamma 2} \in FR$. (b) Visible acceptance calculated as the ratio between the number of annihilation in a single bin for the sample with the smearing over the truth sample (red line / blue line of the Figure (a).)*

Equation 1.12, is shown in Figure 1.14 (b). In this case, the correction is not identically equal to one.

1.5.3 Acceptance at NLO

The CalcHEP generator produces annihilation events, with exactly two photons in the final state, at the leading order in the perturbative expansion. It can also be used to produce the process $e^+e^- \to \gamma\gamma(\gamma)$ at the leading order approximation; Eventually the two samples might be combined to derive a general estimate for the inclusive cross section for the process e^+e^- to photons, however this procedure is prone to theoretical inaccuracies. On the other hand, Babayaga is NLO event generator for the $e^+e^- \to \gamma\gamma$ process, which means that the production of two and three photons are consistently managed over the phase space. In addition, Babayaga can be configured to run in the LO approximation, therefore a first check done to verify the compatibility of the LO predictions from the two generators. The total cross sections obtained are $\sigma(e^+e^- \to \gamma\gamma)^{CalcHEP} = 1.91218$ mb and $\sigma(e^+e^- \to \gamma\gamma)^{Babayaga} = 1.91096 \pm 0.00036$ mb with a relative difference of 0.06%. Another check was done to compare the kinematics measuring the global acceptance of the process. In this case the one measured with Babayaga is $acc^{Babayaga} = 0.0651$, thus there is a relative difference of -0.4% with the acceptance measured with CalcHEP. After these preliminary check a sample of the process $e^+e^- \to \gamma\gamma(\gamma)$was generated. When running Babayaga at NLO up to three photons can be generated and the three photon final state is not anymore fully constrained. In this case the spatial resolution of ECAL should be considered if a soft photon falls close to another one, they may be reconstructed as a single cluster. To take into account this clustering effect photons from Babayaga are merged if the second lies at a distance in X or Y from the other compatible with the clusterization algorithm. In this case the resulting merged photon is assigned an energy equal to the sum of the two original energies and a position computed as an energy weighted average of the original positions. After this procedure, the photons are requested to pass the kinematic cuts that will be applied in the event selection: $E_\gamma > 90$ MeV and $|\Delta E| = |E_\gamma - E(\theta_g)| < 100$ MeV. Notice that these conditions in a LO simulation are trivially satisfied, therefore they ere not applied to estimate the Acceptance in the LO approximation. The events where at least one pair of photons passing the kinematic cuts and lying both inside the FR are counted as events inside the acceptance. The ratio of this number to the total number of events produced by Babayaga is used to assess the acceptance that is measured to be: $A = 0.06341 \pm 0,00026$ that is relative 2.6% lower than the acceptance at the leading order. This is used to measure the cross section as described in the next sections.

The systematics that can affect the acceptance come from perturbative approximation and the error on the distance between the target and the ECAL detector. For the first of them the NNLO correction is quoted be of the order of 0.1% put reference, hence it can be neglected. For the second the variations of the acceptance when changing the distance between ECAL and target have been estimated and they are summarized in Table 1.4 . Since the systematic error the measurement of the distance from the survey of the PADME apparatus is $\sim few$ mm, also this systematic uncertainty can be neglected.

Table 1.4: *Acceptance calculation obtained varying the distance between ECAL and target.*

Variation [mm]	$acc^{Babayaga}$	$\frac{acc^{Babayaga}}{acc_0^{Babayaga}}$
-15	0.0627771	0.990
-10	0.0629869	0.993
-5	0.0632111	0.997
0	0.0634096	1.000
$+5$	0.0632002	0.997
$+10$	0.0629825	0.993
$+15$	0.0627801	0.990

1.6 Efficiency determination and closure tests

The photon efficiency was measured on data by developing a tag and probe technique exploiting the closed kinematics of annihilation events. Typically data driven efficiency measurements benefit from another auxiliary detector that allows to observe a sample of reference particles (probes), sometimes identified as belonging to a specific category of interest thanks to a tagging criterion. Then, the efficiency for reconstructing and identifying that category of particles with the detector and procedure under test is measured as the number of probes that are actually matched a particle reconstructed by the detector or procedure under test. For example, in a detector with a central spectrometer IS tracking all charged particles and an outer spectrometer OS for muons, the OS efficiency can be measured by looking for a well reconstructed muon reconstructed (tag) that combined with a track (probe) reconstructed in the IS gives an invariant mass corresponding to the J/Psi mass; the OS efficiency is given by the number of probes that have a matching muon track in the OS divided by the total number of probes.In the case of annihilation events in PADME calorimeter is a destructive detector and there is no other tagging detector to confirm the presence of a photon. Therefore the redundancy of kinematic constraints in the annihilation process is used to define a tag, a probe and to test if the probe is matched.

1.6.1 Tag and probe with annihilation events in PADME

As already extensively discussed, the two photons produced in the final state of $e^+e^- \to \gamma\gamma$ are correlated in energy and in space. Figure 1.15 shows that the polar angle of an annihilation photon predicts its energy, through an analytical function $E = f(\theta)$. Therefore, if a photon in ECAL comes from annihilation:

- its energy is compatible with $E_\gamma = f(\theta_\gamma)$;
- a second photon must exist back to back in phi to the first with $E_{\gamma 2} = E_{beam} - E_{\gamma 1}$;
- the energy of the second photon is also compatible with $E_{\gamma_2} = f(\theta_{\gamma 2})$.

Therefore, the tag is identified as a cluster in the FR of ECal with:

$$\Delta E_{tag} = E_{Tag} - f(\theta_{Tag}) \tag{1.13}$$

close to zero. All the clusters in the FR with $|\Delta E_{Tag}| < 100$ MeV are considered tag candidates. This is a very loose cut considering that the resolution on ΔE_{Tag} is of the order of ~ 15 MeV.

When a tag candidate is found, the probe is defined as the "expected second photon" from the annihilation therefore, the number of probes is equal to the number of tags.

Finally, a matched probe candidate is defined as a cluster with features similar to the probe hypothesis; this means with $|\phi - \phi_{Probe}| < 25$ Deg, with $|\Delta E_{Probe}| < 100$ MeV, where $\Delta E_{Probe} = E_{Probe} - f(\theta_{Probe})$, and with $|\Delta E_{TP}| < 100$ MeV, where $\Delta E_{TP} = E - E_{beam} + f(\theta_{Tag})$. In addition, a matched prove is requested to be in time with the tag photon within 7 ns.

If more than one cluster seems to match a given tag, a choice must be taken; this is done by selecting the candidate matched probe with the minimum χ^2 defined as follows:

$$\chi^2 = \frac{\Delta E'^2 + \Delta E^2_{probe}}{\sigma^2} = \frac{\Delta E^2_{Probe} + \Delta E^2_{TP}}{\sigma(E_{\gamma_1})^2 + \sigma(E_{\gamma_2})^2} \tag{1.14}$$

where $\sigma(E_{\gamma_i})$ for $i = 1, 2$ is the energy resolution of the calorimeter and it is considered equal to 15 MeV for all the clusters. An additional analysis was made requesting the belonging of

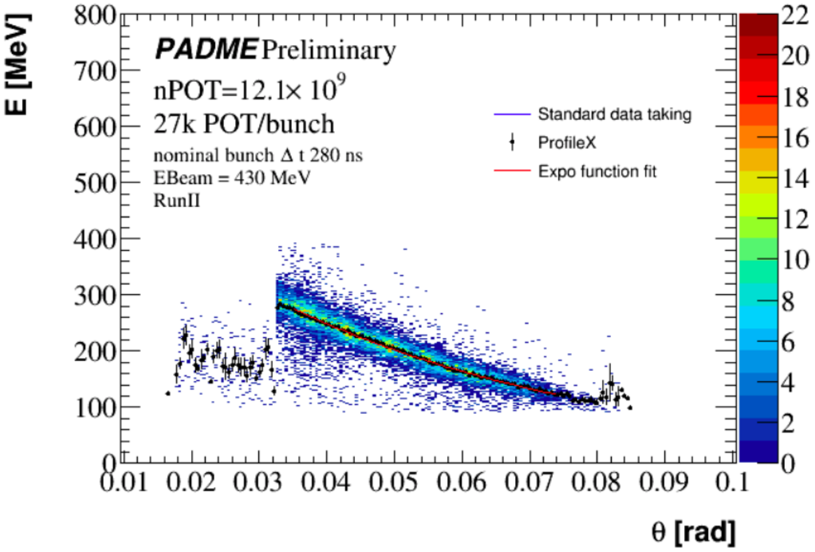

Figure 1.15: *Correlation between the energy E and the polar angle θ of annihilation photons. For the plot are used data of run II and events that pass the selection: a,b,c,d,e, described in Section 1.4, to be background free. To extract the function $f(\theta_g)$ used in this studies to extract the predicted energy of the photon, a profileX was done, thus an exponential fit on a good region of it (fitted in* $[0.035, 0.074]$ rad *to exclude the problematic points). The parameters extracted are used to convert the polar angle in energy.*

the second photon in the FR. In the following studies, in order to understand each element of the analysis, the efficiency and the corrected annihilation yields are reported for both the selections: γ_1 in FR and γ_1, γ_2 in FR.

Finally, given the sample of tag candidates, the counting of the "signal candidates" N^{sig}_{Tag}, i.e. of the photons that are really originating from an annihilation, requires the subtraction of a large background; similarly, the counting of the matched probes, N^{sig}_{Probe}, in the sample of candidates requires the subtraction of a background that, in this case, is very small.

The efficiency is therefore computed as follows:

$$\epsilon \pm \sigma = \frac{N^{sig}_{probe}}{N^{sig}_{tag}} \pm \sqrt{\frac{N^{sig}_{probe}}{(N^{sig}_{tag})^2} + \left(\frac{N^{sig}_{probe}}{(N^{sig}_{tag})^2}\right)^2 \times N^{sig}_{tag}} \qquad (1.15)$$

The error takes into account the poisssonian fluctuation of both counters because the background, dominating the selection of tag candidates, washes out the correlation of numerator and denominator that would require a binomial treatment.

Indeed the subtraction of the background contaminating the sample of candidate tags and the determination of the number of signal tags is the most critical step in the procedure and several approaches have been adopted. The first strategy consists in modelling the background using the sideband or a control data sample, applying a gaussian fit to the signal peak to estimate its standard deviation; The number of tags is then computed as the integral of the background subtracted distribution in the range corresponding to 3 sigma. The same procedure is applied to count the number of matched probes in the sample of candidates. An assessment of the systematic error affecting the efficiency determination is obtained by estimating the number of tags and probes consistently as the integral within 1 or 5 sigma of the background subtracted candidate distribution.

This method has been applied to measure the efficiency in 16 bins covering the ECAL geometry, two radial bins and 8 azimuthal bins.

1.6.2 Validation in MC

The entire methodology was tested on MC samples of different types: pure annihilation events in a perfect PADME detector, annihilation events overlapped to a realistic pileup of other interactions, with and without defects in the calorimeter.

Efficiency from MC truth

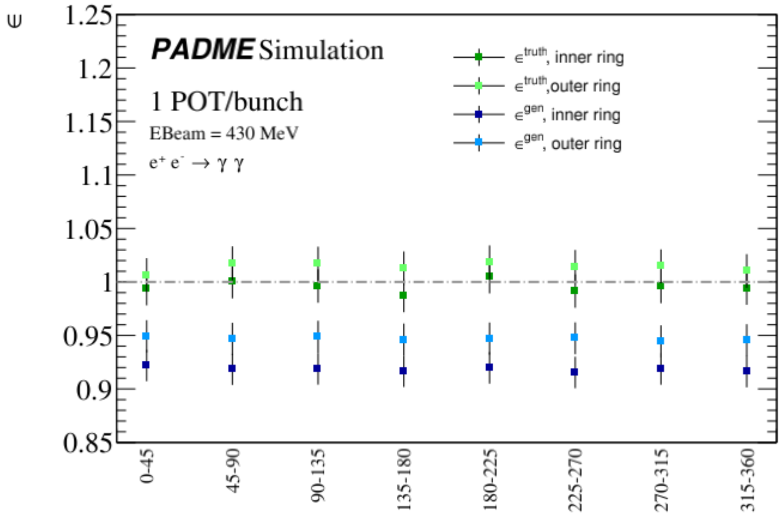

Figure 1.16: *True and effective efficiency for photons from annihilation events, in the absence of pileup and detector defects. The efficiency is quoted in 8 bins in phi each divided in 2 bins in R.*

A preliminary study tried to address the relation between true photons and reconstructed photons in a perfect ECAL, without detector defects nor pileup. ECAL was divided in 8 azimuthal slices and each one in two radial intervals: $R_{min} - R_{mid}$ and $R_{mid} - R_{max}$. In each event the photon spatial coordinates from the MC truth and from the reconstruction of the same events simulated with PADMEMC are studied. The following quantities are studied

- effective efficiency, defined as the ratio between the number of reconstructed photons and the number of generated photons in each bin $\epsilon^{truth} = \frac{N_\gamma^{sim}}{N_\gamma^{gen}}$. This is shown in Figure

1.16 for each bin (green dots), where N_γ^{sim} is the number of annihilations observed in that bin analysing the simulated sample and N_γ^{gen} is the number of annihilation recorded in the same bin studying the truth information. A first observation is that in some bins the effective efficiency is higher than 1 due to a migration effect. Indeed, the photon reconstructed coordinates are modified by the resolution and segmentation of the detector and by the presence in the experiment of all the components. This effect is observed in all bins of the outer ring;

- true efficiency, given by the ratio between the number of the simulated photons having true and reconstructed spatial coordinates in a bin and the number of the generated γ that fall in the same bin $\epsilon^{gen} = \frac{N_\gamma^{sim}(\gamma^{gen})}{N_\gamma^{gen}}$, where $N_\gamma^{sim}(\gamma^{gen})$ is the number of the annihilations having truth and simulated coordinates in the bin. This is shown by the light blue points in figure 1.16. The truth efficiency in the outer ring $[R_{mid} - R_{max}]$ is systematically higher then the inner ring $[R_{min} - R_{mid}]$ due to a stronger loss (migration toward the outside) for resolution in the inner region.

Tables 1.5 (for the inner ECAL ring) and 1.6 (for the outer ECAL ring) report for all the azimuthal slices the truth efficiency ϵ^{truth}, the efficiency ϵ, the feed-through and loss at the inner and at the outer boundary are summarised. The feed-through at the inner boundary is defined as the ratio of the number of clusters simulated in that bin but with the truth at $R_\gamma < R_{min}^{range}$ to the total number of clusters in the bin. The loss at the inner boundary is the ratio between the number of clusters simulated with a radius $R_{cl} < R_{min}^{range}$ but with the truth with radius in the bin. Analogous definitions are used for the feed-through and loss at the outer boundary.

Table 1.5: *True and effective efficiency, feed-through and loss at the inner and outer boundary of the bin for photons from annihilation events, in the absence of pileup and detector defects. The efficiency is quoted in 8 phi bins for R in* $[R_{min}, R_{mid}]$.

Angle range	ϵ **truth** ±0.015	ϵ ±0.016	feed through in ±0.002	loss in ±0.002	feed through out ±0.002	loss out ±0.002
[0, 45[	0,923	0,994	0,046	0,044	0,030	0,034
[45, 90[	0,918	1,000	0,050	0,046	0,029	0,037
[90, 135[	0,919	0,996	0,047	0,045	0,028	0,037
[135, 180[	0,917	0,987	0,047	0,050	0,031	0,033
[180, 225[	0,920	1,005	0,047	0,044	0,029	0,036
[225, 270[	0,915	0,994	0,049	0,048	0,028	0,036
[270, 315[	0,919	0,996	0,048	0,050	0,034	0,033
[315, 360[	0,916	0,994	0,046	0,049	0,029	0,035

Table 1.6: *True and effective efficiency, feed-through and loss at the inner and outer boundary of the bin for photons from annihilation events, in the absence of pileup and detector defects. The efficiency is quoted in 8 phi bins for R in* $[R_{mid}, R_{max}]$.

Angle range	ϵ truth ±0.015	ϵ ±0.016	feed through in ±0.002	loss in ±0.002	feed through out ±0.002	loss out ±0.002
$[0, 45[$	0,949	1,020	0,035	0,030	0,027	0,021
$[45, 90[$	0,947	1,017	0,040	0,027	0,030	0,026
$[90, 135[$	0,949	1,017	0,039	0,026	0,033	0,026
$[135, 180[$	0,946	1,013	0,034	0,030	0,027	0,024
$[180, 225[$	0,947	1,018	0,036	0,029	0,027	0,024
$[225, 270[$	0,947	1,014	0,037	0,024	0,033	0,028
$[270, 315[$	0,945	1,015	0,035	0,031	0,032	0,024
$[315, 360[$	0,946	1,010	0,035	0,028	0,027	0,026

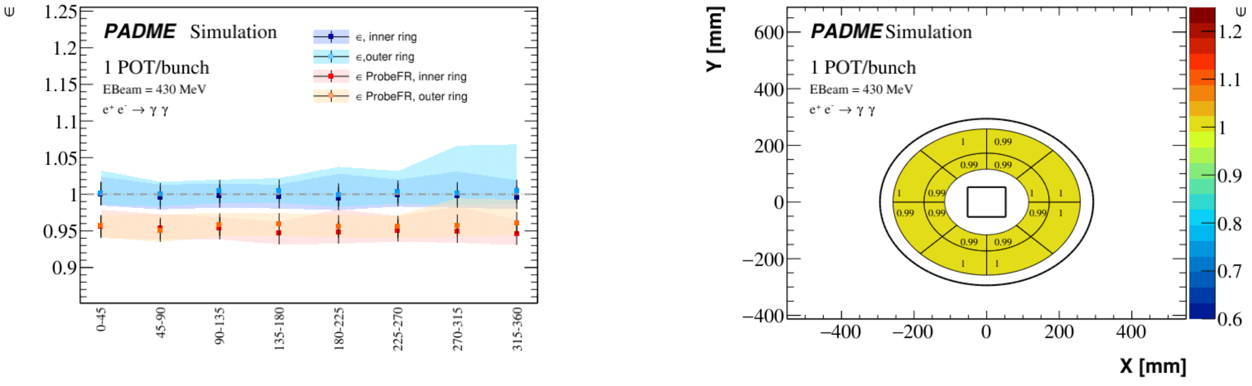

(a) (b)

Figure 1.17: *Tag and probe efficiency estimated for photons from annihilation events, in the absence of pileup and detector defects. The efficiency is quoted in 8 bins in phi each divided in 2 bins in R. (a) The efficiency is quoted with (red) and without (blue) the requirement that the matched probe belongs to the fiducial region. (b) Schematic view of the efficiency without any requirement.*

Tag and probe on MC

A first study was done in simulated single annihilation events, ignoring pileup and defects of the detector. For this reason the selection of the tag and of the matched probe are free from any background. In this case the number of tags (matched probes) in measured by integrating 3σ the peak of the distribution of ΔE_{tag} (ΔE_{probe}). The systematic errors are estimated as described in section 1.6.1. Figure 1.17 shows in blue the tag-and-probe efficiency defined as the number of matched-probes divided by the number of tags; in red the tag-and-probe efficiency within the fiducial region is defined as the number of matched probes in the fiducial region divided by the number of tags. Error bars represent the statistical error σ while the shaded band corresponds to the total error $\sigma \oplus \sigma_{sys}$ including the systematic uncertainty.

Comparing truth and tag and probe efficiency

The definitions based on MC truth and shown efficiency in Figure 1.16 differ from those based on the tag and probe technique represented in Figure 1.17. However, a comparison between $\epsilon^{truth} = \frac{NClusters_i}{NTruth_i}$ of the Figure 1.16 (green dots) and the tag and probe efficiency without the request for the matched probe to be in the FR $\epsilon^{TP} = \frac{nProbe_i}{nTag \in bin_j}$[4] can be done. As discussed in Section 1.6.2, the differences between the efficiency in the inner bins and in the outer ring Figure 1.16 is due to migration effects. In the tag and probe efficiency trend this effect is reduced. In addition the efficiency is never higher than 1 because the existence of a probe is constrained to the existence of a tag, so also when the number of tags is lower than the number of clusters in the opposite bin (case of tag in bins of the inner ring as described in 1.6.2), the number of probes can't be higher than the number of tags. When the number of tags is higher than the number of clusters in the opposite bin (case of the tag in the outer ring) the absence of an explicit boundary between inner and outer ring for the probe allows to find a matched probe, so the efficiency is still close to one. From these considerations it follows that the efficiency extracted from tag and probe is more stable when moving from an inner to an outer bin. The small differences in the tag and probe efficiency are induced by cluster reconstruction.

Table 1.7 summarized the ratio between the effective efficiency from MC truth and the one measured with the tag and probe (TP):

$$\alpha = \frac{\epsilon^{truth}}{\epsilon^{TP}} = \frac{\frac{NClusters}{NTruth}}{\frac{NProbe}{NTag}}. \tag{1.16}$$

for all the phi slices, inner and outer rings. In the inner ring bins the truth and TP efficiencies are equal within the 1%, while in the outer ring the truth efficiency is higher than the TP one because more affected by migration effects.

1.7 Closure tests on simulation

1.7.1 Tag and probe efficiency and detector defects

To test how the tag and probe efficiency depends on detector defects, the CalcHEP sample $e^+e^- \to \gamma\gamma$ was simulated emulating four dead crystals in ECAL in the bin $\phi \in [45, 90]^\circ$ in order to induce an important localised defect. Figure 1.18 shows the map of the annihilation photons for this special sample.

First the effective efficiency for this special sample was estimated using the knowledge of MC truth as described in section 1.6.2. The dependence on the bin in ECAL is shown in

---

[4] In this nomenclature the subscript i means the bin in which ECAL efficiency is studied, while j is the bin with opposite azimuthal angle and opposite radius range (constrain given by the kinematics of the annihilation).

Table 1.7: *Ratio between the effective truth derived from MC and TP efficiency.*

Angle range	α inner ring	α outer ring
$[0, 45[$	$0,994$	$1,018$
$[45, 90[$	$1,004$	$1,018$
$[90, 135[$	$0,999$	$1,013$
$[135, 180[$	$0,991$	$1,009$
$[180, 225[$	$1,011$	$1,019$
$[225, 270[$	$0,995$	$1,011$
$[270, 315[$	$0,999$	$1,014$
$[315, 360[$	$0,999$	$1,006$

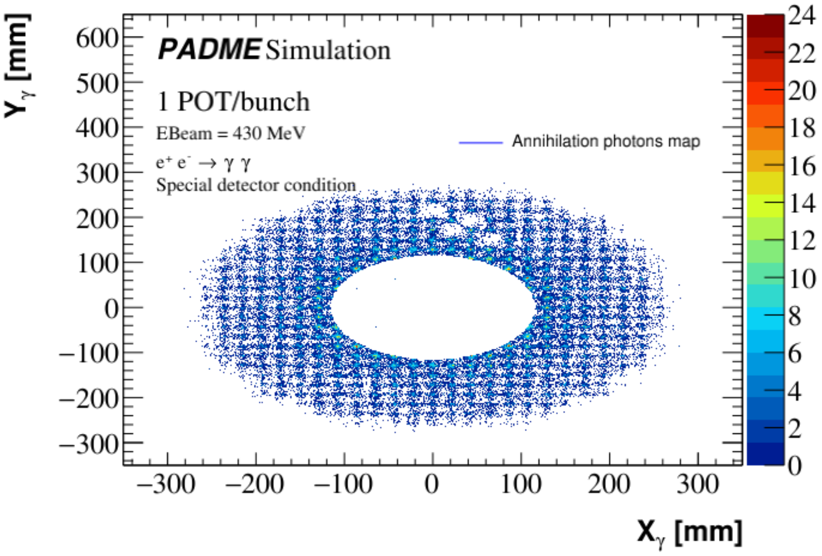

Figure 1.18: *Map of the annihilation photons selected with only the time coincidence requirement and the application of the FR to the most energetic photon. This is a special simulation with four dead crystals, made to test the tag and probe efficiency.*

Figure 1.21 (a). As expected the efficiency is lower in the region where the detector response is affected by the dead crystals. Then the ΔE_{Tag} and ΔE_{Probe} were studied to extract the tag and probe efficiency. The distribution of these variables in this special sample are not gaussian for all the bins. Figure 1.19 shows the distribution of ΔE_{tag} for tags reconstructed in a bin without problems $\phi \in [180, 225]$ Deg , R $\in]\mathrm{R_{min}}$ and $\mathrm{R_{mid}}[$ while Figure 1.19 (b) the same distribution observed for the problematic bin with $\phi \in [45, 90]$ deg and R $\in]\mathrm{R_{min}}, \mathrm{R_{mid}}[$. The probe distributions are affected by the same problem as indicated by Figure 1.20 where the ΔE_{Probe} distributions are reported for the same bins. Also for this variable is visible a tail appears where there are dead crystals. The procedure applied to measure the tag and probe

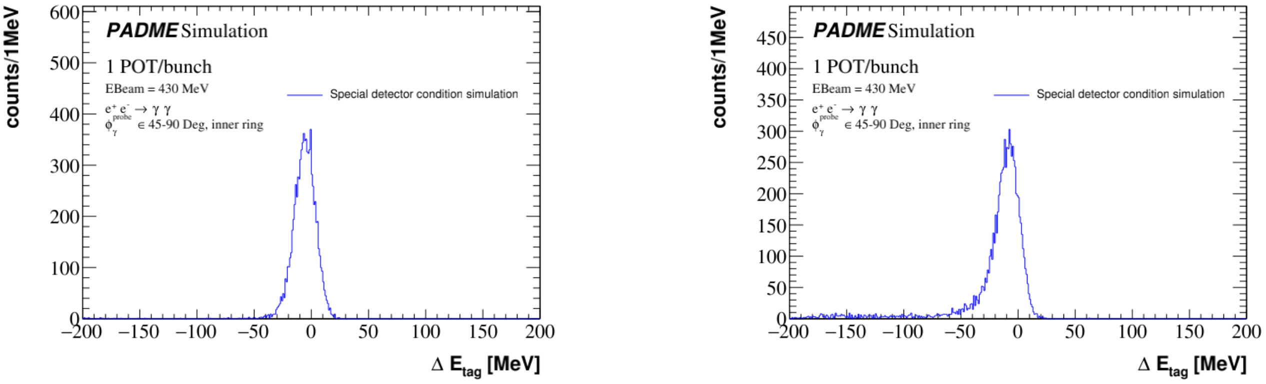

(a) **(b)**

Figure 1.19: *ΔE_{Tag} distribution for the MC simulation of pure annihilation events in a simulation where the detector has dead channels. On the left the distribution is plotted for a bin without dead crystals, on the right the same distribution for tags reconstructed in the bin with dead crystals.*

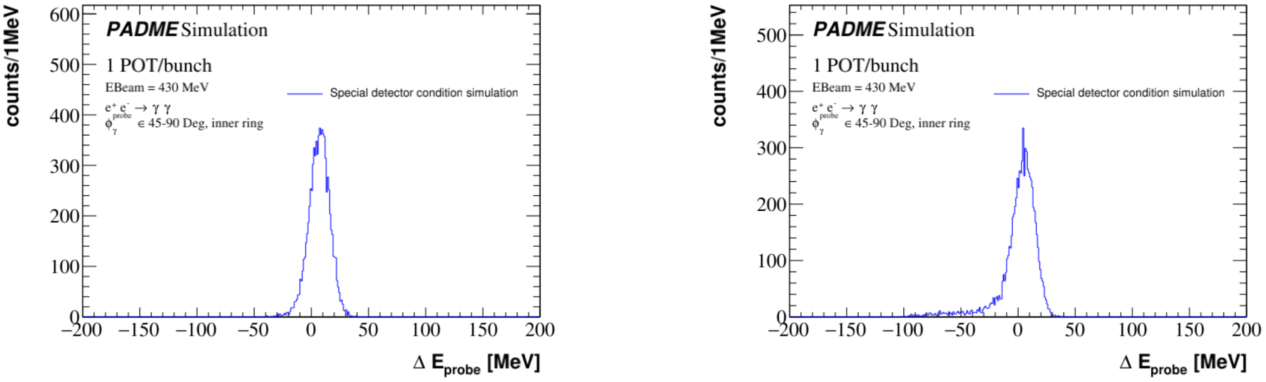

(a) **(b)**

Figure 1.20: *ΔE_{Probe} distribution for the MC simulation of pure annihilation events in a simulation where the detector has dead channels. On the left the distribution is plotted for a bin without dead crystals, on the right the same distribution for tags reconstructed in the bin with dead crystals.*

efficiency is the one described in the previous section and the efficiency obtained is reported in Figure 1.21 (b). In the ECAL slice where four dead crystals were simulated the efficiency is strongly reduced $\epsilon \sim 0.86$. The corresponding increase of the efficiency in the opposite phi slice shows that the efficiency extracted using the tag and probe is biased. This is due to the counting procedure for tags and probes (applied in a 3σ interval around the peak) that looses a fraction of tags or probes if the distributions exhibit a long tail due to inaccurate energy and position measurement induced by the detection holes.

These biases make difficult to give an interpretation to the tag-and-probe efficiency. However, it turns out to be still a useful quantity. Since the correction of the annihilation yield will

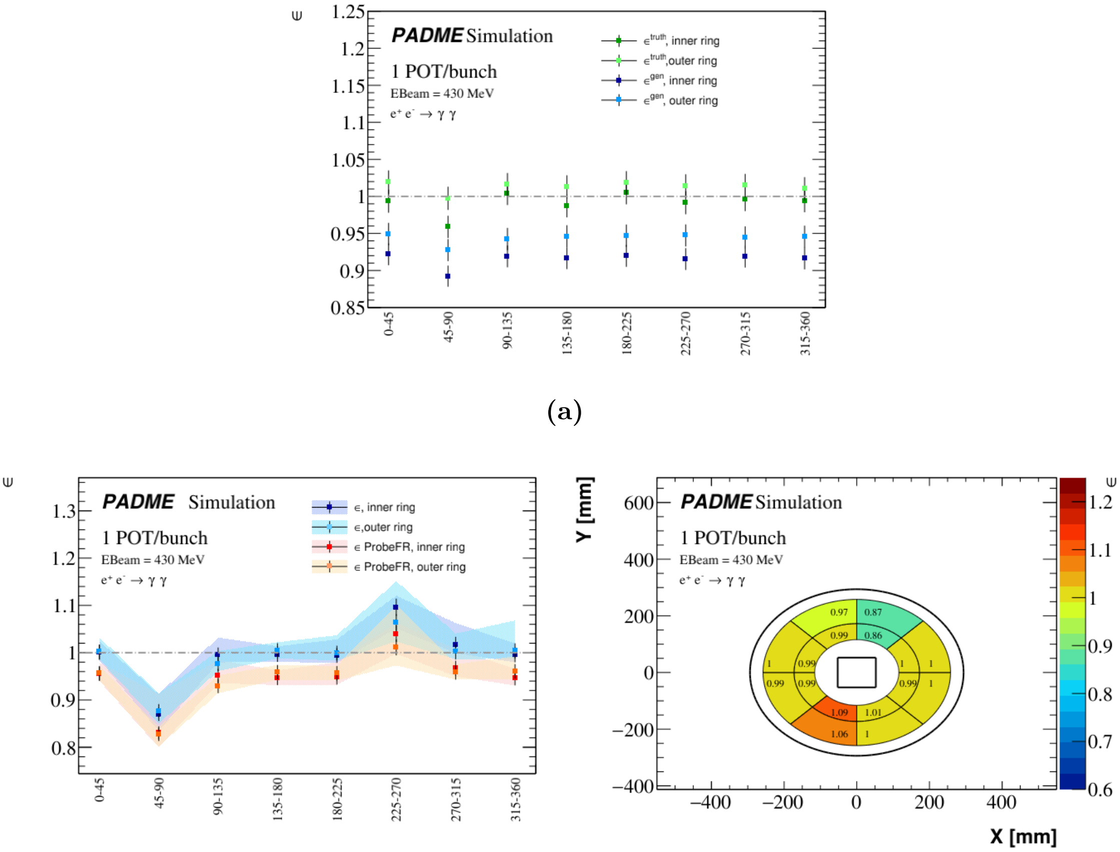

(a)

(b)

(c)

Figure 1.21: *Efficiencies on a simulation where the detector has dead channels. (a) Truth efficiency based on Monte Carlo. (b) Efficiency based on the tag and probe technique. (c) Schematic view of the TP efficiency without any requirement*

be done using $\epsilon(\gamma_1) \times \epsilon(\gamma_2)$ the opposite biases compensate each other. Indeed in the problematic region the efficiency is $0,86 \times 1,08 = 0,93 < 1$. Figure 1.22 (a) shows the truth (green) and TP (blue) event efficiency. The event efficiency from the tag and probe in the problematic bins is slightly lower than the truth event efficiency. This is an expected effect because in the truth efficiency there is no use of the cluster energy. A photon hitting a dead crystal likely produces a small signal in a nearby crystal. The tag and probe selection rejects this cluster (because its energy is not compatible with the expected value). On the other hand, the simple counting of clusters used for the truth efficiency is still taking into account that photon. If an energy threshold is applied when counting clusters to estimate the truth efficiency, the two efficiency determinations become statistically the same, as shown in Figure 1.22 (b).

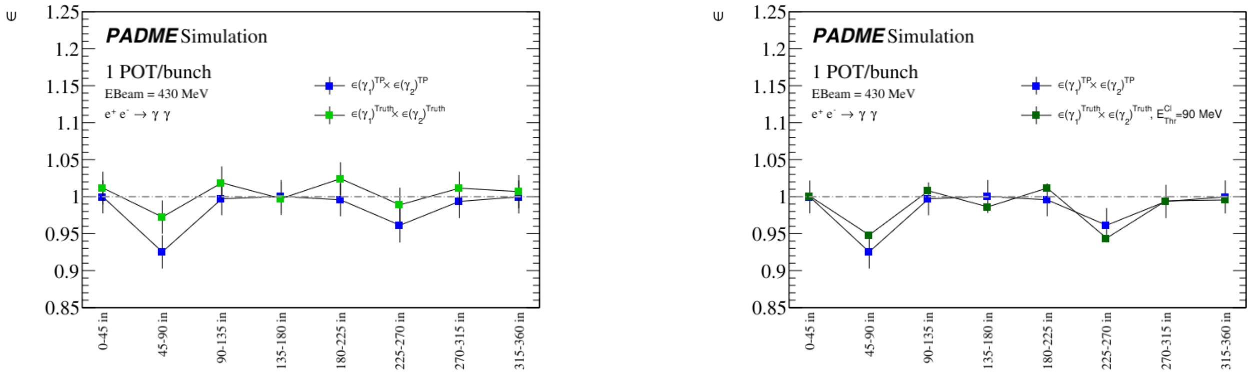

(a) **(b)**

Figure 1.22: *Event efficiency given by* $\epsilon(\gamma_1) \times \epsilon(\gamma_2)$*. On the right, the clusters used for the truth efficiency have a reconstructed energy above* 90 MeV*.*

1.7.2 Measurement strategy based on tag and probe efficiency

The simulation of single annihilation events generated by CALCHEP detector defects and no pileup is used to verify the consistency with truth of the yield of annihilation events after correction for migration at the acceptance boundary and reconstruction efficiency as measured as in data. The simulation described four dead crystals. The tag and probe single photon efficiency for this sample is shown in Figure 1.21. The annihilation candidates are assigned weights described in Figure 1.22.

When candidates are selected requiring the the most energetic photon is in the fiducial region, the efficiencies to be assigned to the photons are the tag and probe efficiency obtained without requiring that the matched probe belongs to the FR and the correction for the migration at the acceptance border in given by Figure 1.13. On the other hand, when the selection requires that both photons are in the FR, the efficiency to be used for the second photon is the one obtained by requiring that the matching probe belongs to the FR and the correction for the migration at the border of the acceptance is in Figure 1.14. This is equivalent to using the efficiency measured with matched probes within the FR for both photons and the correction for migration at the acceptance border in Figure 1.13.

The yield of the annihilation candidates, for this background free sample, is given by the integration of the $ECAL_{g_1} + E_{\gamma_2}$ spectrum in the energy range $[300, 600]$ MeV. Figure 1.23 shows the annihilation peak of all the events that pass the time selection, with the first photon in the FR and the CoG coordinates in 5 cm. Original and corrected yields extracted are reported in Table 1.8. After applying the correction for efficiency and migration at the acceptance boundary the reconstructed yield matches within an error of 0.5% the number of events in the acceptance known from MC truth. This successful closure test validates the tag and probe efficiency measurement and the cross section measurement strategy also in case of local defects of the detector.

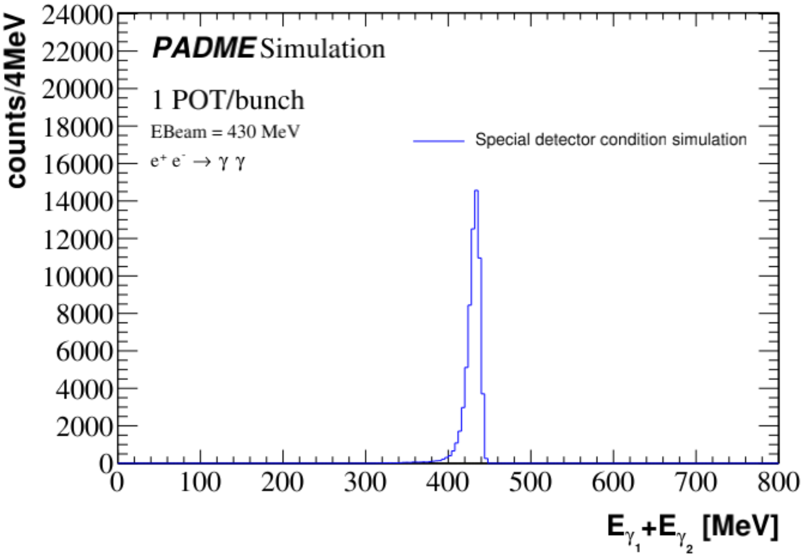

Figure 1.23: *Distribution of the sum of the two photons energy* $E_{\gamma_1} + E_{\gamma_2}$ *for all the events that pass the time selection, with the first photon in the FR and that has the CoG coordinates inside* 5 cm *for a MC sample of single annihilation events and four dead crystals in ECAL .*

Table 1.8: *Annihilation candidates reconstructed in a simulation with detector defects and no pileup. The number of candidates after correction for efficiency and acceptance corrections is also reported along with the number of events in the acceptance at generator level.*

Sample and cut	$\gamma_1 \in FR$	$\gamma_1, \gamma_2 \in FR$
CalcHEP **generation** (expectation)		
$\in FR$	65320	65318
CalcHEP **simulation**		
$\in FR$, $\lvert CoG \rvert < 5$ cm	64006	61041
$\in FR$, $\lvert CoG \rvert < 5$ cm, corrected for $\epsilon_{TP} \times \epsilon_{TP} (\times \epsilon_{TP,probe \in FR})$	65057	65088
$\in FR$, $\lvert CoG \rvert < 5$ cm, corrected for $\epsilon_{TP} \times \epsilon_{TP} \times Acc(\theta_{\gamma_1})$		65649

1.7.3 Measurement strategy based on scale factors

Another strategy for the cross section measurement is to use the efficiency predicted by simulation and corrected with scale factors that allow to match the efficiency in data. The method has been introduced in Section 1.1 and is referred as the “scale factor method”. Here, it will be applied in a special simulation. The tag and probe efficiencies will be used to compute scale factors in a sample of events playing the role of data (with defects) and in a sample of events playing the role of simulation.

Emulating a data and a MC sample

The simulation of annihilation events from CalcHEP in a PADME Monte Carlo with four dead crystals in the top-right quadrant of ECAL (see a hit map in Figure 1.18) has been split in two sub-samples defined as “data” and “MC”:

- sub-sample 1, shown in green in Figure 1.24, is free from detector defects and plays the role of simulation. Sub-sample 1, the “MC” region, can be considered as an imperfect simulation of sub-sample 2, the “data” region. In particular, a one-to-one relation between “MC” and “data” regions is defined by a rotation of $\pi/2$, i.e., a photon at ϕ_L in the “MC” region simulates a photon at $\phi_L + \pi/2$ in the “data” region.
- sub-sample 2, shown in yellow in Figure 1.24, plays the role of data; the detector defects are all located in this region;

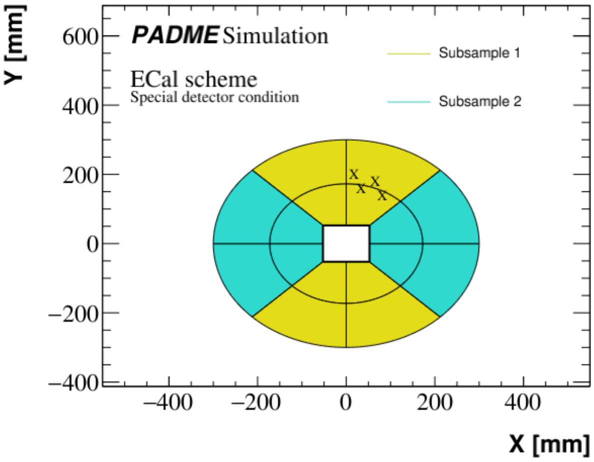

Figure 1.24: *Graphic representation of the two sub-samples.*

The number of annihilation events in the two samples, known from Monte Carlo truth and statistically compatible with each other, is reported in Table 1.9. Two simulations are studies: the first one with a single positron beam, the second with 25000 positrons in each event spread in 250 ns.

Table 1.9: *Number of annihilation events in the sub-sample 1 (MC role) and 2 (data role), known from Monte Carlo truth.*

Sub-sample	Yield
Data	32649
MC	32671

A pileup free simulation

In the absence of pileup, the number of annihilation candidates reconstructed in the “data” and “MC” regions are listed in Table 1.10, along with the selection criteria applied. As expected the dead crystals are responsible of a lower yield in the “data” region.

Table 1.10: *Number of annihilation candidates reconstructed in the “data” and “MC” region from the integration of the distribution of* $E_{\gamma_1}+E_{\gamma_2}$ *in the range* $[300, 600]$ MeV*. Two selections are considered: the first requiring that the leading photon belongs to the FR, the second requiring that both photons are in the FR. No pileup is simulated.*

Sample	**Cut**	$\gamma_1 \in FR$	$\gamma_1, \gamma_2 \in FR$
Data	$\lvert\Delta t\rvert < 10$ ns, $\lvert X(Y)_{CoG}\rvert < 5$ cm	31443	29940
MC	$\lvert\Delta t\rvert < 10$ ns, $\lvert X(Y)_{CoG}\rvert < 5$ cm	32537	31088

As a first step each event passing the selection ($|\Delta t| < 10$ ns, $|X(Y)_{CoG}| < 5$ cm with the first or both photons in the FR) is reweighed according to Equation 1.3 using the tag and probe efficiency measured in the 16 bins and shown in Figure 1.21 (b). The corrected yields, reported in Table 1.11, are in agreement with the expected valued within 1%. It is interesting to observe that in the data region, where there are the dead crystals, the corrected yield is in agreement with the expectation, a confirmation that the bias of the efficiency, clearly visible in Figure 1.21 (b), is compensated in the product $\epsilon(\gamma_1) \times \epsilon(\gamma_2)$.

Table 1.11: *Yield extracted from the annihilation distribution obtained analysing the special detector calchep simulation and corrected for the weights as described in formula 1.3. The yields were extracted integrating the* $E_{\gamma_1}+E_{\gamma_2}$ *spectrum in a fixed range (*$[300, 600]$ MeV*).*

Sample	**Cut**	$\gamma_1 \in FR$	$\frac{\gamma_1 \in FR}{expetation}$	$\gamma_1, \gamma_2 \in FR$	$\frac{\gamma_1,\gamma_2 \in FR}{expetation}$
Data	$\lvert\Delta t\rvert < 10$ ns, $\lvert CoG\rvert < 5$ cm	32429	0.993	32477	0.995
MC	$\lvert\Delta t\rvert < 10$ ns, $\lvert CoG\rvert < 5$ cm	32598	0.998	32594	0.998

As a second step, the number of annihilation candidates is derived with the scale factor method.Therefore, each event in the MC region is rescaled with the product of two scale factors for the efficiency corresponding to each photons.

An efficiency scale factor is defined as follows:

$$f_i = \frac{\epsilon^{TP}(data|\phi_i, R_i)}{\epsilon^{TP}(MC|\phi_i, R_i)} = \frac{\epsilon^{TP}(data|\phi_i + \pi/2, R_i)}{\epsilon^{TP}(MC|\phi_i, R_i)} \tag{1.17}$$

where the efficiency at the numerator, estimated in the “data” region, is the efficiency measured at $\phi + \pi/2$. From these inputs and from the number of reconstructed candidates, the factor C, defined in Section 1.1 is computed and the efficiency-corrected yields summarized in Table ...... are obtained.

This was done for the two analyses related to the request of the most energetic photon or both in the fiducial region. All relevant counters are summarized in Table 1.12. The number of candidates reconstructed in the “data” region, after correction for the efficiency.

Table 1.12: *Annihilation yield and scale factor from “MC” sample and yield after the selection and the correction for “DATA” sample.*

	DATA region		MC region	
	$\gamma_1 \in FR$	$\gamma_1, \gamma_2 \in FR$	$\gamma_1 \in FR$	$\gamma_1, \gamma_2 \in FR$
MC truth	32649		32671	
MC candidates			?	?
MC reweighed scale factor			31627	30065
C			0.968	0.920
Data candidates	31443	29940		
Data corrected for scale factor	32480	32535		

Applying this method it is obtained an yield close to the expected within $0,5\%$.

A simulation with pileup

The simulation used here is the sample of annihilation events from CalcHEP embedded on the GEANT4 simulation of the interaction of 25000 positrons with the target in each event corresponding to a beam bunch. This sample may contain annihilation processes simulated by GEANT4 and, therefore, not recorded in MC truth, in addition to the annihilation event generate by CalcHEP and embedded in the PADME simulation. To keep the ability of comparing reconstructed annihilation events with MC truth, reconstructed candidates are considered only if the two-photon kinematics matches the CalcHEP MC truth for that event. The performance of the matching logic is studied in a pure annihilation simulation without any dead crystals. The variables under study were the photon energy and azimuthal angle. The differences $\Delta E = E_\gamma - E_{cl}$ and $\Delta\phi = \phi_\gamma - \phi_{cl}$ between generated and reconstructed values for all events passing the selection cuts a, b and c described in Section 1.4 are shown in Figure 1.25 (a) and (b) for a pileup free simulation.

The matching requirements applied are $|\Delta E| < 50$ MeV and $|\Delta\phi| = 180$ Deg(care is taken to treat correctly the case of $\Delta\phi = 180$ Deg , occurring when reconstructed photons are matched to the MC truth of the second photon in the event).

The effect of the matching is heavier when the detector has defects; this has been verified using the simulation of ECAL with 4 dead crystals in the top right quarter. The same procedures applied to this simulation separately for the data region (where defects lie) and the MC region (where the detector has no defects) gives counts summarised in Table 1.13. From these results, and from Table 1.10 where the number of annihilation events from MC truth is reported, the efficiency of the matching criterion in the data region is found to be $\beta = \frac{30809}{31443} = \frac{29313}{29940} = 0.98$ for the data region.

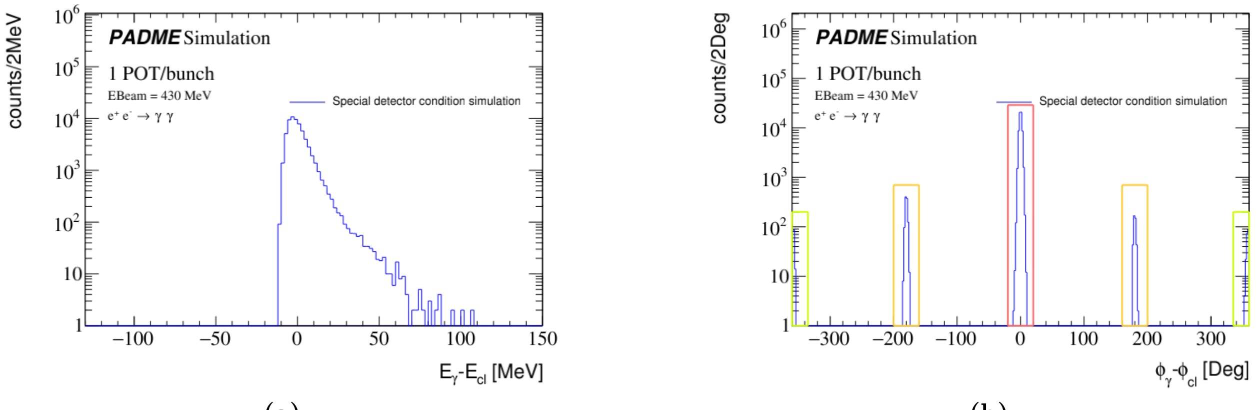

(a) **(b)**

Figure 1.25: *Left: distribution of $\Delta E = E_\gamma - E_{cl}$ for the events that pass the selection cuts a, b and c described in 1.4 for a pure annihilation simulation.*

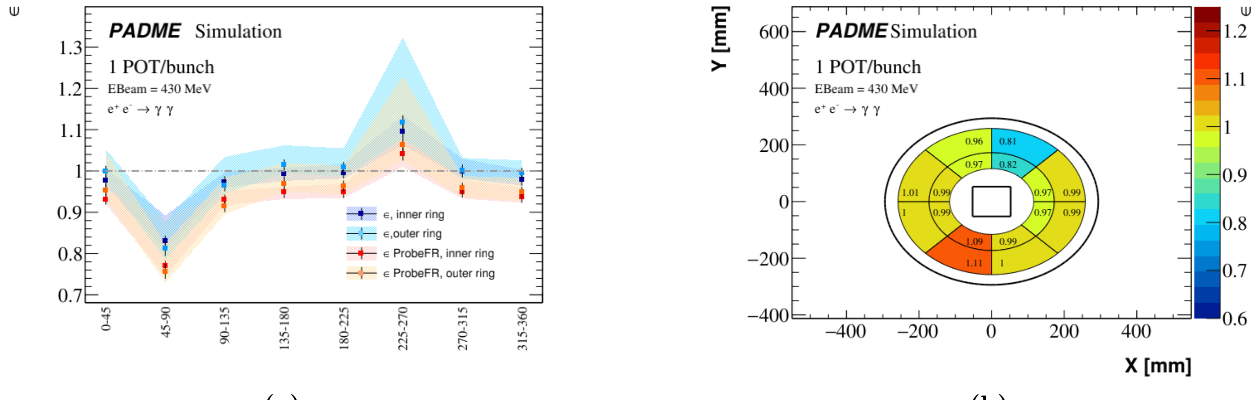

(a) **(b)**

Figure 1.26: *Tag and probe efficiency for MC simulation of CalcHEP with pileup. In (b) a schematic view of efficiency measured without any requirement.*

Taking these effects into account, the number of annihilation candidates selected in the sample with pileup is corrected with the tag and probe efficiency measured in the same sample shows in Figure 1.26. The results, reported in Table 1.14 for the data and the MC region, show a very good match with MC truth, both for the selection with the leading photon in the FR and for the selection with both photons in the FR.

After applying these requirements, the number of annihilation processes from CalcHEP passing the matching criterion was 65067 instead of 65172, corresponding to a 0.2% inefficiency of the matching criterion in absence of pileup and without any detector problems. In presence of pileup (25×10^3 POT/bunch) the number of annihilation that pass the MC truth matching is 65342, 0.3% more than expected (65172) due to a residual GEANT4 contamination.

In addition the scale factor method has been applied, following the same approach described

Table 1.13: *Yield extracted from the annihilation distribution obtained analysing the special detector calchep simulation in order to extract the performance on the consistency selection.*

	$\gamma_1 \in FR$		$\gamma_1, \gamma_2 \in FR$	
Sample	Without consistency	Consistency applied	Without consistency	Consistency applied
Data	31443	30809	29940	29313
MC	32537	32489	31088	31042

Table 1.14: *Yield extracted from the annihilation distribution obtained analysing the special detector calchep simulation with and without the consistency check corrected for the tag and probe efficiency.*

	$\gamma_1 \in FR$		$\gamma_1, \gamma_2 \in FR$	
Sample	Weighted w/o consistency	Weighted, Consistency applied	Weighted w/o consistency	Weighted, Consistency applied
Data	32429	31765	32477	32553
MC	32598	31784	32594	32548

for the simulation without pileup. The results are summarized in Table 1.15.

Table 1.15: *Annihilation yield and scale factor from "MC" sample and yield after the selection and the correction for "DATA" sample applied to CalcHEP simulation with pileup.*

	DATA region		MC region	
	$\gamma_1 \in FR$	$\gamma_1, \gamma_2 \in FR$	$\gamma_1 \in FR$	$\gamma_1, \gamma_2 \in FR$
MC truth	32649		32671	
MC candidates			?	?
MC reweighed scale factor			31583	30022
C			0.967	0.919
Data candidates	31443	29940		
Data corrected for scale factor	32516	32579		

The results of the various closure tests performed in the simulation are very satisfactory also in the difficult case of pileup of interaction in a detector with some dead crystals.

In summary, a long list of checks discussed in this section allow to gain strong confidence on the tag and probe technique for the efficiency measurement and and the cross section measurement strategy that will be applied for the analysis of the PADME data.

1.8 Background subtractions

In Chapter 3 the background in PADME, and in ECAL in particular, has been widely discussed comparing data collected in RunI and in RunII, after the commissioning of the beam line. Despite the big improvement in the quality of data collected in RunII, the occupancy of the electromagnetic calorimeter is still dominated by beam induced background. In addition, the simulation of the beam line with all relevant materials along with the focusing and bending magnets is a very complex task. An important effort has been done in the collaboration to achieve the goal of a realistic simulation of the beam line, however a tuning of such simulation suitable to describe the data of RunII has not yet been completed. This situation implies that the subtraction of the background, both in the selection of the annihilation events, and in the selection of tag (and probe) photons for the data-driven efficiency measurement, requires a special effort.

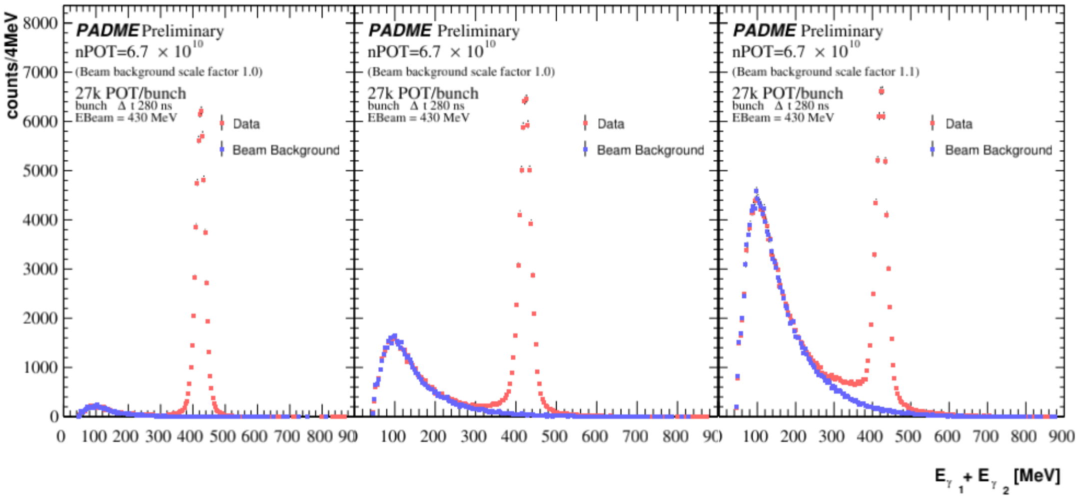

Figure 1.27: *Distribution of* $E_{\gamma_1} + E_{\gamma_2}$ *of the two photons that pass the selection a.b. described in Section 1.4 for standard run (red dots) and special one with target out of the target beam (blue dots). (a) additional selection CoG cut of* 20 mm*; (b) additional selection CoG cut of* 50 mm*; (c) additional selection CoG cut of* 80 mm.

Figure 1.27 shows in red the distribution of the sum of the energies of the two photons passing a selection for annihilation events in data. The three plots refer to a different thresholds for the x and y coordinates of the center of gravity: 20, 50 and 80 mm. The peak at 430 MeV, corresponding to the signal events, overlaps with a shoulder related to combinatorial background whose relative importance is as bigger as looser is the cut on the center of gravity. Figure 1.28 shows the same distributions obtained by applying the same selection to a simulation of annihilation events with the pileup of physics background from the interactions of 25000 positrons per bunch in the target. In this case the background is smaller in size and different in shape with respect to the background observed in data.

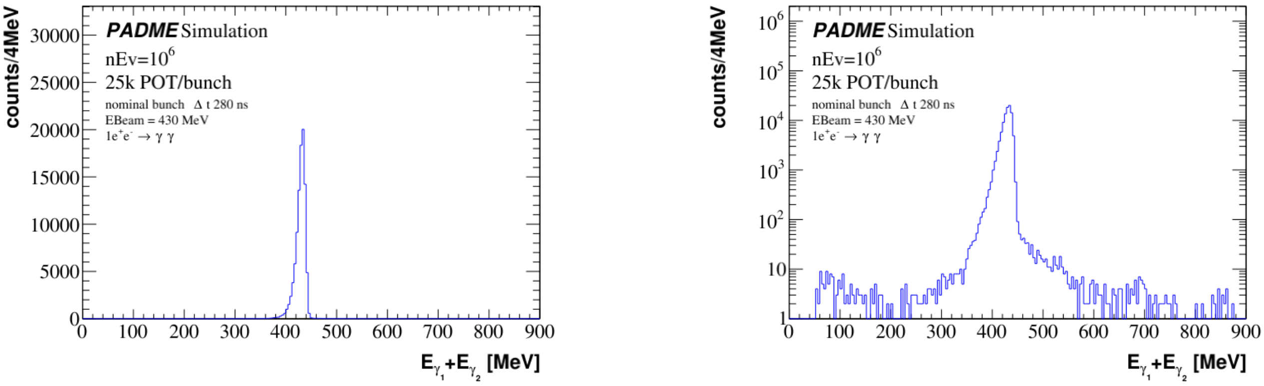

(a) (b)

Figure 1.28: *Distribution of $E_{\gamma_1} + E_{\gamma_2}$ of the two photons that pass the selection a.b.c. described in Section 1.4 for CalcHEP simulation with pileup.*

Much more severe is the problem of background subtraction for the selection of tag photons. This is shown, for data in Figure 1.29 (a) and in the simulation with pileup in Figure 1.31 (a). Eventually, the distribution of the photon identified as matched probes is almost free of background, therefore the shape of the distribution observed in data (Figure 1.30 (a)) is similar to the distribution in the simulation Figure 1.31 (b).

A fundamental help comes from the samples of data recorded with the diamond target removed from the beam line. In these data samples the signals recorded by the PADME detectors are produced only by beam related background and by positrons in the tail of the beam spot interacting in passive materials surrounding the target. In Figure 1.27 the distribution in blue superimposed to the data represent the result of the annihilation selection applied to no-target data with a normalization adjusted in order to match the amplitude of the background shoulder in the distribution in red observed the canonical data. The distribution corresponding to signal events can be obtained as the difference between the nominal and the background distributions. The same strategy can be applied in the case of the selection of tag photons. In Figure 1.29 (b) the distribution of ΔE_{tag} obtained in no-target data is shown. Figure 1.29 (c) shows the overlap of this distribution to the same distribution obtained in nominal data. Finally the distribution for tag candidates subtracted by the background estimated with the no-target data is shown in Figure 1.29 (d).

The background is normalised equalizing the integral of the distribution of no-target and nominal data in the range $\Delta E_{Tag} \in [-150, -90]$ MeV. For consistency the same background subtraction procedure is applied to the distribution of ΔE_{probe} for the matched probe candidates. One should observe that the no-target data are suitable to describe the beam induced background, but they do not describe the sub-dominant contribution of the background arising from the pileup of interactions of the high intensity beam in the target. The relative importance of beam induced background and background from the pileup can be assessed by comparing the simulation with pileup and the data for the selection of candidate tag-photons, i.e. Figure 1.29

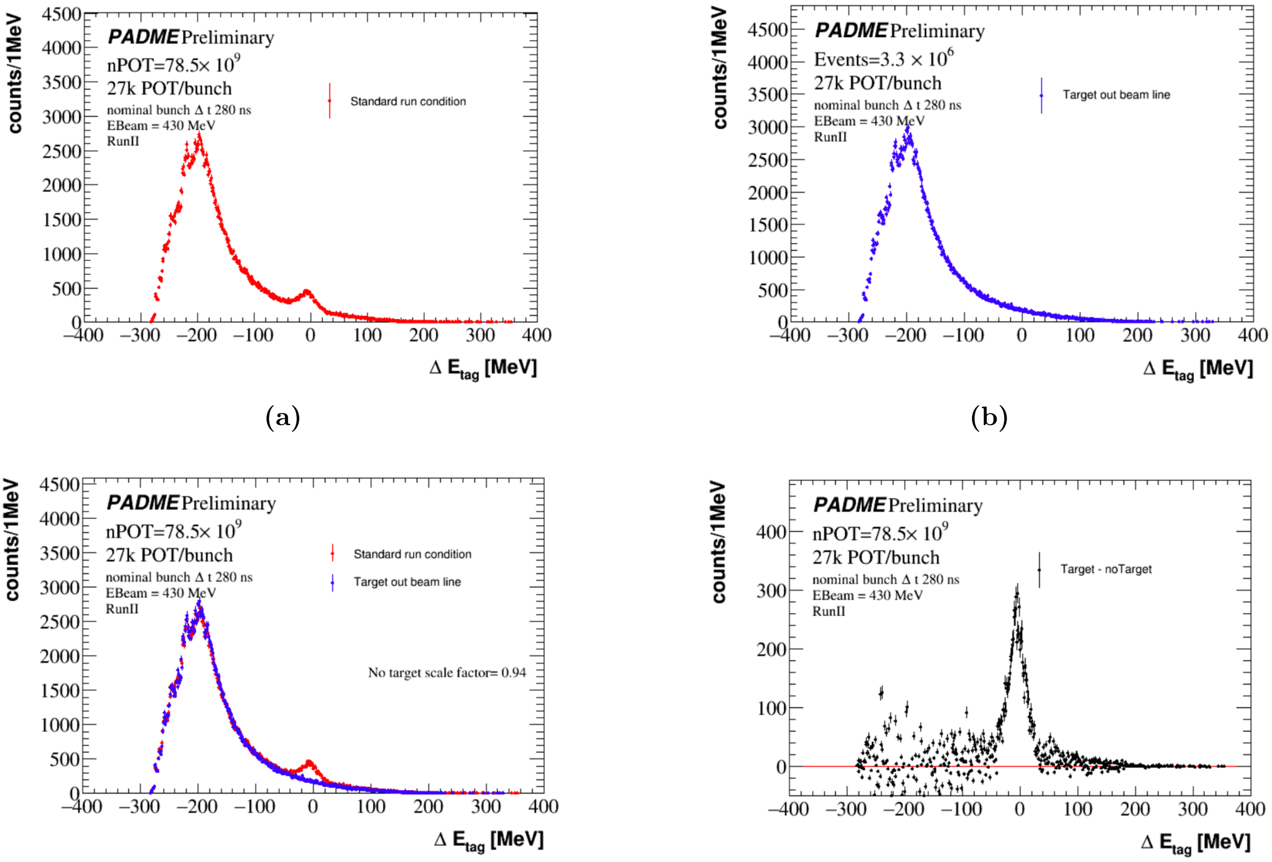

(a) (b) (c) (d)

Figure 1.29: *(a): Distribution of the* $\Delta E = E_{cl} - f(\theta)$ *of the tag distribution in a standard run condition. (b): Distribution of the* $\Delta E = E_{cl} - f(\theta)$ *for background, distribution of the events token with the target out of the beam line. (c): Comparison of (a) and scaled (b). (d) : Tag yield, obtained from the subtraction of the background on the signal.*

(a) and Figure 1.31 (a). In the assumption that the contribution of pileup can be ignored, the procedure described in Section 1.6.1 can be applied to estimate the number of tag-photons and matched probes after background subtraction using the no target data. This allows to estimate the tag and probe efficiency and its systematic variations in all 16 bins of ECAL . The results are shown in Figure 1.32 for all matched probes and for matched probes requested to belong to the FR. They exhibit an unclear pattern with respect to the known features of ECAL, in addition to biases indicated by few values higher than one.

The known defects of ECAL in RunII data , that can be observed in Figure reference to map of chapter 3 (a two-dimensional cluster map) and Figure 1.33 (a two-dimensional map of candidate photons from annihilation), are:

- 3 dead crystals: one in the external bin of slice $270 - 315$ $rmDeg$, one in the external bin of slide $315 - 360$ Deg; the third at the inner border of the FR at the boundary between

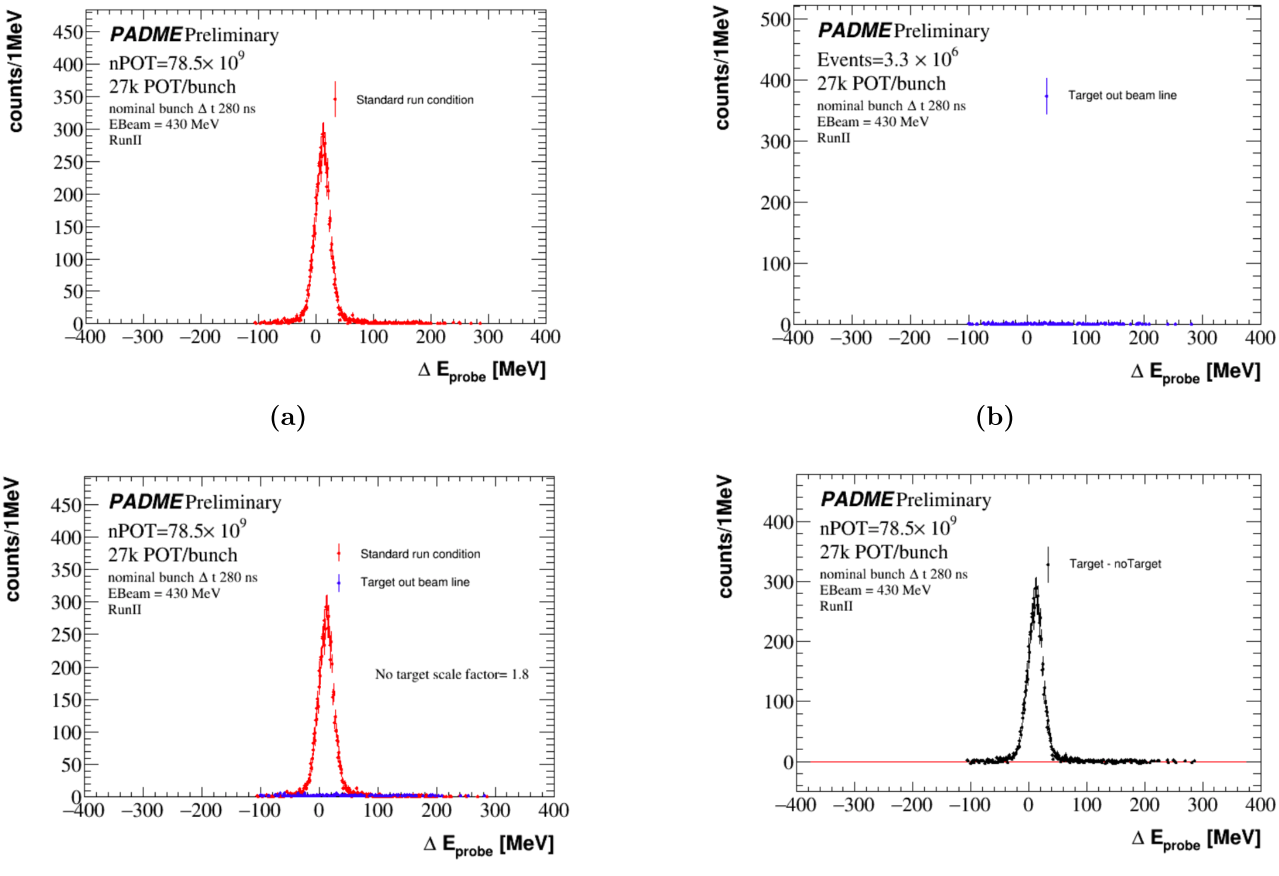

(a) **(b)** **(c)** **(d)**

Figure 1.30: *(a): Distribution of the* $\Delta E_{Probe} = E_{cl} - (E_{Beam} - f(\theta_{Tag}))$ *of the probe matched distribution in a standard run condition. (b): Distribution of the* ΔE_{Probe} *for background, distribution of the events token with the target out of the beam line. (c): Comparison of (a) and scaled (b). (d) : Probe yield, obtained from the subtraction of the background on the signal.*

slice $270 - 315$ Deg and slice $315 - 360$ Deg;

- a reduction of the acceptance at the top and at the bottom of the fiducial region appearing as a shadow from inert materials (presumably the top and bottom walls of the vacuum chamber at the exit of the magnet dipole); this effect is seen also in simulation and in data it causes a slightly larger effect at the bottom of ECAL, suggesting some mismodeling of the vertical offset of ECAL with respect to the vacuum chamber;

- in some runs a a few adjacent crystals in the top-right quarter have a low efficiency due to a DAQ problem. Some of these features can be recognised in the efficiency map of ECAL shown in Figure **??**, but other unclear effects show up in these measurements; also they appear rather sensitive to the criteria applied to count signal tags and probes in the distributions obtained after background subtraction.

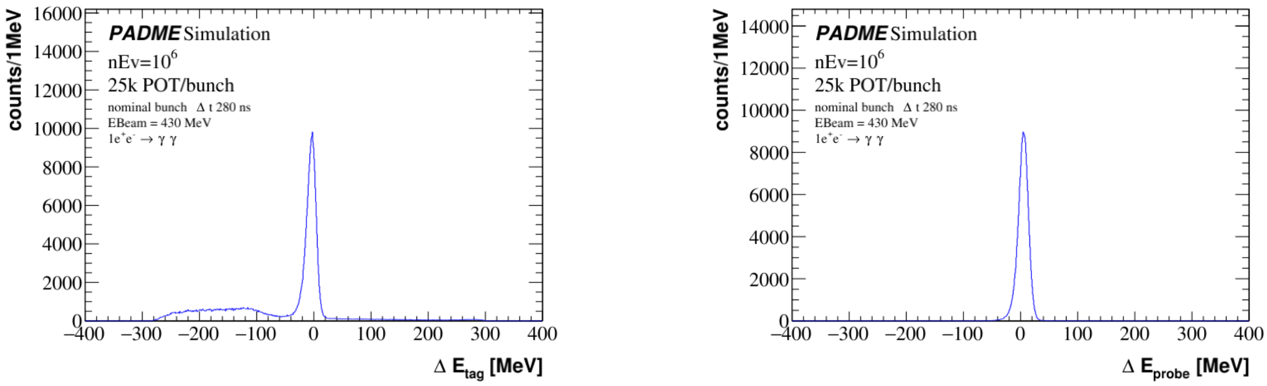

(a) (b)

Figure 1.31: *(a): Distribution of the* $\Delta E = E_{cl} - f(\theta)$ *of the tag and (b) of the* $\Delta E_{Probe} = E_{cl} - (E_{Beam} - f(\theta_{Tag}))$ *for CalcHEP simulation with pileup.*

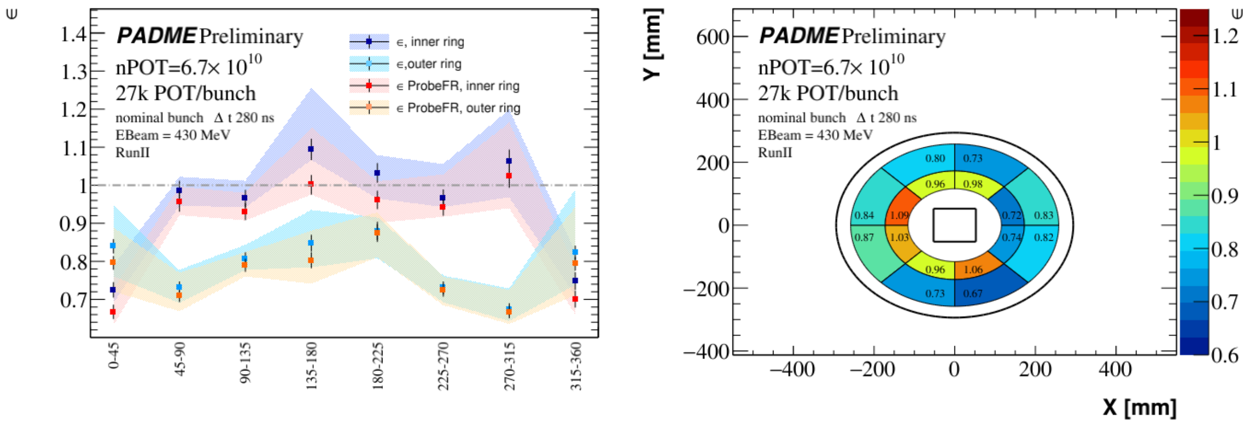

(a) (b)

Figure 1.32: *(a): Trend of the efficiency for bins in the inner ring in blue and outer once in light blue; in addition is reported the efficiency time the visible acceptance extracted requiring the probe in the FR (red for inner ring bins and orange for outer ring bins); (b) schematic view of the measured efficiency.*

As a consequence a few improvements have been introduced in the overall data analysis process, affecting on one side the data driven efficiency determination and on the other side the measurement of the number of annihilation candidates. They will be applied for the derivation of results in the next section. They are briefly anticipated here:

- The overall rate of background photon candidates will be reduced by applying a pre-selection of photons according to shape parameters for the clusters discriminating signal photons form background;

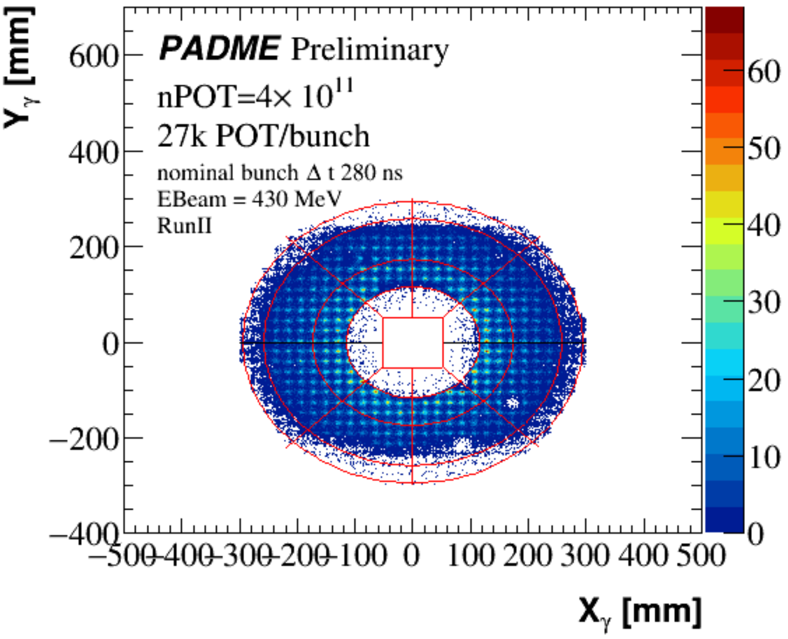

Figure 1.33: *Map of the annihilation photons candidates passing the selection a.b.*

- The distribution of ΔE_{tag} has been subtracted of the background by considering the contribution of beam related background and pileup; the shape on the beam background is inferred from no-target data while the shape of the background from pileup is predicted by simulation. The normalization of both of them will be obtained from a fit to the data;
- The yield of annihilation events will be obtained from the distribution if the difference in phi between a photon and the direction expected from the other photon; the background contamination is easily subtracted since it is flat under the signal peak;
- a correction of the position of ECAL in the PADME reference frame, where the z axis is defined as matching the direction of the incoming beam, will be applied leading to a distribution of the annihilation candidates symmetric in the calorimeter, after correction for the local inefficiencies. This will be determined using survey measurements and further corrections derived from data.

1.9 $e^+e^- \to \gamma\gamma(\gamma)$ cross section measurement

1.9.1 Pre-selection

A first screening of the events was done in order to chose only events where a beam bunch arrives in the experiment, this is possible by choosing event triggered by the hardware trigger of the BTF beam.

However, even when the PADME trigger board receives the BFT trigger signal, it can happen that the event is empty, typically because of a late update of the BFT trigger signal after beam loss.

In addition, another problem can be observed looking at Figure 1.34 where the N_{POT} distribution for the events triggered by the BTF signal is shown for run $N = 30563$. Up to 70 kPOT/bunch were estimated in a few cases. To solve both these problems in each run, events with a measured number of positrons in the bunch above or below five sigma from the average bunch multiplicity have been discarded. The reason of this cut lie the fact that if the target is reconstructing correctly the bunch multiplicity, events out the 5σ have a different beam background level and are affected by the pileup differently with respect to a typical event. On the other hand, instead events where the signals readout from the strips of the Diamond target lead to an extremely low or unrealistically high measurement of the total charge lead to a wrong assessment of the number of positrons in the bunch. Although the occurrence of such events is low, they may introduce biases in the measurement of the total number of positrons on target.

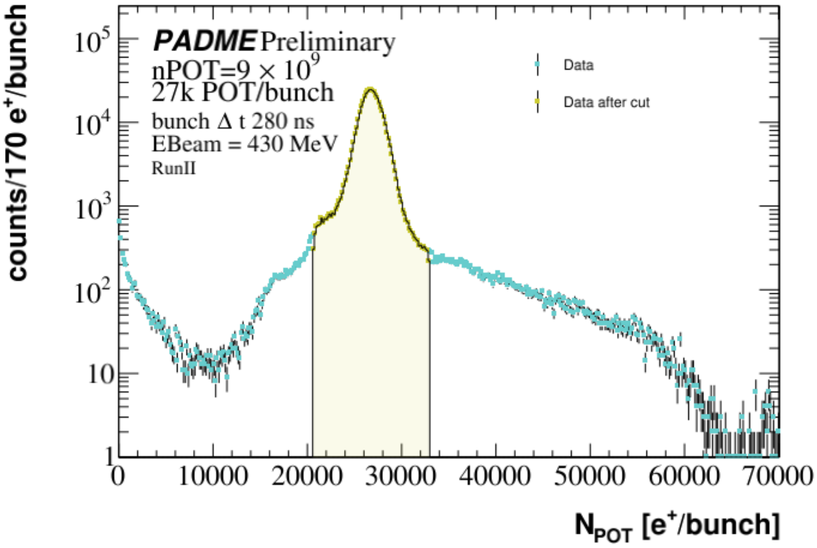

Figure 1.34: *Distribution of the Number of Positrons On Target per bunch for run $N = 30563$ (azure distribution). In yellow is reported the N_{POT}/bunch distribution of the events that pass the multiplicity selection.*

In Table 1.16 the number of events for each runs before and after the luminosity selection are reported along with the fraction of events retained.

1.9.2 Photon pre-selection

In Chapter data taking) it has been shown that even in RunII the PADME electromagnetic calorimeter receives a high rate of background particles, from beam related spurious interactions. Most of the times the resulting energy deposits have low energy, therefore the features

Table 1.16: *For each run analysed the number of events triggered by the BTF trigger signal, the number of events passing the luminosity selection and their ratio are reported.*

Run number	N_{ev}^{BTF}	$N_{ev}^{5\sigma}$	$\frac{N_{ev}^{5\sigma}}{N_{ev}}$
30369	2961470	2820916	$0,953$
30386	1437248	1307072	$0,909$
30547	2232745	2140028	$0,958$
30553	785728	746250	$0,95$
30563	2243220	2101791	$0,937$
30617	2206172	2086402	$0,946$
30624	2234949	2106551	$0,943$
All	14000000	13300000	$0,95$

of the corresponding clusters are statistically different from those of photons of energy above about 90 MeV that, as we will see later, are involved with the annihilation process. Therefore a cluster selection is applied in order to reduce the contamination of the cluster collection and improve the rejection of background.

Cluster quality requirements

Several features of the clusters corresponding to a tight selection of annihilation events have been studied and contrasted with the same quantities observed in the overall sample of clusters. The selection of annihilation photon candidates was based in the following requirements: at least two clusters must be found in ECAL with $|t_{\gamma_1} - t_{\gamma_2}| < 10$ ns, $|\Delta\phi| = |\phi_{\gamma_1} + 180° - \phi_{\gamma_2}| < 25°$, $|CoG_{X(Y)}| < 5$ cm, $300 < E_{\gamma_1} + E_{\gamma_2} < 500$ MeV [5]. In addition the most energetic cluster in the pair was requested to be at a radial distance with respect to the direction of the incoming beam bigger than 115.82 mm.

The distributions (with arbitrary relative normalization) of the variables studied are reported in Figure 1.35 for all clusters (azure distribution) and for annihilation candidate photons. For each variable, a loose cleanup cut was defined to avoid compromising significantly the efficiency for signal photon. In the following the relevance of each variable is briefly described:

- the distance between the cluster position and its seed is peaked at zero in both the X and Y directions (see Figure 1.35 (c) and (d)), large distances may only be due to anomalous situations related for example by pileup; therefore only clusters with $R_{cl-seed} = (X_{Cl} - X_{seed})^2 + (Y_{Cl} - Y_{seed})^2 < 20$ mm are retained;

- X and Y RMS, defined as

$$\sqrt{\frac{\sum_{i=0}^{n_{hit\in Cl}} (X(Y)_i - X(Y)_{Cl})^2 E_i}{\sum_{i=0}^{n_{hit\in Cl}} E_i}}, \tag{1.18}$$

---

[5] The definition of x, y_{CoG} and the motivations of these cuts will be explained in Section 1.4

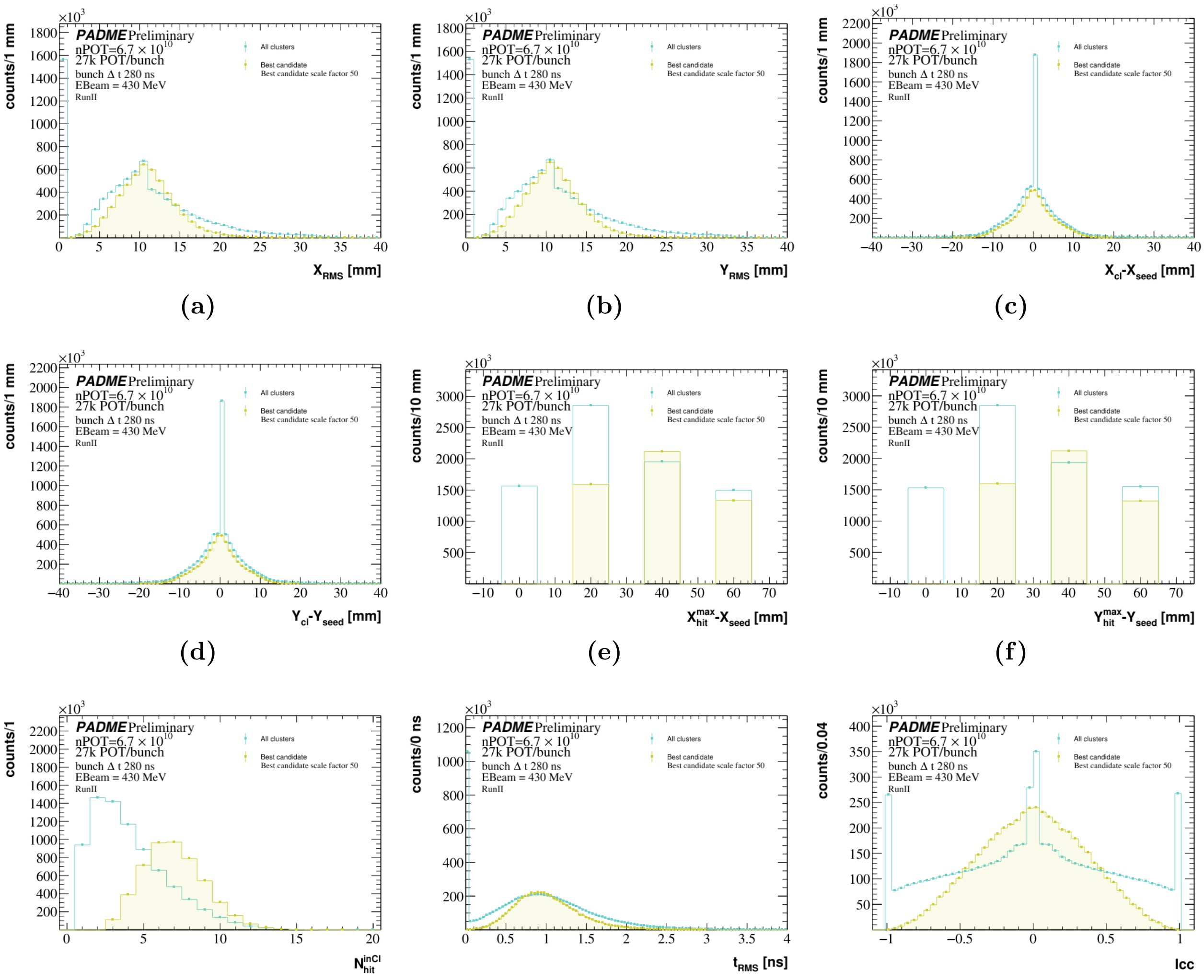

(a) (b) (c)

(d) (e) (f)

(g) (h) (i)

Figure 1.35: *Cluster features, used to improve the quality and reduce the background contamination of the cluster sample, for all clusters (azure distributions) and annihilation candidate photons (yellow distribution): (a) RMS of X coordinates for hits in cluster, (b) RMS of Y coordinates for hits in cluster, (c) distance of cluster position from its seed in the X and Y (d) direction (e) maximum distance between a hit in the cluster and the seed in the X and Y (f) direction, (g) cluster size, (h) time RMS, (i) linear correlation coefficient of hits in the cluster.*

are shown in Figure 1.35 (a) for X and (b) for Y RMS. A comparison between generic clusters and annihilation candidates suggest to reject clusters with $X(Y)_{RMS} \leq 1$ mm;

- the maximum distance between hits in a cluster and the cluster position along X and Y axis (Figure 1.35 (e) and (f)) is requested to be $\Delta X(Y)^{max} \geq 1$ mm in order to discard the occurrence of signals from noise in an isolated crystal;

Table 1.17: *Cluster quality requirements and fraction of clusters passing each cut with respect to those passing the previous cut.*

Quality cut	$\frac{N_i}{N_{i-1}}$
$R_{Cl-seed} < 20$ mm	0.96
$X_{RMS} \geq 1$ mm	0.79
$Y_{RMS} \geq 1$ mm	0.90
$\Delta X^{max} \geq 1$ mm	1.
$\Delta Y^{max} \geq 1$ mm	1.
$\|lcc\| \leq 0.99$ mm	0.92
t_{RMS}	0.996
Isolation	0.85

- the cluster distribution size, reported in Figure 1.35 (g), shows that candidate photons have an average multiplicity of 7 hits per cluster, thus a threshold was defined $N^{inCL}_{hits} > 1$;
- the RMS of the time distribution of hits in a cluster, defined similarly to the X(Y) RMS, is shown in Figure 1.35 (h) and a value not exceeding 3 ns is requested;
- the linear correlation coefficient of hits in the cluster given by

$$lcc = \frac{\sum_{i=0}^{n_{hit}}(X_i - Xcl)(Y_i - Ycl)E_i}{\sum_{i=0}^{n_{hit}} E_i \times X_{RMS} \times Y_{RMS}} \tag{1.19}$$

  is reported in Figure 1.35 (i); only values below 0.99 are accepted;
- finally an isolation requirement is applied: a photon is rejected if another cluster in a time within 10 ns is found closer than 200 mm.

The sequence of cuts applied to the ECAL clusters rejects 53, 8% of them with the relative efficiency cut flow reported in Table 1.17. The fraction of the signal rejected is the 10% given by (number of probe that pass NPotSelection and ClQuality / number of probe that pass only NPOTSelection)/2 - I divided for 2 to consider also the number of tag, since I select a probe if I found the tag....How I can explain this now?.

Figure 1.36 shows how this pre-selection of the clusters in ECAL allows to reduce the background in the tag selection, leaving the signal almost unaffected.

1.9.3 Event selection

The measurement of the yield of annihilation events is based on a fit of the distribution of the variable $\Delta\phi = \phi_{\gamma_1} - \phi_{\gamma_2} - 180°$. This variable has the big advantage of being affected by a background almost flat in shape. Figure **??** shows this variable for the entire data sample; the same distribution observed in the no target data is superimposed for comparison, showing that

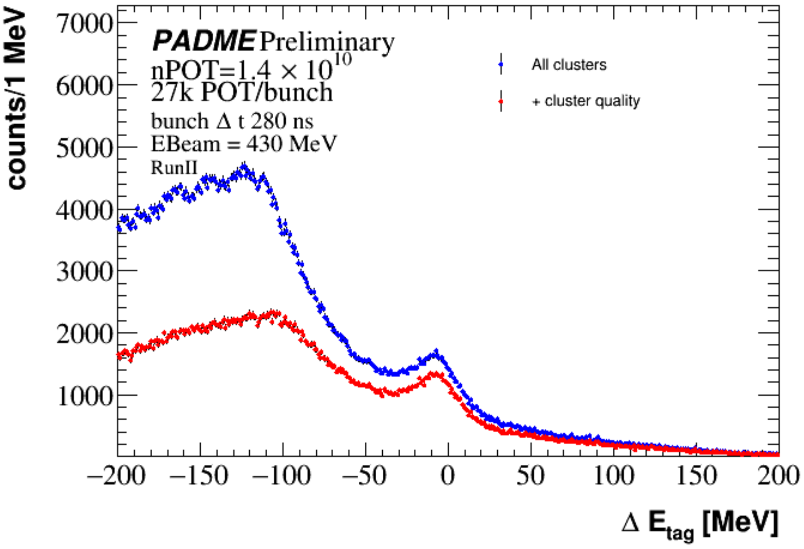

Figure 1.36: *ΔE_{Tag} distribution of identified tag belonging the fiducial region in blue. The same distribution is reported in grey for events that pass the $nPOT$ selection and in red the photons that pass also the cluster quality cuts.*

the beam related background reproduces the flat behaviours of the signal side-bands in nominal data.

The two photons annihilation yield is obtained by fitting the $\Delta\phi$ distribution with a background and signal function represented by a second order polynomial and a gaussian. The event selection has been designed in order to be as efficient as possible for signal events, benefiting of the reduction of the background coming from the clean-up of the photon candidates. The requirements applied are summarized in Table 2.2 along with the number of PADME events in the data sample (described in Section add reference) surviving each cut. correct table The number of signal events N_{sig} is defined as the total number of candidates N_c with $|\Delta\phi| < 40°$

Table 1.18: *Data analysis cut-flow.*

Cut	
N of pre-selected events	13×10^6
N pairs of good clusters in ECAL	20×10^6
$E_{\gamma_1} > 90$ MeV	16×10^6
$E_{\gamma_2} > 90$ MeV	7×10^6
$R_{\gamma_1} \in FR$	3×10^6
$\lvert\Delta t\rvert < 10$ ns	4×10^5
$\Delta E(\theta_{\gamma_1})$	3.8×10^5
$\Delta E(\theta_{\gamma_2})$	3.2×10^5

subtracted of the number of background events estimated by the fit:

$$N_{Sig} = N_c - N_{Bkg}^{fit} \tag{1.20}$$

where $N_{Bkg}^{fit} = \int_{-40}^{40} P2(x)dx$.

A data-driven geometry correction

In order to verify the consistency of the measured yield, the ECAL calorimeter was divided in 8 azimuthal slices and the annihilation candidates have been assigned to each slice according to the value of ϕ_{γ_1}, i.e. the azimuthal angle of the most energetic photon in the pair. The uniformity predicted by physics can be altered only by variations of the reconstruction and identification efficiency associated to detector defects. Table 1.19 summarizes the yields of the annihilation candidates in each bin for run 30563. These results are also graphically shown in Figure 1.37 left, where one can easily observe that the top part of ECAL seems to be depleted. A lower number of candidates in the top and bottom regions might be expected due to the known interference of the vacuum chamber walls with the trajectories of photons from the target. However, the top-bottom asymmetry is not expected and may be interpreted as an indication of a vertical offset between beam and ECAL. Indeed, a campaign of survey measurements on the experimental apparatus found a position of the center of ECAL in the PADME reference frame given by $(x_c, y_c) = (-3.13, -3.86)$ mm.

Table 1.19: *Annihilation yields derived from the $\Delta\phi$ distribution for each azimuthal ECAL bin and the ratio of the yields with respect to the highest one. In the latest two columns are reported the yield and the ratio for the annihilation yield after the correction.*

			γ position correction	
ϕ Deg **range**	N_{sig}	$\frac{N_{sig}}{N_{sig}^{max}}$	N_{sig}	$\frac{N_{sig}}{N_{sig}^{max}}$
$[0, 45]$	1227	0.85	1352	1
$[45, 90]$	899	0.62	966	0.71
$[90, 135]$	866	0.60	901	0.67
$[135, 180]$	1316	0.91	1295	0.96
$[180, 225]$	1451	1	1294	0.96
$[225, 270]$	1290	0.90	1182	0.87
$[270, 315]$	1091	0.75	1089	0.81
$[315, 360]$	1334	0.92	1332	0.99

After this general correction of the PADME geometry was applied in the reconstruction software, the distribution of the x and y coordinates of the center of gravity of the two photons from annihilation candidates was studies separately for all runs. The aim of the study was to observe in data the run-dependent offset of the beam position with respect to the PADME reference frame. Indeed corrections of the order of 1 mm were derived for each run and applied

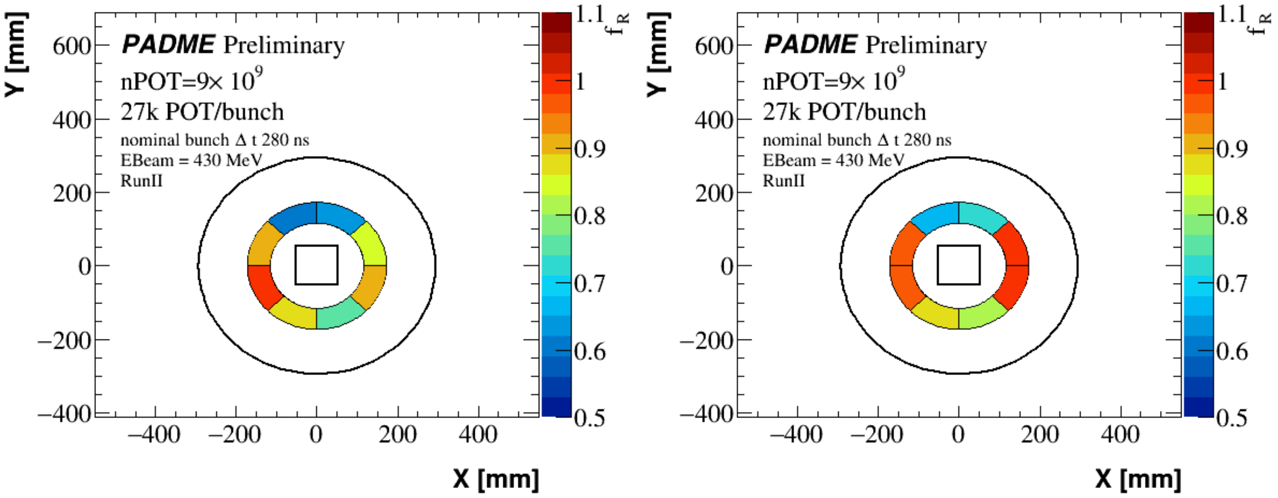

(a) (b)

Figure 1.37: *Schematic view of the yield of annihilation candidates in eight slices of ECAL. The number of candidates is normalised to the highest value observed. Each annihilation candidate is assigned to the slice where the most energetic photon in the pair lies. Before (a) and after (b) the geometry correction.*

to correct the geometry on a run by run basis. The distribution of the annihilation candidates after these corrections is shown in Table 1.19 and in Figure 1.37 right. Here one can see that the left-right and top-bottom symmetry of the yield is improved. The remaining differences will be described and corrected through the data driven efficiency measurement. Indeed the condition where the number of annihilation candidates corresponds to the case of the most energetic photon in the inner ring of the third phi slice; this photon must be paired with a second one in the outer ring of the seventh slide where one dead crystal is located in addition to the reduction of efficiency due to shadow from the bottom section of the vacuum chamber walls at the exit of the dipole. In summary the patters of the yield is now matching the features of the detector.

The corrections described here were studied and applied before the cluster pre-selection was implemented, therefore the numbers of candidates reported in Table 1.19 are given here just to describe the effect of the run dependent geometry correction, while the final number of candidates obtained at the end of the entire chain of selection, on data corrected for these effects are reported in Table 1.20.

1.9.4 Yield of annihilation candidates

The number of annihilation candidates finally obtained from the entire data set and divided in the 8 slides of ECAL are reported in Table 1.21. The distributions of the $\Delta\phi$ coordinates used to derive them are shown in Figure **??**, with the distribution for the entire data set shown in 1.38. In addition, the selection has been applied separately in the different runs and the

Table 1.20: *Annihilation yields measured fitting the background of the $\Delta\phi$ distribution for each azimuthal ECAL bin and the relative ratio of the yields with to respect the higher one for events passing the event and photon selections.*

			ϵ correction	
ϕ Deg **range**	N_{sig}	$\frac{N_{sig}}{N_{sig}^{max}}$	N_{sig}	$\frac{N_{sig}}{N_{sig}^{max}}$
$[0, 45]$	38783	1	66183	0.978
$[45, 90]$	28611	0.738	61266	0.905
$[90, 135]$	26517	0.684	62688	0.926
$[135, 180]$	37436	0.965	64656	0.955
$[180, 225]$	38779	1	67325	0.995
$[225, 270]$	36293	0.936	61828	0.914
$[270, 315]$	35329	0.911	64824	0.958
$[315, 360]$	36069	0.93	67672	1

Table 1.21: *Yield as a function of the phi slice and of the selection.*

ϕ [Deg]	$N_{\Delta\phi}$	$N_{\Delta E_{In}}$	$N_{MM^2_{In}}$	$N_{\Delta E_{Out}}$	$N_{MM^2_{Out}}$
$[0, 45]$	38780 ± 200	46950 ± 760	46920 ± 900	57000 ± 1300	57600 ± 670
$[45, 90]$	28610 ± 170	46730 ± 520	48720 ± 350	45300 ± 470	46100 ± 550
$[90, 135]$	26520 ± 160	53700 ± 1400	50040 ± 930	46320 ± 800	46800 ± 420
$[135, 180]$	37440 ± 190	45770 ± 440	48340 ± 350	51590 ± 820	52900 ± 440
$[180, 225]$	38780 ± 200	44850 ± 870	47350 ± 400	52000 ± 1100	50000 ± 860
$[225, 270]$	36290 ± 190	47470 ± 730	47000 ± 1300	38320 ± 580	39300 ± 410
$[270, 315]$	35330 ± 190	45300 ± 780	44010 ± 430	32430 ± 370	32800 ± 290
$[315, 360]$	36070 ± 190	45690 ± 840	46400 ± 1700	50400 ± 1700	46000 ± 710

corresponding results and plots are shown in Table 1.22 and Figure figure run. The errors are statistical only.

The constrained kinematics of annihilation events is such that, candidate events can be identified also through a search for a single photon with energy and polar angle related to each other as expected for a photon produced in the process $e^+e^- \to \gamma\gamma$. Of course, one should count photons either in the inner ring of the FR or in the outer ring, in order to avoid a double counting of events. Therefore, two single photon selections have been designed to search for annihilation events. They are defined by the requirements summarised in Table 1.23. These selections are strongly contaminated by background. This can be subtracted statistically from a fit of the signal region and of the sidebands of the distributions of the following variables: $\Delta E = E_\gamma - f(\theta_g)$, with $f(\theta)$ given by $E = exp(c + s\theta)$ where $c = 6.4$ and $s = -20.6$ (true for $E_{beam} = 430$ MeV) and, alternatively, $M^2_{miss} = 2m_e[E_{beam} - E_\gamma(1 + \frac{E_{beam}}{2m_e}\theta^2_\gamma)]$ the squared missing mass. Both quantities are zero for a photon produced in a two photons annihilation

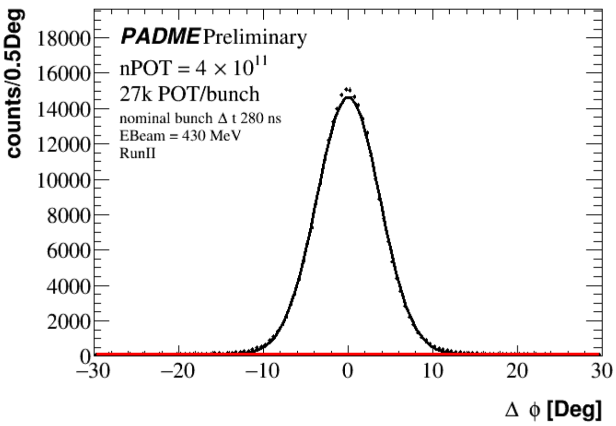

Figure 1.38: *$\Delta\phi$ distribution for all the statistic superimposed to the background (second order polynomial function) + signal (gaussian function).*

Table 1.22: *Yield as a function of the run number and of the selection*

ϕ [Deg]	$N_{POT/10^{10}}$	$N_{\Delta\phi}$	$N_{\Delta E_{In}}$	$N_{\Delta E_{Out}}$
30369	8.2	54570 ± 230	74900 ± 1100	71100 ± 1700
30386	2.8	21440 ± 150	27900 ± 1000	26000 ± 440
30547	7.1	51470 ± 230	67100 ± 1800	66500 ± 930
30553	2.8	19040 ± 140	26340 ± 880	25100 ± 2000
30563	6.0	42200 ± 210	56500 ± 1400	55500 ± 3500
30617	6.1	43320 ± 210	58000 ± 1800	56700 ± 4400
30624	6.6	45700 ± 210	63700 ± 1400	61300 ± 3000
All	39.7	276700 ± 530	375600 ± 3000	365700 ± 4300

Table 1.23: *Single photon selection.*

	$\lvert\Delta E\rvert = \lvert E_\gamma - f(\theta_g)\rvert < 100$ MeV
γ inner ring	$_{min} < R_\gamma < R_{mid}$
γ outer ring	$R_{mid} \leq R_\gamma < R_{max}$

event. The background, instead, is smooth under the peak at zero, but it exhibits a different shape for the two variables. Figure 1.39 shows the distribution of ΔE and M^2_{miss} for the inner and outer ring of a specific slide; from the plot one can appreciate how the background shape differs not only from bin to bin of the same variable, but also when moving from one variable to the other. Therefore, even if the events used in the fit are exactly the same the systematic uncertainty coming from the background modelling may be different. The annihilation yield obtained from both single photon searches, looking at the inner or outer ring of ECAL, and from both the ΔE and M^2_{miss} distributions are reported in Table 1.21, along with the results

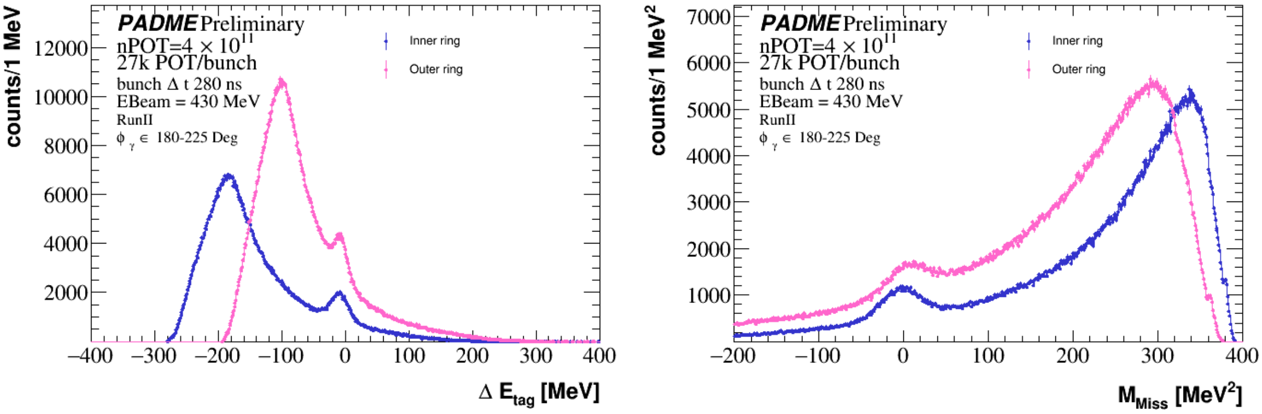

(a) **(b)**

Figure 1.39: *Comparison between the (a) ΔE_{tag} and (b) M^2_{miss} in inner (blue dots) and outer (pink dots) ring belonging. The variables are extracted from photons with* $R \in]115.8, 172.82[$ mm *and* $\phi \in [180, 225[$ Deg.

obtained from the two-photon selection described earlier in this section.

The subtraction of the background is performed with a new procedure trying to account for beam induced background and also for background from pileup. The distributions of ΔE and M^2_{miss} have been fit with a linear combination, with free coefficients, of a template for the signal component, a template for the beam background and a template for the pileup. The beam background is obtained by applying the same single photon selection to the no-target PADME data set, while the template of the pileup is obtained from the simulated sample of annihilation events embedded in the pileup of interactions from 25000 positrons per bunch. In this kind of simulation the single photon selection clearly select a signal component in addition to the background component. In order to obtain a signal free distribution, the signal region (i.e. the interval [-70,100] MeV) is removed and the sidebands are simultaneously fit with a smooth function in the range $[-100 \text{ MeV}, 250 \text{ MeV}]$ for ΔE and $[-200 \text{ MeV}, 300 \text{ MeV}]$ for M^2_{miss}.

This is shown if Figure **??**, where the red line, representing the function fitting and connecting the sidebands is used as template of the background from pileup.

The fit is done with the Roofit cite toolkit. The signal is described as the sum of two gaussian contributions G_{lr}, G_{hr}; this allows to account for a component of the signal reconstructed with an error larger than the core resolution. In summary, the model fit to the data has the free parameters listed in Table 1.24. The best fit is achieved by minimizing the negative loglikelihood. Examples of the fit results, with all the components of signal and background determined by the minimization are shown in Figure 1.41 for ΔE distributions and in Figure 1.42 for M^2_{miss} for the squared missing mass.

The number of signal events is estimated as follows: $N_{sig} = f_s N$, where f_s is the fraction of the signal component in the best fit combination of the templates and N is the total number of

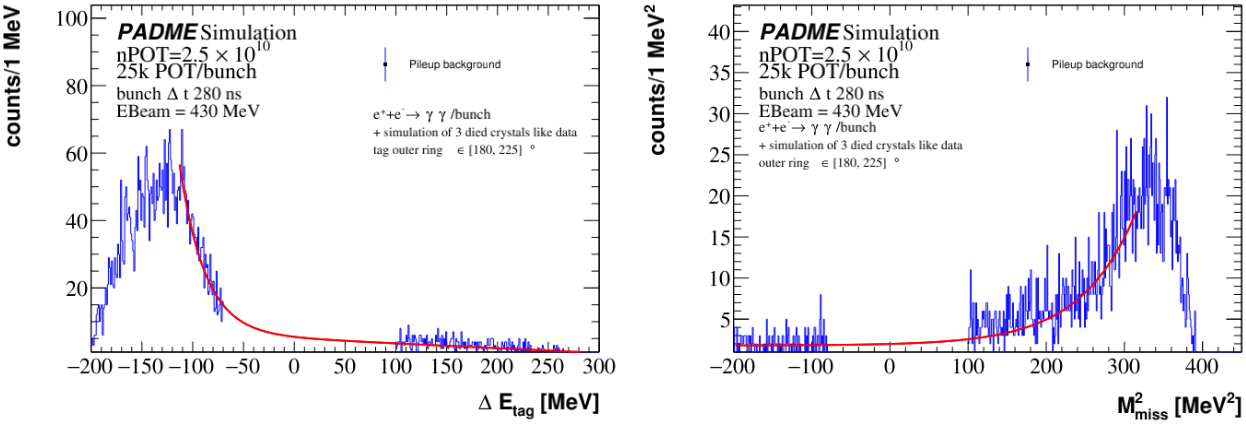

(a) (b)

Figure 1.40: *Distribution of pileup background in the tag (a) and squared missing mass (b) distribution extracted using MC simulation of one annihilation events generated by CalcHEP embedded in* 25000 *POT and predict the signal region fitting with an exponential and polynomial of one order degree functions.*

Table 1.24: *Single photon fit parameters.*

Description	parameter
Signal fraction	f_s
Mean of the first gaussian	μ_1
Sigma of the first gaussian	σ_1
Mean of the second gaussian	μ_2
Sigma of the second gaussian	σ_2
Fraction of the second gaussian integral over the total signal	f_g
Fraction of the pileup integral over the total background	f_p

candidates. The statistical errors quoted in Table 1.21 are estimated by propagating the error on the counting of the candidates and the error of f_s from the fit.

1.9.5 Annihilation photon efficiency in data

The tag and probe technique has been applied as described in Section 1.6.1 to the data preselected, clean-up and corrected for beam-ECAL offsets. The measurement is performed in the overall data sample, and also separately in the 16 bins of ECAL. Tags are selected with the single photon selection described in Table 1.23. Then, for each tag with an energy higher than 90 MeV a search for a cluster matching the probe on the other side is performed using the following criteria:

- $|\Delta t| = |t_{tag} - t_{probe}| < 7$ ns;

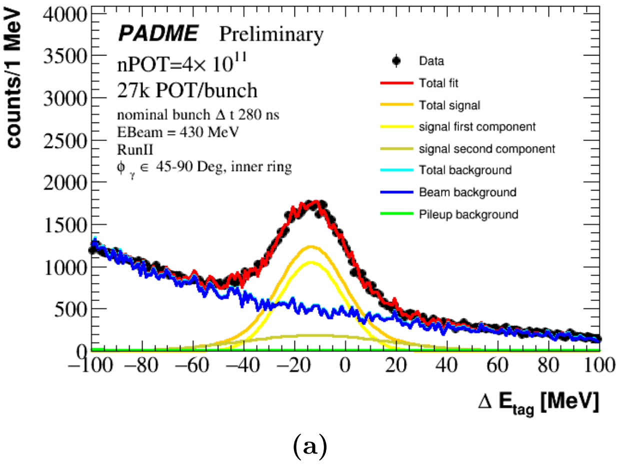

Figure 1.41: *Fit of the* ΔE_{Tag} *distribution for photon belonging (a)* $R \in]115.8, 172.82[$ mm *and* $\phi \in [180, 225[$ Deg*, (b)* $R \in [172.82, 258[$ mm *and* $\phi \in [45, 90[$ Deg*. The data (black dots) is fitted with a total function (red line) given by the sum of a total signal component in orange (composed by two gaussian function in yellow) and a total background component in cyan (given by the sum of pileup effect in green and the beam related background in blue).*

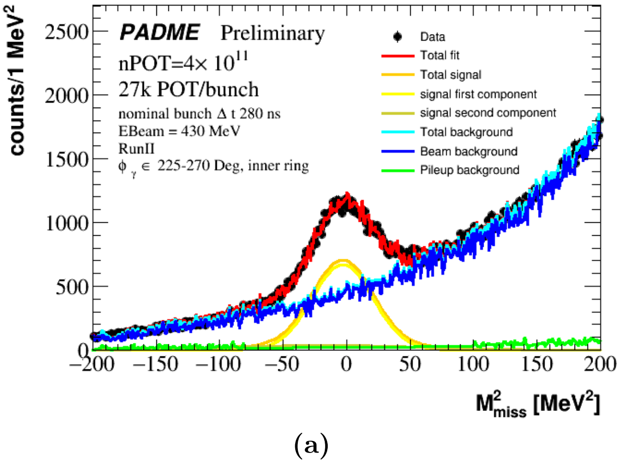

Figure 1.42: *Fit of the missing mass squared distribution for photon belonging the inner (a) and outer (b) in* $\phi \in [225, 270[$ Deg*. The data (black dots) is fitted with a total function (red line) given by the sum of a total signal component in orange (composed by two gaussian function in yellow) and a total background component in cyan (given by the sum of pileup effect in green and the beam related background in blue.*

- $E_{probe} > 90$ MeV
- $|\Delta\phi| < 25°$;

- $|\Delta E_{probe}| < 100$ MeV;
- $|\Delta E_{TP}| = |E_{probe} - E_{beam} + f(\theta_{tag})| < 100$ MeV;

Table 1.25: *Number of tag yield N_{Tag} and its error ΔN_{Tag}, number of probe N_{Probe} with the error ΔN_{Probe} and the efficiency ϵ measured form the ratio of the probe over the tag yield with the error $\Delta\epsilon$ obtained applying the propagation of the tag and probe errors. The yields are obtained with events that pass the multiplicity selection and photons that pass the cluster quality cuts.*

ϕ [Deg]	N_{Tag}	N_{Probe}	ϵ
		Inner ring	
$[0, 45]$	52000 ± 1100	37460 ± 190	0.721 ± 0.015
$[45, 90]$	38310 ± 580	28420 ± 170	0.742 ± 0.012
$[90, 135]$	32430 ± 370	26630 ± 160	0.821 ± 0.011
$[135, 180]$	50400 ± 1700	36390 ± 190	0.723 ± 0.024
$[180, 225]$	57000 ± 1300	38890 ± 200	0.682 ± 0.016
$[225, 270]$	45300 ± 470	35560 ± 190	0.785 ± 0.009
$[270, 315]$	46320 ± 800	33610 ± 180	0.726 ± 0.013
$[315, 360]$	51590 ± 820	35280 ± 190	0.684 ± 0.011
		Outer ring	
$[0, 45]$	44850 ± 870	37870 ± 200	0.844 ± 0.017
$[45, 90]$	47470 ± 730	35520 ± 190	0.748 ± 0.012
$[90, 135]$	45300 ± 780	33980 ± 180	0.75 ± 0.014
$[135, 180]$	45690 ± 840	35610 ± 190	0.779 ± 0.015
$[180, 225]$	46950 ± 760	38160 ± 200	0.813 ± 0.014
$[225, 270]$	46730 ± 520	29430 ± 170	0.63 ± 0.008
$[270, 315]$	53700 ± 1400	27660 ± 170	0.515 ± 0.014
$[315, 360]$	45770 ± 440	36690 ± 190	0.801 ± 0.009

The results are shown in Table 1.25 and Figure 1.43. The tag and probe distributions for all the statistic with them fits are reported in Figure 1.44. The individual fits are collected in Figure ref in appendix ref. These efficiencies represent the probability to detect, reconstruct and select an annihilation photon after all the clean-up and selection criteria, except for the FR, are applied. They are lower than the values anticipated in Section 1.8 due to the more stringent selection requirements; however the trend as a function of phi and R matches the naive expectations deriving from the knowledge of a few hardware problems affecting ECAL.

In Table 1.26 the annihilation yields are reported after the efficiency correction. In Figure 1.45 the schematic view of the relative annihilation yield is also shown before (a) and after the efficiency correction (b). As is shown, the annihilation yield distribution become more uniform after the efficiency correction.

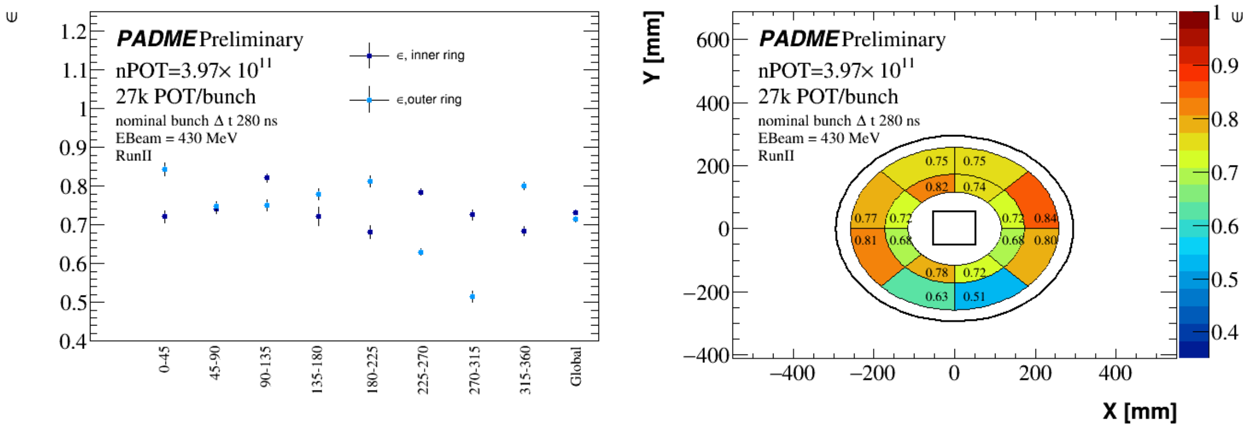

(a) (b)

Figure 1.43: *(a): Trend of the efficiency for bins in the inner ring in blue and outer once in light blue obtained requiring the multiplicity selection and cluster quality cuts; (b) schematic view of the measured efficiency.*

Table 1.26: *Annihilation yield after efficiency correction.*

ϕ [Deg]	$N^W_{\Delta\phi}$	$N^W_{\Delta E_{In}}$	$N^W_{MM^2_{In}}$	$N^W_{\Delta E_{Out}}$	$N^W_{MM^2_{Out}}$
$[0, 45]$	66200 ± 1800	65100 ± 1700	65100 ± 1800	67500 ± 2000	68200 ± 1600
$[45, 90]$	61300 ± 1400	63000 ± 1200	65700 ± 1200	60600 ± 1200	61600 ± 1300
$[90, 135]$	62700 ± 2000	65500 ± 1900	61000 ± 1400	61800 ± 1600	62400 ± 1300
$[135, 180]$	64700 ± 2300	63300 ± 2200	66900 ± 2300	66200 ± 1700	67900 ± 1400
$[180, 225]$	67300 ± 2100	65800 ± 2000	69400 ± 1700	63900 ± 1700	61500 ± 1500
$[225, 270]$	61800 ± 1300	60500 ± 1200	59900 ± 1700	60800 ± 1200	62500 ± 1000
$[270, 315]$	64800 ± 1700	62400 ± 1500	60600 ± 1200	63000 ± 1900	63600 ± 1800
$[315, 360]$	67700 ± 1700	66800 ± 1600	67900 ± 2800	62900 ± 2200	57500 ± 1100

1.10 Results

The annihilation yield obtained in Subsection 1.9.4 and the efficiency for annihilation photons measured in data, reported in Section 1.9.5 are combined to derive a cross section measurement for the annihilation of a 430 MeV positron with an atomic electron. Using the measurement of the number of signal events obtained from the two-photon selection, the average efficiency measured on the entire data set and the other parameters summarized in Table 1.27, the following results are obtained for the visible and total cross section:

$$\sigma(e^+e^- \to \gamma\gamma) = 1,973 \pm 0,030\ (\text{stat}) \pm 0,082\ (\text{syst}) \pm 0,098\ (\text{lumi})\ \text{mb}. \tag{1.21}$$

On all statistic the measurement was extracted also fitting the squared missing mass, see

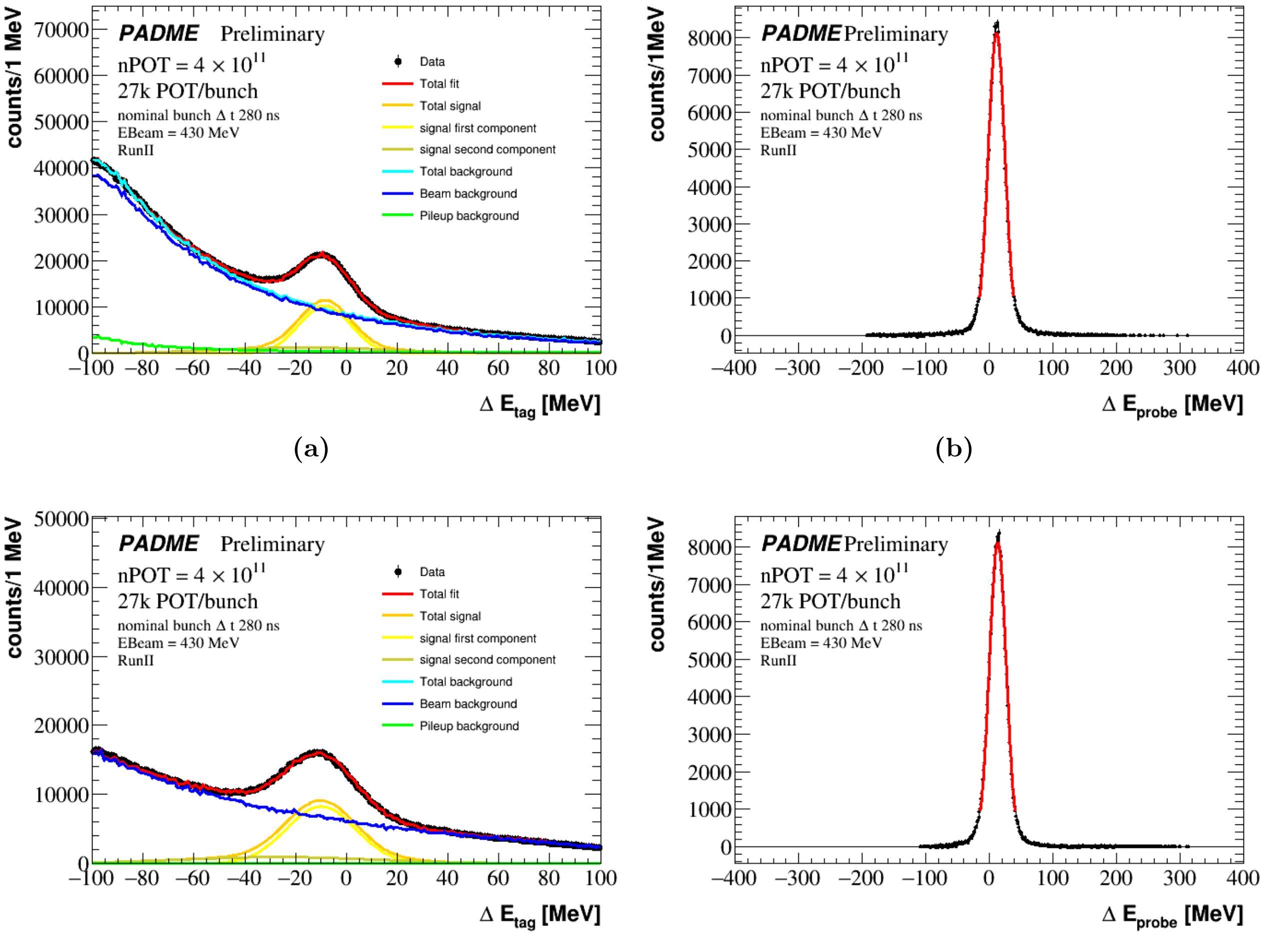

(a) (b)

(c) (d)

Figure 1.44: *Distribution of tag (a) and the matched probe used (b) for the inner ring efficiency measurement and for tag (c) and the matched probe used (d) for the outer ring efficiency measurement.*

Table 1.27: *Variable used to extract the annihilation in two photons cross section.*

Variable	Value
two-photon annihilation yield	276700 ± 530
inner ring efficiency	0.731 ± 0.009
outer ring efficiency	0.714 ± 0.006
acceptance	0.0653 ± 0.0003
N_{POT}	4×10^{11}
$N_{e/S}$	$0.0105b^{-1}$

Figure 1.46. In Table 1.28 the yields and cross sections obtained with all five methods are

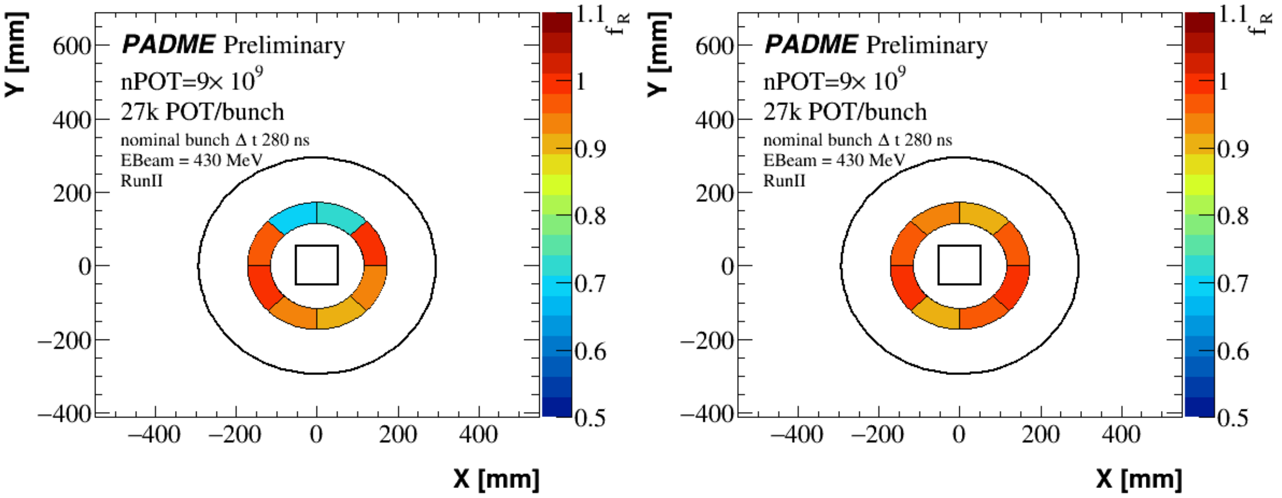

(a) (b)

Figure 1.45: *Schematic view of the yield of annihilation candidates in eight slices of ECAL. The number of candidates passing the pre-selection is normalised to the highest value observed. Each annihilation candidate is assigned to the slice where the most energetic photon in the pair lies. Before (a) and after (b) the efficiency correction.*

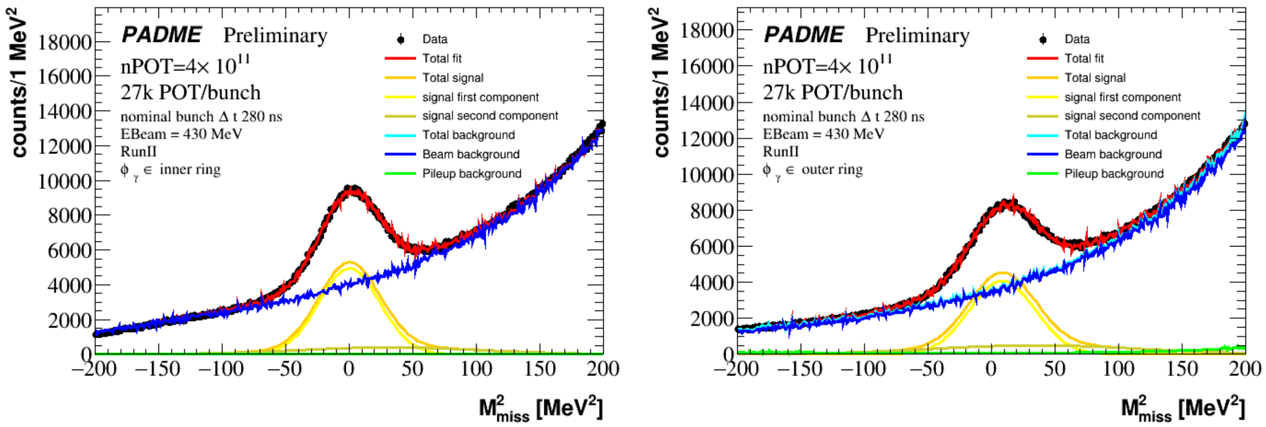

(a) (b)

Figure 1.46: *Squared missing mass distribution for inner (a) and outer (b) ring.*

reported.

The systematic errors on the measurement are related to the yield extraction and the efficiency determination; they will be discussed in Section add ref . The error coming from the uncertainty on the total number of positrons hitting the target is quoted separately. The same happens for the acceptance, that is used to extrapolate the visible cross section to the total cross section.

Table 1.28: *Annihilation in two photons cross section measured with the five methods on all statistic and using the global efficiency.*

Method	Yield	cross section [mb]
$\Delta\phi$	276700 ± 530	2.007 ± 0.031
ΔE_{in}	375600 ± 3000	1.946 ± 0.028
ΔE_{out}	365700 ± 4300	1.939 ± 0.028
$M^2_{miss,\ in}$	369400 ± 1100	1.913 ± 0.024
$M^2_{miss,\ out}$	365200 ± 8500	1.937 ± 0.048

1.10.1 Phi dependence

In Table 1.29 the cross section measurement derived with the two-photon selection and with the fit either of ΔE or M^2_{miss} are collected. They appear fully consistent with the measurement in Equation 1.21.

Table 1.29: *Cross sections measured with the yields of one (Tag and missing mass squared in the inner ring and Tag and missing mass squared in the outer ring) and two photons as a function of them azimuthal angles. The cross sections are obtained with events that pass the multiplicity selection and photons that pass the cluster quality cuts.*

ϕ [Deg]	$\sigma_{\Delta\phi}$ [mb]	$\sigma_{\Delta E_{In}}$ [mb]	$\sigma_{MM^2_{In}}$ [mb]	$\sigma_{\Delta E_{Out}}$ [mb]	$\sigma_{MM^2_{Out}}$ [mb]
$[0, 45]$	2.005 ± 0.056	1.972 ± 0.052	1.971 ± 0.056	2.045 ± 0.062	2.067 ± 0.048
$[45, 90]$	1.856 ± 0.041	1.908 ± 0.037	1.989 ± 0.035	1.834 ± 0.035	1.865 ± 0.037
$[90, 135]$	1.899 ± 0.06	1.983 ± 0.059	1.846 ± 0.042	1.871 ± 0.048	1.889 ± 0.039
$[135, 180]$	1.959 ± 0.068	1.918 ± 0.066	2.025 ± 0.069	2.006 ± 0.05	2.056 ± 0.043
$[180, 225]$	2.039 ± 0.065	1.992 ± 0.061	2.103 ± 0.052	1.936 ± 0.052	1.862 ± 0.045
$[225, 270]$	1.873 ± 0.04	1.832 ± 0.035	1.814 ± 0.053	1.842 ± 0.036	1.892 ± 0.031
$[270, 315]$	1.964 ± 0.052	1.89 ± 0.047	1.836 ± 0.038	1.907 ± 0.056	1.927 ± 0.055
$[315, 360]$	2.05 ± 0.051	2.023 ± 0.049	2.056 ± 0.084	1.904 ± 0.066	1.741 ± 0.033

Figure 1.47 and Table 1.29show the cross section measured in the 8 independent slices of ECAL, with the five methods and compared with the theory prediction from Babayaga. Despite the differences in performance of the various slices, the most relevant caused by local inefficiencies, the cross section measurement appear pretty stable and in agreement with the SM prediction within the measurement errors.

1.10.2 Run dependence

To study the stability of the result as a function of the pileup, beam background and time structure of the beam bunch, the cross section was measured separately in each run: for each

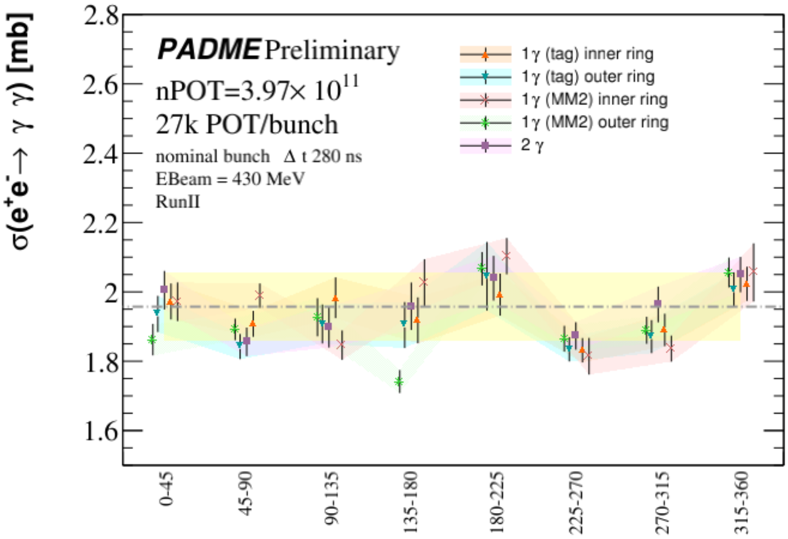

Figure 1.47: *Trend of the cross section as a function of the phi slice (the annihilation photon belong to a phi bin if the respective most energetic photon belong to that bin). The yellow strip represent the uncertainty of* 5% *on the multiplicity measurement. The orange dots are the cross section measurement done with a single photon obtained from tag yields in the inner ring, the azure one is the cross section trend obtained from the single photon form tags in the outer rings, the pink dots correspond to the cross section obtained from the missing mass squared of photons in the inner ring, the green are from photons measured from missing mass squared spectrum for clusters in outer ring and the violet are the cross sections obtained with the two photons (selection: most energetic photon in FR and time coincidence of* 10 ns*).*

sub- sample was extracted the average efficiency in the inner ring, the average efficiency in the outer ring and the yield of signal annihilation events were measured. The results on the efficiency measurements are reported in Table 1.30 and in Figure 1.48. The annihilation yield corrected for the efficiency are reported in Table 1.31.

The yield of annihilation events is obtained both with the usual two-photon selection, fitting the $\Delta\phi$ distribution, and with the single photon selection fitting the ΔE distribution. The results are summarised in Table 1.32 and represented in Figure 1.49.

1.10.3 Systematics

The cross section measurement is strongly dependent on the data-driven efficiency measurement. The latter exhibits a non trivial dependence on the sector of ECAL that can be ascribed to local defects but also to the uneven distribution of background in the detector. The systematic uncertainty deriving from an imperfect accounting of these effects can be assessed looking at the differences in the annihilation yield corrected for the efficiency obtained in the different slices and summarised in Table 1.29. Each sector is independent from the others and the statistics of events in each slice is approximately the same, therefore one can look at how the

Table 1.30: *Number of tag yield N_{Tag} and its error ΔN_{Tag}, number of probe N_{Probe} with the error ΔN_{Probe} and the efficiency ϵ measured form the ratio of the probe over the tag yield with the error $\Delta\epsilon$ obtained applying the propagation of the tag and probe errors. as a function of the run. The yields are obtained with events that pass the multiplicity selection and photons that pass the cluster quality cuts.*

Run number	N_{Tag}	N_{Probe}	ϵ
Inner ring			
30369	71100 ± 1700	52340 ± 230	0.736 ± 0.018
30386	26010 ± 440	20540 ± 140	0.790 ± 0.014
30547	66490 ± 930	49150 ± 220	0.739 ± 0.011
30553	25100 ± 2000	18110 ± 140	0.720 ± 0.057
30563	55500 ± 3500	40370 ± 200	0.728 ± 0.046
30617	56700 ± 4400	41910 ± 210	0.740 ± 0.058
30624	61300 ± 3000	44040 ± 210	0.719 ± 0.035
All runs	365700 ± 4300	267370 ± 520	0.731 ± 0.009
Outer ring			
30369	74900 ± 1100	52680 ± 230	0.703 ± 0.011
30386	27900 ± 1000	20630 ± 140	0.741 ± 0.028
30547	67100 ± 1800	49480 ± 220	0.737 ± 0.02
30553	26340 ± 880	18170 ± 140	0.690 ± 0.024
30563	56500 ± 1400	40590 ± 200	0.718 ± 0.018
30617	58000 ± 1800	41800 ± 200	0.721 ± 0.023
30624	63700 ± 1400	44360 ± 210	0.696 ± 0.016
All runs	375620 ± 3000	268100 ± 520	0.714 ± 0.006

Table 1.31: *Annihilation yield corrected for efficiency.*

ϕ [Deg]	$N_{POT/10^{10}}$	$N^{W}_{\Delta\phi}$	$N^{W}_{\Delta E_{In}}$	$N^{W}_{\Delta E_{Out}}$
30369	8.2	105500 ± 3100	101800 ± 2900	101200 ± 2900
30386	2.8	36700 ± 1500	35300 ± 1500	35100 ± 1500
30547	7.1	94400 ± 3000	90800 ± 2800	90200 ± 2800
30553	2.8	38300 ± 3300	36600 ± 3100	36400 ± 3100
30563	6.0	80700 ± 5600	77600 ± 5200	77200 ± 5200
30617	6.1	81100 ± 6800	78300 ± 6600	78600 ± 6600
30624	6.6	91400 ± 5000	88600 ± 4700	88000 ± 4800
All	39.7	530100 ± 8200	513800 ± 7500	512100 ± 7300

eight measurements deviates from their average and establish whether there is any fluctuation in excess of the expected statistical contribution. Indeed, the estimates of the cross sections from the two-photon selections fluctuate more than the statistical error on the average, leading to the indication of a systematic error on the efficiency $\sigma(\text{sys}_{\text{defects}}) = 0.021$ mb.

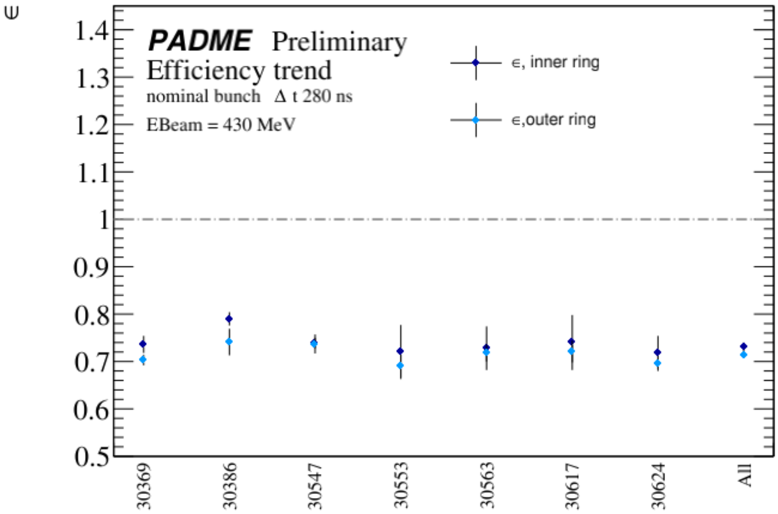

Figure 1.48: *Trend of the efficiency for inner ring in blue and outer one in light blue obtained requiring the multiplicity selection and cluster quality cuts extracted for each run. The last point represent the global efficiency of the whole data taking*

Table 1.32: *Cross sections measured with the yields of one (Tag in the inner ring and Tag in the outer ring) and two photons as a function of run number. The cross sections are obtained with events that pass the multiplicity selection and cluster quality cuts.*

Run number	$\sigma_{\Delta\phi}$ [mb]	$\sigma_{\Delta E_{In}}$ [mb]	$\sigma_{\Delta E_{Out}}$ [mb]
30369	1.941 ± 0.057	1.872 ± 0.053	1.861 ± 0.053
30386	1.98 ± 0.082	1.904 ± 0.079	1.896 ± 0.078
30547	1.988 ± 0.063	1.911 ± 0.06	1.899 ± 0.058
30553	2.051 ± 0.178	1.959 ± 0.168	1.95 ± 0.167
30563	2.012 ± 0.139	1.936 ± 0.131	1.926 ± 0.131
30617	1.989 ± 0.168	1.92 ± 0.162	1.927 ± 0.162
30624	2.07 ± 0.112	2.006 ± 0.107	1.993 ± 0.108
All runs	2.007 ± 0.031	1.946 ± 0.028	1.939 ± 0.028

The same consideration holds for the measurements derived analysis separately each run. As discussed in Section data the runs used for this measurement have an average number of positrons per bunch that varies from 19000 to 36000; in addition the time profile of the current in the bunch is not completely uniform. Since the amount of background impacts on the performance of the photon reconstruction and identification the assumption of an efficiency averaged over time may be incorrect. However, the fluctuations of the cross sections measured in each run are fully consistent with the statistical expectation, therefore no systematic error is assigned.

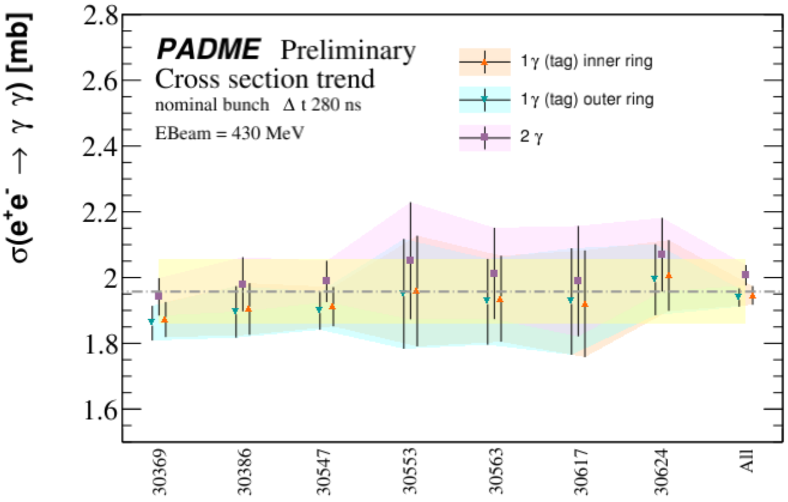

Figure 1.49: *Trend of the cross section as a function of the run. The yellow strip represent the uncertainty of* 5% *on the multiplicity measurement. The orange dots are the cross section measurement done with a single photon obtained from tag yields in the inner ring, the azure one is the cross section trend obtained from the single photon form tags in the outer rings, the violet are the cross sections obtained with the two photons (selection: most energetic photon in FR and time coincidence of* 10 ns*).*

The background modelling, though the choice of the interpolating template, is another source of systematic uncertainty. It can be assessed comparing the results from the fit of the $\Delta\phi$ distribution, in the two-photon selection, with the result of the ΔE and M^2_{miss} distributions in the single photon selection applied to the inner ring of ECAL. The resulting systematic error is $\sigma(\text{sys}_{\text{bkgmod}_\text{var}}) = 0.022$ mb.

In addition, the difference between the cross section measured in the single photon selection applied in the inner and outer rings must be considered. The two measurements are based on consistent, but experimentally different definition of the fiducial region, the first using the range $[R_{min}, R_{mid}]$ for the photon identified, the second using the range $[R_{mid}, R_{max}]$. Therefore, the systematic uncertainty related to the definition of the acceptance can be estimated as $\sigma(\text{sys}_{\text{acc}_\text{var}}) = 0.0079$ mb. On the other hand the acceptance is also affected by a theoretical error due to the missing NNLO contributions in Babayaga and to the uncertainty coming from the procedure matching the theory prediction at generator level to the experimental reconstruction and selection requirements. These errors are estimated to be $\sigma(\text{sys}_{\text{acc}_\text{th}}) = 0.0000$ mb.

A separate source of error comes from the estimate of the number of positrons collected on target. A careful calibration of the diamond target response relative to the BGO calorimeter of the BTF and a study of the stability of the measurement of over the data set used for this analysis number lead to an estimate of the relative error on N_{POT} equal to 4%. Table 1.33 summarizes all the sources of systematic errors combined in the measurement in Equation 1.22:

$$\sigma(e^+e^- \to \gamma\gamma) = 2.007 \pm 0.031\ (\text{stat}) \pm 0.033\ (\text{syst}) \pm 0.079\ (\text{lumi})\ \text{mb} \tag{1.22}$$

that is compatible with the measurement of Babayaga at NLO $\sigma = 1.9573 \pm 0.0051$ mb (for reference Babayaga estimation at LO is $\sigma = 1.9110 \pm 0.0004$ mb).

Table 1.33: *Measurement results.*

$\sigma(e^+e^- \to \gamma\gamma)$	2.007 ± 0.031 mb
Detector defects	0.021 mb
Background modelling	0.022 mb
Acceptance variation	0.0079 mb
Luminosity	0.079 mb

2

Dark photon search

The main role of the ECAL calorimeter is the detection of the ordinary photon produced in association with the dark photon A'. As described in Chapter 2, the technique used by PADME is the missing mass distribution $M^2_{A'} = M^2_{miss} = (p_{e^+} + p_{e^-} - p_\gamma)^2$ where, in addition to a good knowledge of the beam energy, is needed a good knowledge of the energy and angle of the photon.

By selecting events within a small interval around M^2_{miss}, the peak value corresponding to the signal, we approximate the search to a single counter experiment. The expected number of background events is large, therefore the Gaussian statistic can be used. Hence, the probability that, in absence of a signal, the number of background events exceeds the expected value by an amount Δ, such that $\Delta/\sqrt{N_{bkg}} > 0.47$, is less than 32% we can assert that the parameter values of new model that produce a number of events $\Delta > 0.47\sqrt{N_{bkg}}$ are excluded at the 68% confidence level.

The number of signal events can be expressed as a function of the new model parameter:

$$N_{sig} = \epsilon^2 \delta \sigma(e^+e^- \to \gamma\gamma) N_{POT} \epsilon_{sig} N_{e/S} \tag{2.1}$$

where

- ϵ is the mixing coefficient term;
- δ (see Table ref) is the kinematic factor calculated as the ratio of the signal cross section to the SM cross section of the annihilation in two photons $\sigma(e^+e^- \to \gamma\gamma)$;
- $\sigma(e^+e^- \to \gamma\gamma) = 1,91$ mb for a beam energy of 430 MeV at LO;
- N_{POT} is the number of positron on target;
- ϵ_{sig} is the efficiency of the A' signal, which can be decomposed in different terms: cut efficiency, acceptance, photon efficiency and efficiency of the veto cuts

$$\epsilon_{sig} = \epsilon^{sel}_\gamma \times A \times \epsilon_\gamma \times \epsilon^{veto}_{sig}; \tag{2.2}$$

- and $N_{e/S} = 0.0105$ b^{-1} is the number of electron on the target surface.

The ϵ value that satisfied the following relation can be considered excluded at 68% of Confidence Level:

$$\epsilon^2 > 0.47\sqrt{N_{Bkg}}/(\delta\sigma(e^+e^- \to \gamma\gamma)N_{POT}\epsilon_{sig}N_{e/S}). \tag{2.3}$$

2.0.1 Data sample, simulation, reconstruction and pre-selection

The data used for the dark photon analysis is composed by the seven runs analysed for the annihilation cross section measurement, a description of them is reported in Section reference.

Simulation of the new physics process is needed to extract the efficiency and acceptance of the signal selection cuts. The generation of the dark photon in association with a photon is done with the external generator CalcHEP. The dark and standard photons are generated in the Diamond target where a positron of the beam is also stopped and removed. For the determination of the dark photon exclusion limits as a function of the A' mass, MC samples of 10^6 events were simulated with different dark photon mass hypothesis in the range $[2.5\text{ MeV}, 17.5\text{ MeV}]$ with a step of 2.5 MeV. Since the beam background not well describe the data background, a pure $e^+e^- \to \gamma A'$ was simulated. In Table 2.1 the A' simulated masses are reported along with the luminosity.

Table 2.1: *Simulated $M_{A'}$, number of events generated and corresponding luminosity of the sample.*

$M_{A'}$ MeV	$N_{ev}/10^6$	$N_{POT}/10^{15}$ $(\epsilon = 10^{-3})$
2.5	1	3.07
5	1	3.07
7.5	1	2.80
10	1	2.57
12.5	1	2.03
15	1	1.54
17.5	1	1.05

For both, data and simulations, the photon reconstruction used is the multi hit, described in Section reference. Also the N_{POT} reconstruction is described in the same section.

The others detectors involved are PVeto and SAC, for which the hit identification is based on ROOT tools (TSpectrum add ref). The request done to identify the hit is the minimum amplitude, that is setted in case on PVeto hit to 20 mV and in case on SAC to 40 mV. The clusterisation algorithm used the to merge hits and built clusters is analogous to the one described for the ECAL detector, described in Section reference. A difference lie in the parameters used to clusterise:

- PVeto: an energy higher than 0.1 MeV is required for seed and hits. The hits can be merged to the seed if they are close in time within 4 ns and in space $\Delta Cell \leq 2$ with the seed;

- SAC: the cluster seed has an energy higher than 3 MeV and hits with energy hugher than 2 MeV can be merged to the seed if they are close in time within 1 ns and in space $\Delta Cell \leq 2$ with respect to the seed.

Also for this analysis event selection cuts were applied and ECAL clusters quality cuts. The cuts are described in Section add ref. In addition, the same cuts applied in the annihilation studies were applied to the ECAL photons: an energy higher than 90 MeV and to belong to the FR. A consequence of this pre-selection is a reduction of the A' mass range reach. In Figure 2.1 the squared missing mass M^2_{miss} is reported in azure for all clusters in ECAL, in orange the same variable for photon that pass the FR request and in red the photon that pass also the energy threshold cut. Since $M^2_{miss} \leq 300$ MeV, the maximum mass that can be probed is 15 MeV.

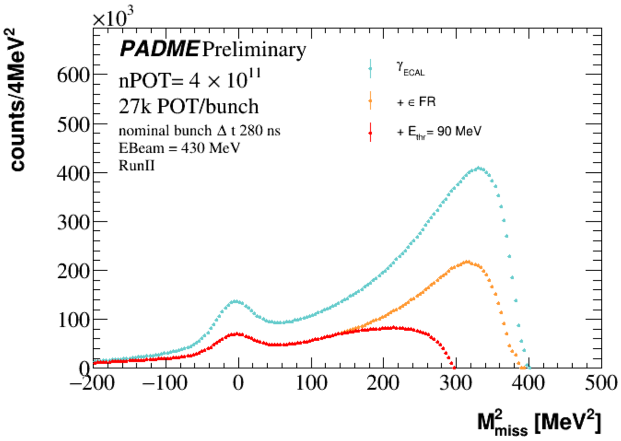

Figure 2.1: *Squared missing mass for all clusters recorded in ECAL in azure, for clusters that pass the FR request in orange and for those that pass also the energy threshold cut in red.*

2.0.2 Physical background rejection

The main sources of background, as described in Section ref, are the Bremsstrahlung, annihilation in two and three photons. In the following parameters the rejection strategy of them was described.

Annihilation in two photons

The two photons signature was deeply discussed in the previous sections. The rejection of this background was done requiring that no other photons exist in ECAL with energy higher than 90 MeV and in time coincidence of 4 ns (~ 3 times the ECAL time resolution observed in the two photons selection).

Bremsstrahlung

A photon revealed in ECAL could be from Bremsstrahlung if there is a positron in time coincidence revealed in PVeto. For this channel temporal and energetic cuts can be required between photon and positron.

The distribution of the difference in time of the two particles is shows in Figure 2.2. Since

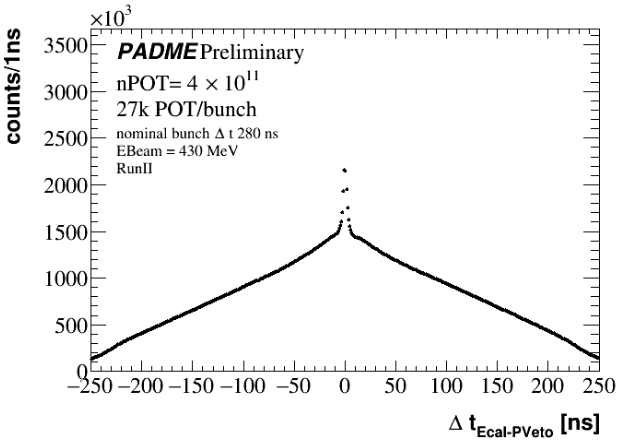

Figure 2.2: *Difference in time between the ECAL clusters and PVeto clusters for cluster energy higher than* 90 MeV*, inside the FR and passing the two photons annihilation veto.*

the peak that emerge over the triangular background, due to uncorrelated particles inside the bunch, has a width of 2.2 ns, the time coincidence cut was setted to $2 \times \sigma \sim 5$ ns. The correlation of the Bremsstrahlung process is shown in Figure 2.3, where is plotted the scatter plot between the energy of the photon, for energy higher than 90 MeV, and the positron position along the PVeto for a time coincidence of 5 ns. It is possible to notice how the clear Bremsstrahlung signature is overlapping with a relevant beam background. The energy

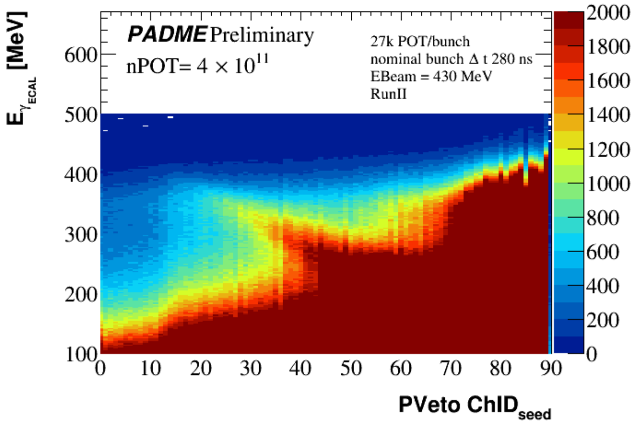

Figure 2.3: *Scatter plot between the energy of ECAL photons with energy higher than* 90 MeV *and the positron channel ID cluster seed in PVEto satisfying the time coincidence request.*

consistency cut is applied calculating the sum of the photon energy and the positron energy subtracted by the beam energy $\Delta E = E_{\gamma}^{ECAL} + E_{e^+}^{PVeto} + -E_{beam}$. The positron energy is

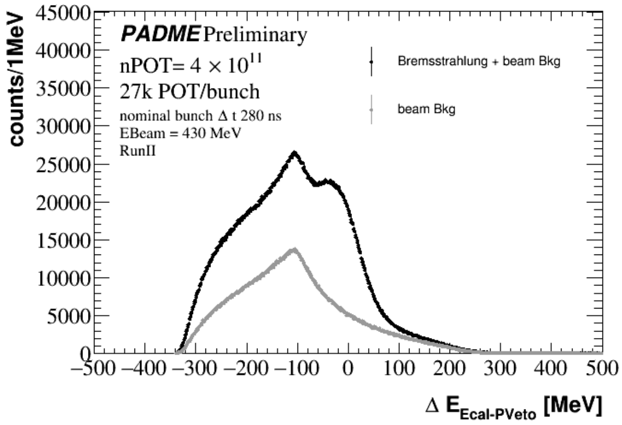

Figure 2.4: *The sum of photon and positron energies with the beam energy subtracted for events that pass the time coincidence of* 5 ns*, having the photon with energy higher than* 90 MeV *and with the positron cluster seed with channel ID in* [20, 70] *in black. In grey are reported the same distribution for beam background evaluated shifting in time inside the bunch the photons before the time coincidence cut.*

obtained from the calibration curve of the PVeto as explained in Section add ref. In Figure 2.4 is reported the ΔE distribution for events that pass the two photons annihilation photons veto, the Bremsstrahlung time coincidence request and for positrons with cluster seed in the range [20, 70] of PVeto channel ID, where the Bremsstrahlung correlation clearly emerge from the background. As Figure 2.3 shows there are two peaks, one at zero and another with lower ΔE. To verify that the Bremsstrahlung signal peak to zero in ΔE, the same plot was done decorrelating in time the two particles shifting the photon time of $t' = t + 100$ ns and subtracting the bunch length if the shifted time goes out the bunch window. Also now the time coincidence cut was applied $|t' - t_{e^+}| < 5$ ns. The ΔE of the uncorrelated photons and positrons was plotted in Figure 2.3 in grey. As it is shown, the ΔE peak at zero. For this reason the additional cut to remove Bremsstrahlung events is $|\Delta E| = |E_{\gamma} + ECAL_{e^+} - E_{beam}| < 50$ MeV.

The Bremsstrahlung yield with the ECAL photon inside the FR is shown in Figure 2.5. It is possible to notice how the Bremsstrahlung signature is basically overwhelmed by beam background.

$\gamma\gamma\gamma$ rejection

The last kind of physical background that should be rejected is the annihilation in three photons. If all the three photons fall in ECAL, this background is rejected by two annihilation cut removing the energy thresholds. Anyway, the most probable kinematic configuration of this process is one photon in ECAL and at least a photon in the SAC. To reject this background a

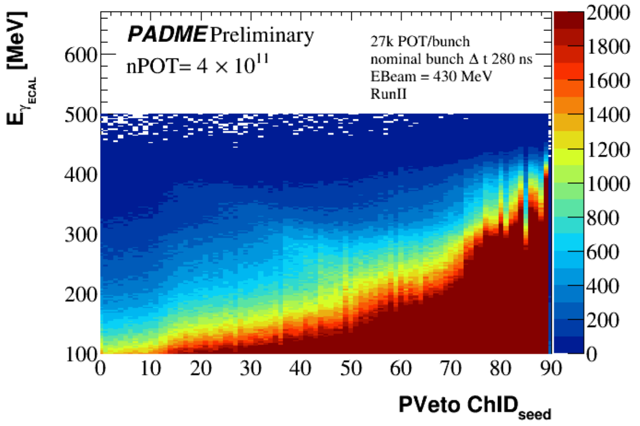

Figure 2.5: *Scatter plot between the energy of the ECAL photon with energy higher than* 90 MeV *and inside the ECAL FR and the positron channel ID cluster seed of the PVEto satisfying the time coincidence request.*

time coincidence is required between the ECAL photon and SAC photon. Since the SAC has an energy resolution of 50 MeV, a threshold of 50 MeV was set to the SAC photon.

To estimate the acceptance of this process was used Babayaga simulation of $e^+e^- \to \gamma\gamma(\gamma)$ (see Section add ref). The reconstructed events N' that satisfy the following requests: $E_\gamma > 90^{ECAL\ FR}$ MeV and $E_\gamma > 50^{SAC}$ MeV were counted. Then the total acceptance was calculated by the ratio of N' with the total number of events generated and it was equal to $0,2\%$.

To define the time coincidence window the difference in time between the photon recorded in ECAL and in SAC it is shown in Figure 2.6 (a). A peak with a sigma of $\sim$ 7 ns emerge on the triangular background distribution, than a time coincidence of $2\sigma \sim 14$ ns is chosen. However, the same difference in time for events that pass the $\gamma\gamma$ and Bremsstrahlung vetoes cut, the peak disappear, see Figure 2.6 (b). This effect is due to the frequent coincidence PVeto - SAC induced by positron Bremsstrahlung. In Figure 2.7 is reported the distribution of $\Delta t_{ECAL-PVeto}$ as a function of $\Delta t_{ECAL-SAC}$. As is clearly visible there is a horizontal correlation for $\Delta t_{ECAL-PVeto} \simeq 0$ ns that is due to the Bremsstrahlung in ECAL, a vertical correlation at $\Delta t_{ECAL-SAC} \simeq 0$ ns that is due to the annihilation in three photons and a strong diagonal correlation induced by the Bremsstrahlung in SAC. Consequently, the Bremsstrahlung veto in ECAL rejects most of the events that have $\Delta t_{ECAL-SAC} \simeq 0$ ns.

Since the Bremsstrahlung veto invalidates the ECAL - SAC correlation rejecting most of the events with $\Delta t_{ECAL-SAC} \simeq 0$ ns, this veto will not be considered.

2.0.3 A' kinematic cuts

Others considerations can be done studying the kinematics of the photon produced along with the dark photon. In particular, the photon energy range and the correlation between the energy and the photon radial position.

For each A' mass hypothesis the energy distribution of the associated photon in ECAL is

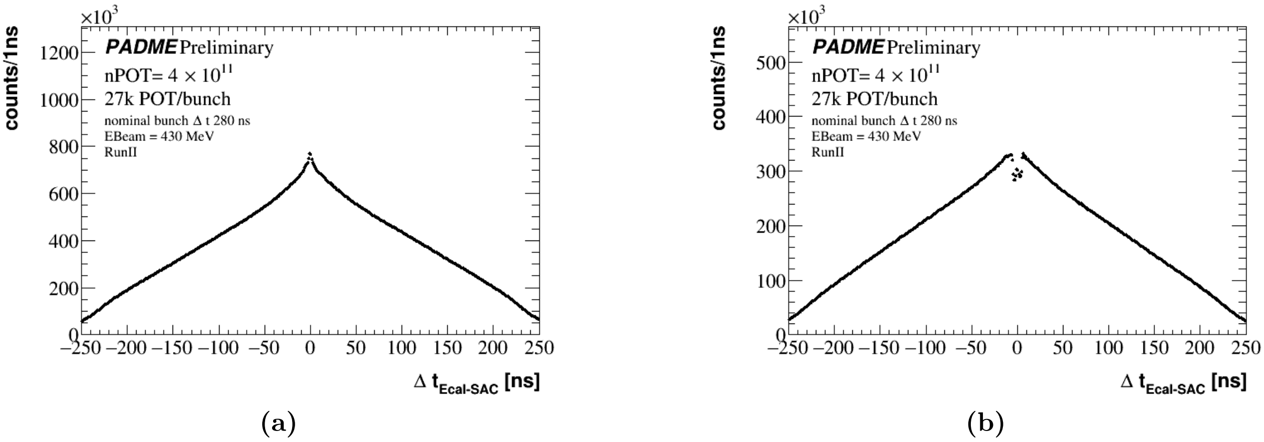

Figure 2.6: *Difference in time between photon in ECAL that pass the* $\gamma\gamma$ *veto (a) and the Bremsstrahlung veto (b) and a photon with energy higher than* 50 MeV *in SAC.*

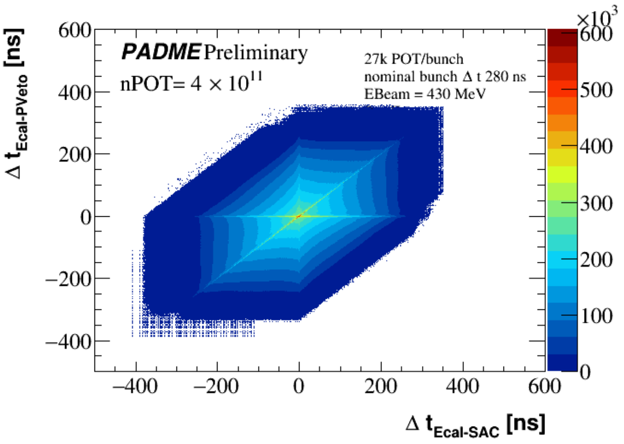

Figure 2.7: *Scatter plot of the difference in time between photons in ECAL and positrons in PVeto and the difference in time between photons in ECAL and photons in SAC.*

plotted in Figure 2.8 (a). As it is shown the photon has minimum and maximum of energies as a function of the A' mass. Thus an energy interval requirement can be considered as a function of the probed A' mass to reject background. Figure 2.8 (b) shows the correlation between the energy of the photon and its radial position for three A' mass hypotheses. From these distributions the function $E(R_\gamma, M_{A'})$ is extracted in order to consider the cut $|\Delta E| = |ECAL_\gamma - E(R_\gamma, M_{A'})| < 30$ MeV, where 30 MeV is about 3σ of the ΔE distribution evaluated from A' simulations. In Figure 2.9 the M^2_{miss} spectrum is shown for photons that pass the two photons annihilation veto, the energy range requirement for the mass hypothesis of 10 MeV and the energy-radial position correlation requirement for the mass hypothesis of 10 MeV. As it is clearly shown, these cuts don't reject background in the signal region, that for the mass hypothesis of 10 MeV is $M^2_{miss} \pm 2\sigma = 100 \pm 28$ MeV, thus they were not applied.

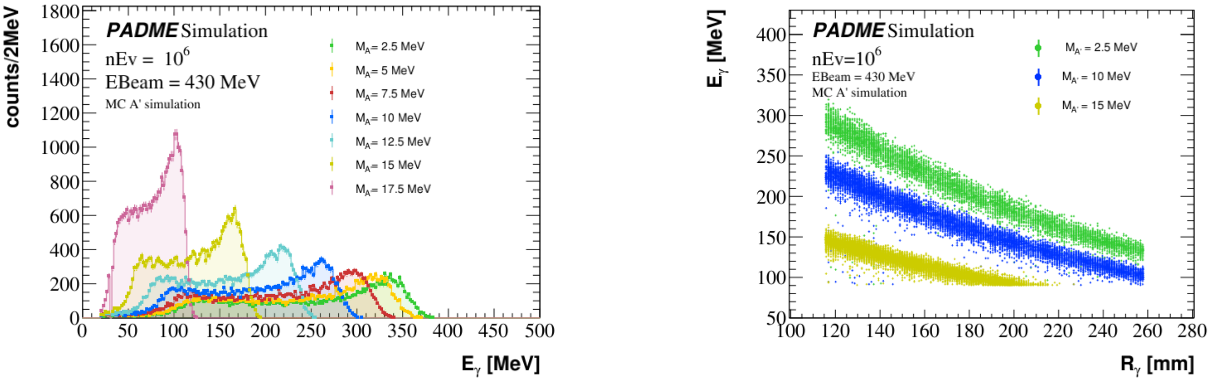

(a) **(b)**

Figure 2.8: *(a) Photon energy distribution for A' mass hypothesis from* $[2.5\ \text{MeV}, 17.5\ \text{MeV}]$. *(b) Correlation between the energy of the photon and its radial position for A' mass hypotheses $M_{A'} = 2.5$ MeV in green, $M_{A'} = 10$ MeV in blue and $M_{A'} = 15$ MeV in orange. The photons are required to pass the energy threshold of* 90 MeV *and to be inside the ECAL.*

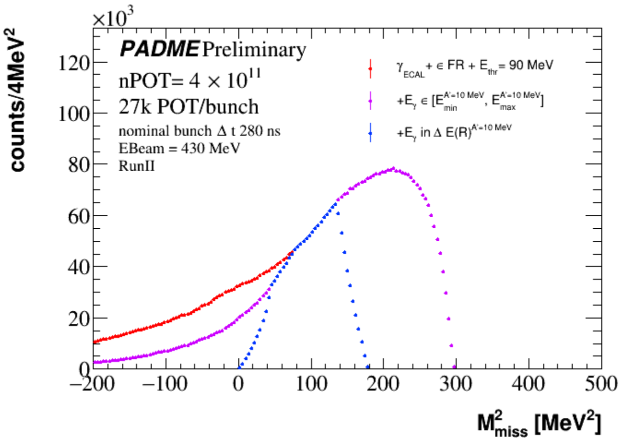

Figure 2.9: *Squared missing mass distribution for events that pass the $\gamma\gamma$ veto in red, the energy range requirement for $M_{A'} = 10$ MeV in pink and the correlation between the energy and the radius for the same mass hypothesis.*

2.0.4 Selection cut flow

The distributions of the data squared missing mass in data are shown in Figure 2.10 (a) adding sequentially the previous explained selection cuts from photons that have an energy higher than 90 MeV and inside the FR, after adding: the two photons veto, the Bremsstrahlung veto and finally the three photons annihilation veto.

As it is shown the rejection of Bremsstrahlung and three photons backgrounds reduce the candidate events more than the discussed expectation. This is because after the two photons annihilation cut the beam background contamination is dominant over the physical background.

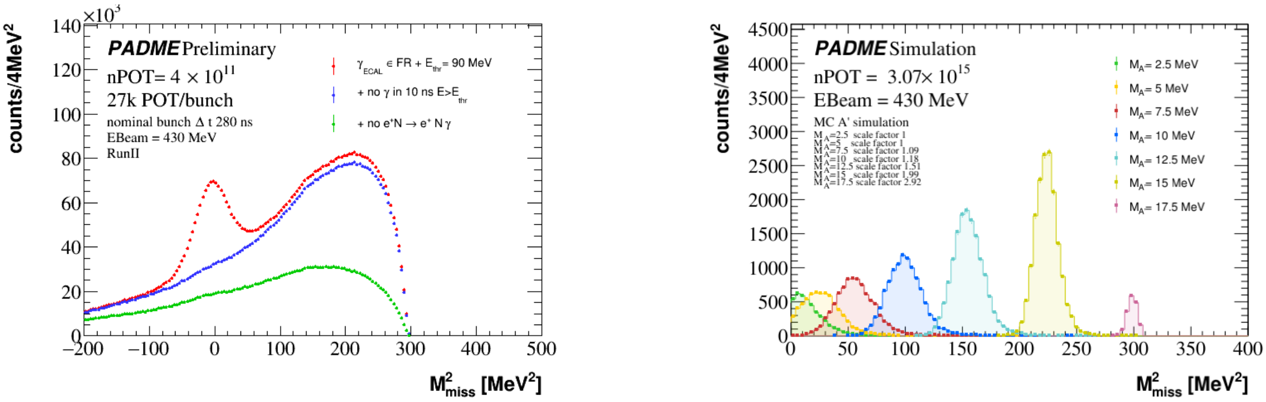

(a) (b)

Figure 2.10: *Squared missing mass of photons that pass the veto cuts for data (a) and for signal simulated at different A' masses without pileup (b).*

In Figure 2.10 (b) the M^2_{miss} distributions are shown for A' simulated without pileup for several mass hypotheses after the same selection as data.

In Table 2.2 the corresponding cut-flows for data and simulation ($M_{A'} = 10$ MeV) are reported.

Table 2.2: *Selection cut and number of photons passing the cuts for simulation ($M_{A'} = 10$ MeV) and data.*

Selection	N_γ	
	simulation $M_{A'} = 10$ MeV	data
N_{POT}	2.6×10^{15}	4×10^{11}
All photons	19631	2.4×10^{7}
Photons in FR	9245	1.2×10^{7}
$E_g > 90$ MeV	9213	6.4×10^{6}
no other photons with $E > 90$ MeV in 4 ns	9213	5.5×10^{6}
no e^+ in $\lvert\Delta t\rvert < 5$ ns and $\lvert\Delta E\rvert < 50$ MeV	9213	2.6×10^{6}

2.0.5 Background estimation

To estimate the background the number of photons falling in the signal region for each mass hypothesis were counted. The signal region is extracted from A' simulated samples with Gaussian fit to the squared missing mass distribution as a two sigma interval around the peak: $[M^2_{miss} - 2\sigma_{M^2_{miss}}, M^2_{miss} + 2\sigma_{M^2_{miss}}]$.

In the squared missing mass distribution of data, the signal events in the signal region are assumed to be negligible in order to extract the signal limits. The distribution was then fitted with a polynomial. From this fit the number of background in the signal region was counted. In Figure 2.11 is shown an example of the procedure for $M_{A'} = 10$ MeV.

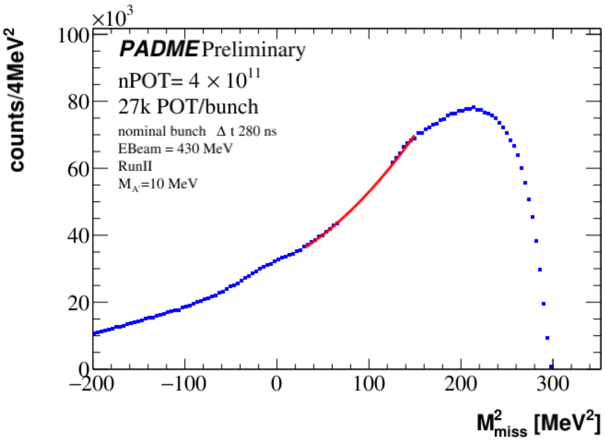

Figure 2.11: *Background estimation for a mass hypothesis of* $M_{A'} = 10$ MeV.

The procedure was applied to each mass hypothesis and for each veto cut. The distribution of the background yield is shown in Figure 2.12.

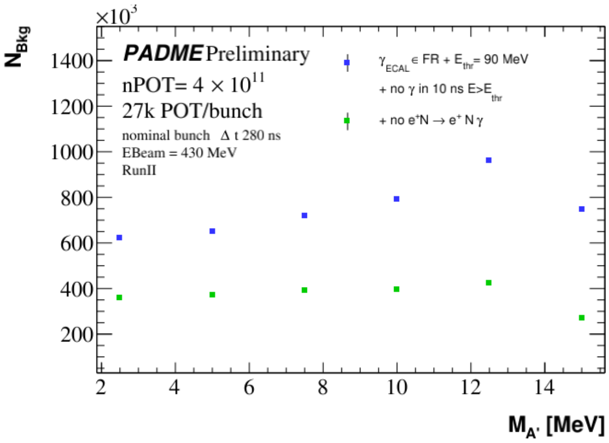

Figure 2.12: *Number of background photons passing the two photons annihilation veto in blue, the Bremsstrahlung veto in green and the three photons annihilation veto in yellow.*

2.0.6 A' efficiency and acceptance

To measure the A' efficiency and acceptance the factor $\epsilon_{\gamma}^{sel} \times A = \frac{N_{A'}^{after\ cut\ i}}{N_{A'}^{generated}}$ was extracted on dark photon simulated samples. $N_{A'}^{after\ cut\ i}$ corresponds to the number of photons that pass the cut selections and $N_{A'}^{generated}$ is the number of $e^+e^- \to \gamma A'$ generated. In Figure 2.13 the signal efficiency times acceptance is reported for each A' mass hypothesis and for each veto cut. As expected the variable under study doesn't change with the veto cut since the simulations don't contains pileup.

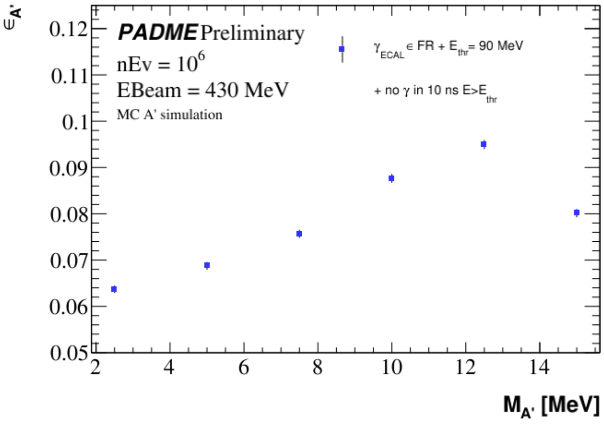

Figure 2.13: *Distribution of* $\epsilon_\gamma^{sel} \times A$ *as a function of the* A' *mass and as a function on the veto selection cuts.*

2.0.7 Signal veto efficiency

The background cuts, as discussed, reject more photons than expected from physical background because the beam background dominate over pileup interactions in target. For this reason there is a high probability to reject also signal photons and the limits should be corrected for a signal veto efficiency. To evaluate the fraction of photons not coming from the physics processes, the time of the photon candidate signal was shifted of 100 ns adding the bunch time duration if after the shift it is outside the bunch time window and then, only after the time shift, the veto cut was applied. This is equivalent to de-correlate in time the photon with respect to the other particle. Thus the signal veto efficiency cut was evaluated as:

$$\epsilon_{sig}^{veto} = 1 - \frac{N'}{N} \tag{2.4}$$

where N is the number of photons that pass the previous veto cut and N' is the number of photons that pass the veto despite its shifted time. For example, in case of the two photons annihilation veto, N represents the number of photons that are inside the FR with an energy higher than 90 MeV and N' corresponds to the number of photons with time $t' = t_\gamma + 100$ ns that has not photons with energy higher than 90 MeV in a time window of $t' \pm 4$ ns. In Figure 2.14 the difference $t_i - t_{\gamma_j}$ for $i \neq j$ and the difference $t'_i - t_{\gamma_j}$ are reported. As it is shown the veto cut, in case of shifted time, reject only de-correlated background events, mostly accidental beam background.

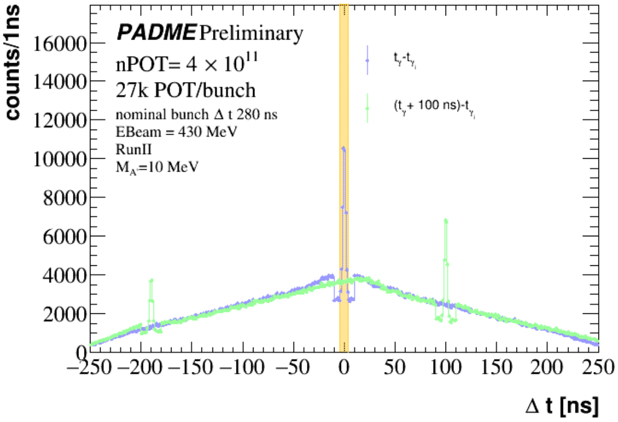

Figure 2.14: *Distribution of the time difference between two clusters in ECAL when the first photon passes the energy and radial FR requests in azure. In green the same distribution is shown when to the first photon is applied a* 100 ns *time shift.*

The same procedure was applied to measure the veto efficiency for all the Bremsstrahlung veto cut. In Figure 2.15 the obtained efficiencies are reported as a function of the A' mass hypothesis: for the annihilation veto and for the Bremsstrahlung veto. As expected the first efficiency is very close to one, while the Bremsstrahlung rejection implies a lower efficiency.

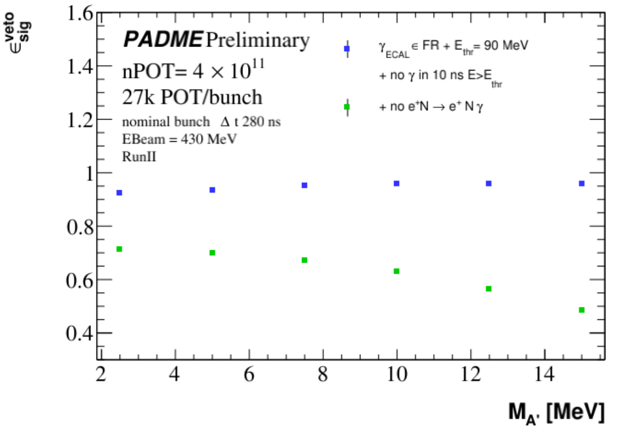

Figure 2.15: *Signal veto efficiency as a function of the A' mass hypothesis and for the three background rejection criteria: in blue the two photons veto, in green the Bremsstrahlung veto and in yellow the three photons veto.*

2.0.8 Results and prospectives

The limits at 68% of Confidence Level (C.L.) in the A' parameters space were extracted using Equation 2.3. In Figure 2.16 are reported the limits obtained for each veto selection cut: photons passing the $\gamma\gamma$ annihilation veto, photons passing the Bremsstrahlung veto and photons

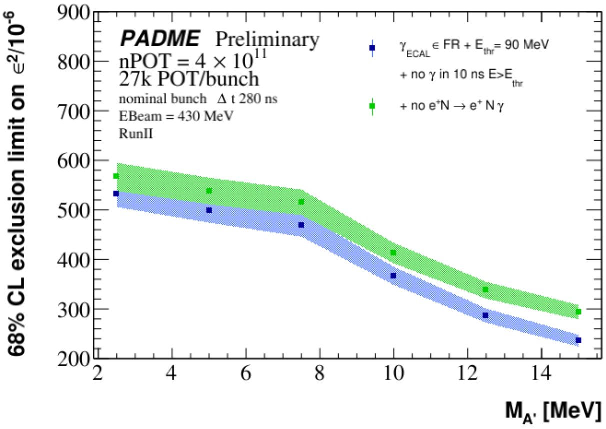

Figure 2.16: *Limits at* 68% *C.L. on* ϵ^2 *as a function of the* A' *hypothesis mass and as a function of the veto condition applied, obtained counting events in* 2σ *respect the peak position of* M^2_{miss}. *In blue for photons that pass the annihilation in two photons veto, in green applying the Bremsstrahlung veto and in yellow for the annihilation in three photons.*

passing the $\gamma\gamma\gamma$ annihilation veto. As it is shown, despite a huge background rejection in the Bremsstrahlung, the limits become worst. This is due to the low signal veto efficiencies which reduces the background of the same amount ϵ^{veto}_{sig} but the overall effect it the increasing of the limits like the inverse of the efficiency square root $\epsilon^2 \propto 1/\sqrt{\epsilon^{veto}_{sig}}$.

For this reason the preliminary limits war estimated done with events passing only the two photons annihilation veto. Assuming that all data collected in RunII have the same feature on the seven runs analysed in this dissertation, the limits can be extended at 5×10^{12} POT that corresponds to the whole RunII data taking luminosity. In Figure 2.17 are reported the limits for events that pass the two photons annihilation veto for the analysed data and the projection to the full RunII data set of $N_{POT} 5 \times 10^{12}$.

The limits extracted by the proposal studies with a luminosity of 4×10^{13} (see Figure put reference limits chapter 1), the limits evaluated in this work were worse of a factor ~ 20. This results is a consequence of the unexpected huge beam background observed in the experiment which doesn't allow to kill the physical background without rejecting also a not negligible amount of possible dark photon signal.

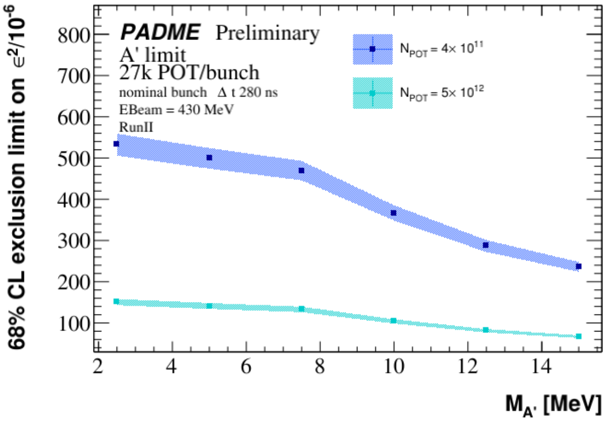

Figure 2.17: *Limits at 68% C.L. on ϵ^2 as a function of the A' hypothesis mass obtained counting events in 2σ around the expected peak position of M^2_{miss}. In blue the limits obtained with the analysed statistic ($N_{POT} = 4\times10^{11}$) are reported. In azure the limits with all RunII statistics of $N_{POT} = 5\times10^{12}$.*

A

Annihilation measurement fits

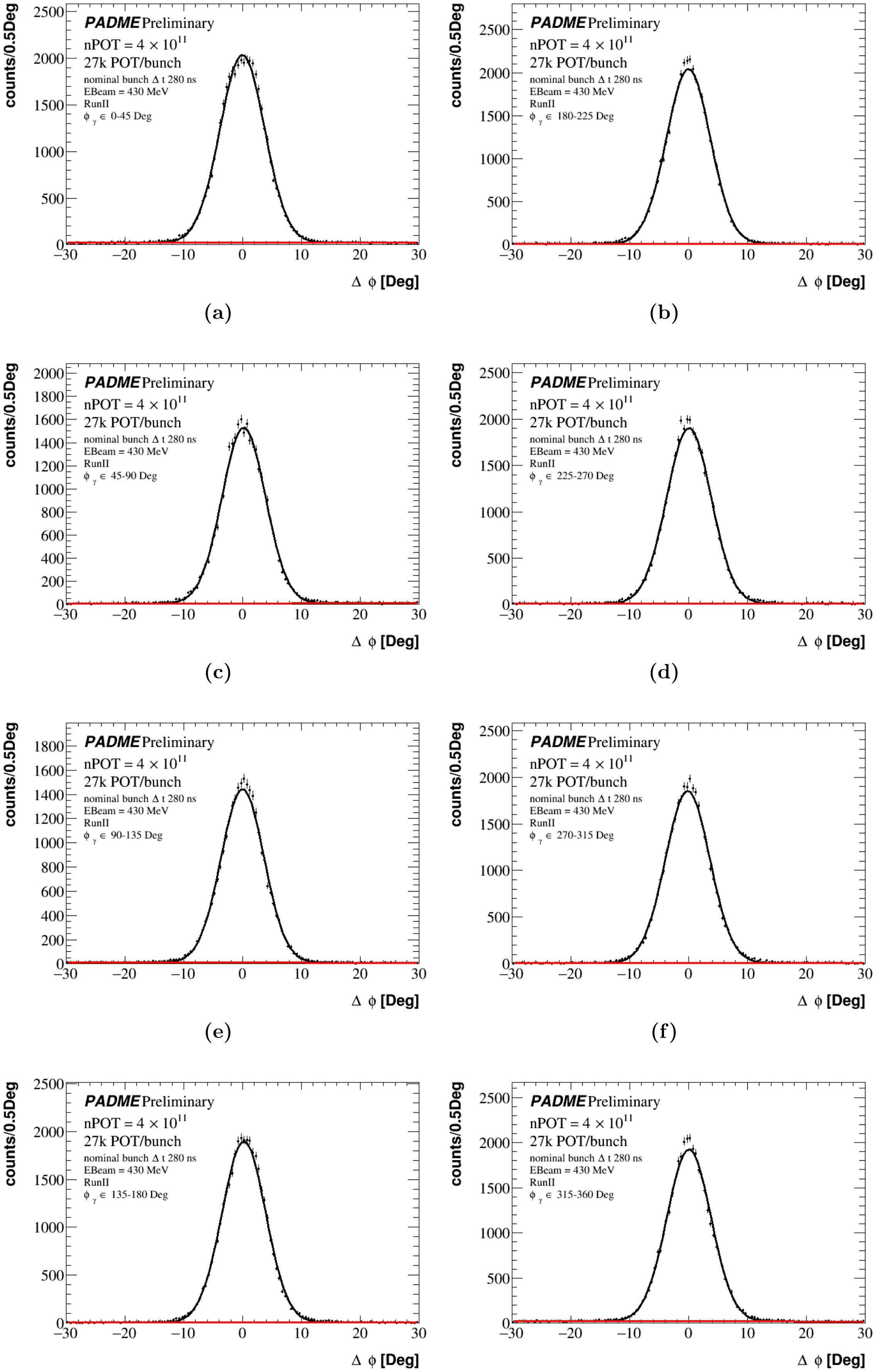

(a) (b) (c) (d) (e) (f) (g) (h)

Figure A.1: *Fit on $\Delta\phi$ distribution for each phi slice.*

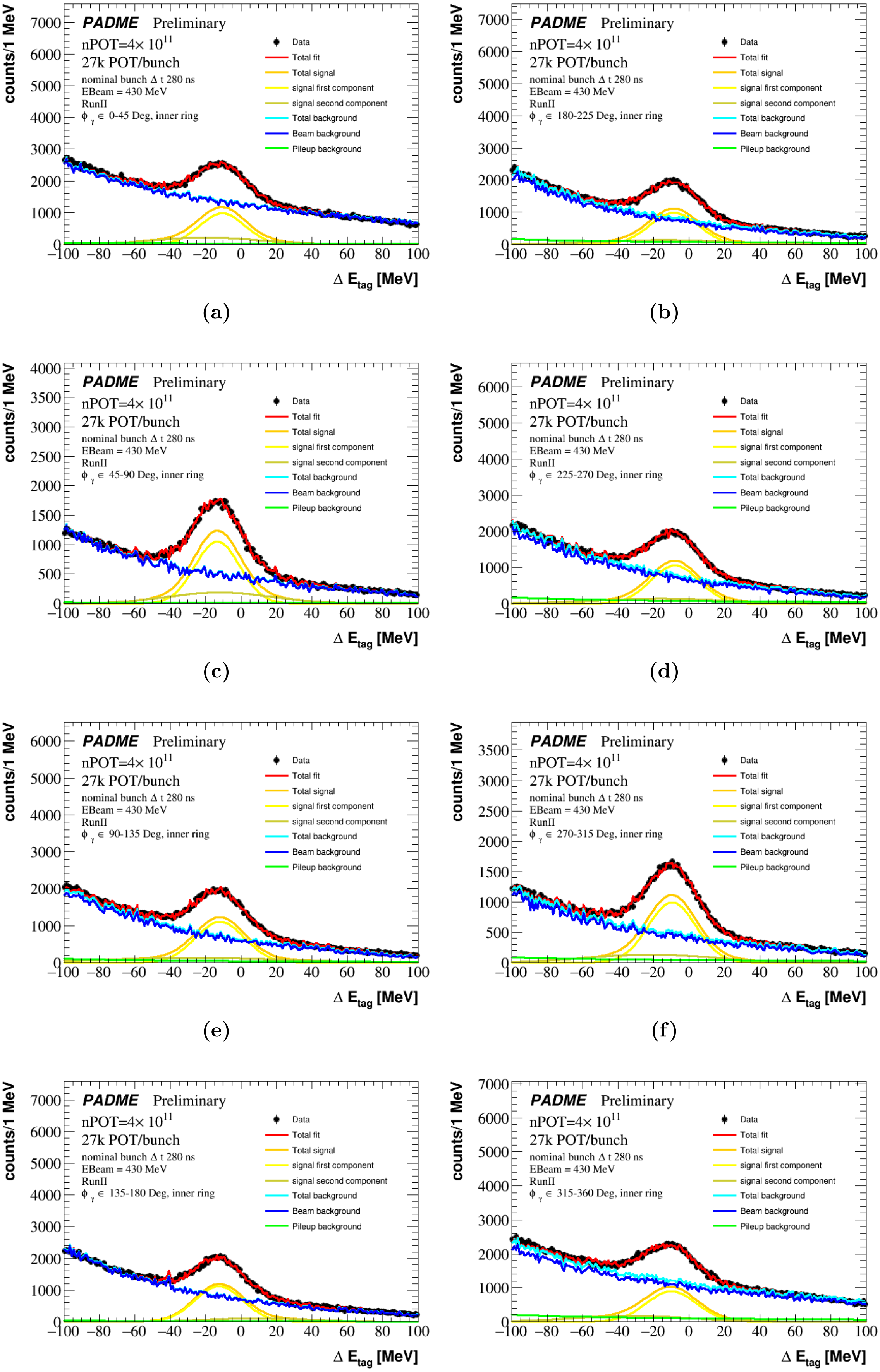

(a) (b)

(c) (d)

(e) (f)

(g) (h)

Figure A.2: *Fit on inner ΔE_{tag} distribution for each phi slice.*

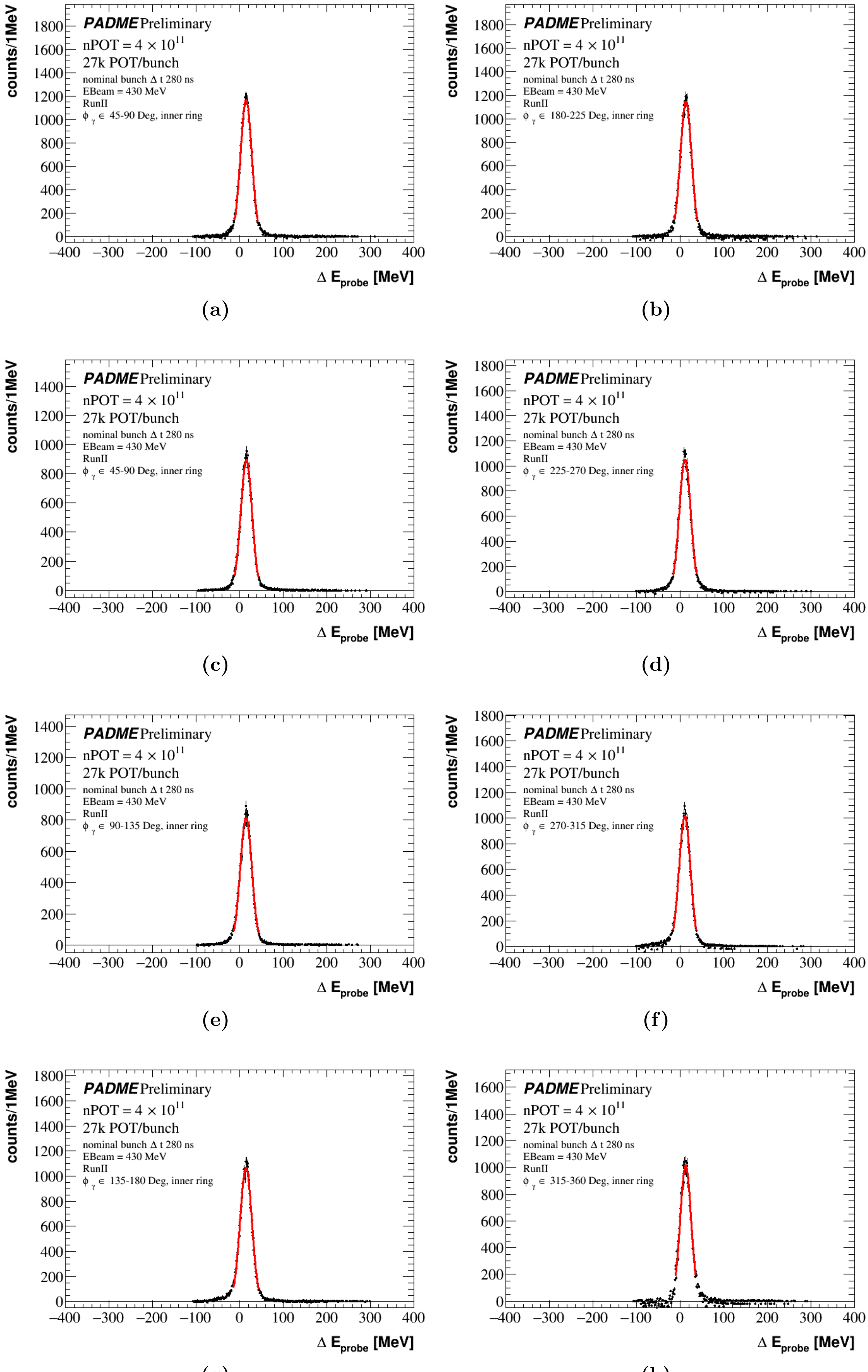

(a) (b)

(c) (d)

(e) (f)

(g) (h)

Figure A.3: *Fit on inner* ΔE_{probe} *distribution for each phi slice.*

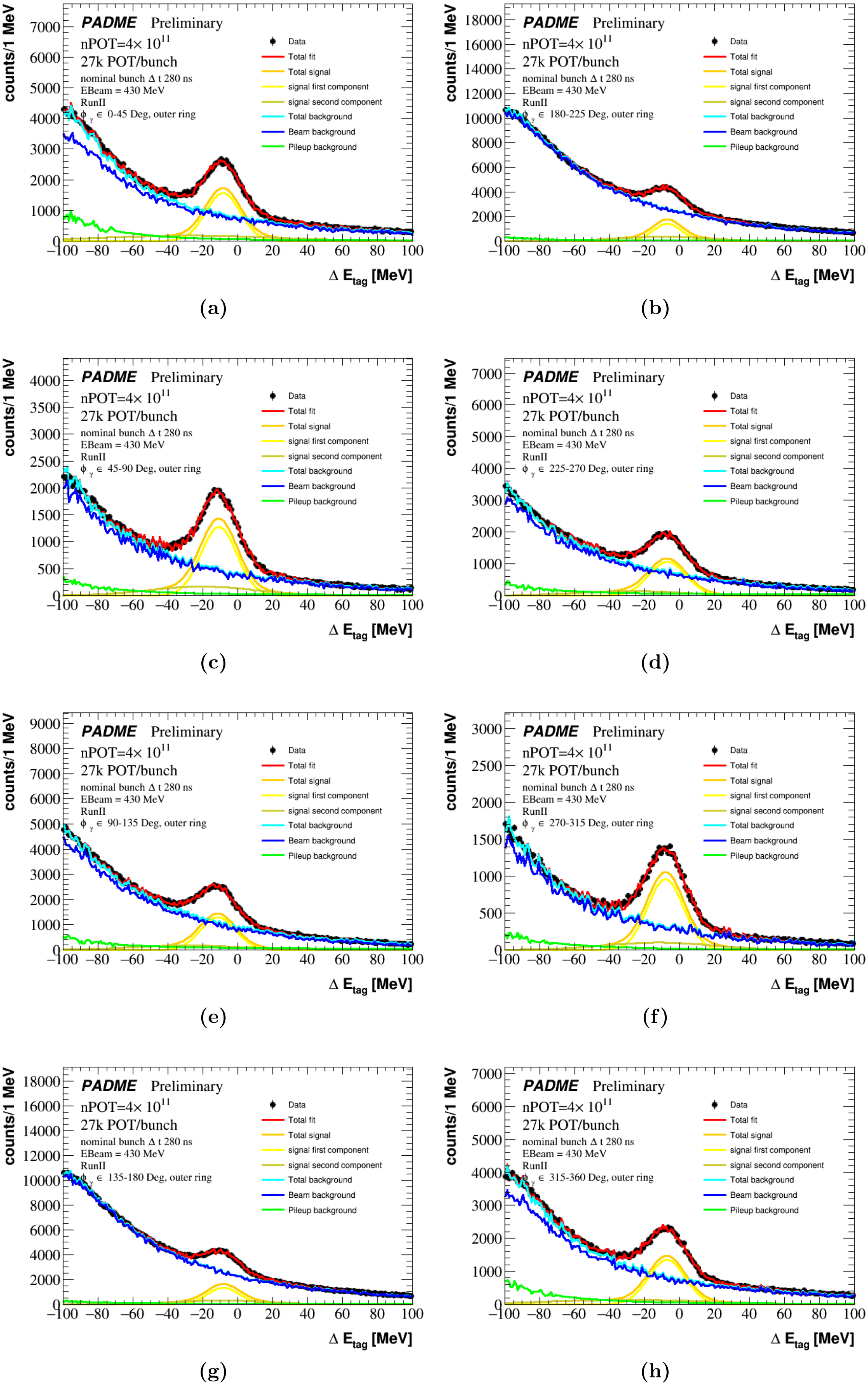

(a) (b) (c) (d) (e) (f) (g) (h)

Figure A.4: *Fit on outer ΔE_{tag} distribution for each phi slice.*

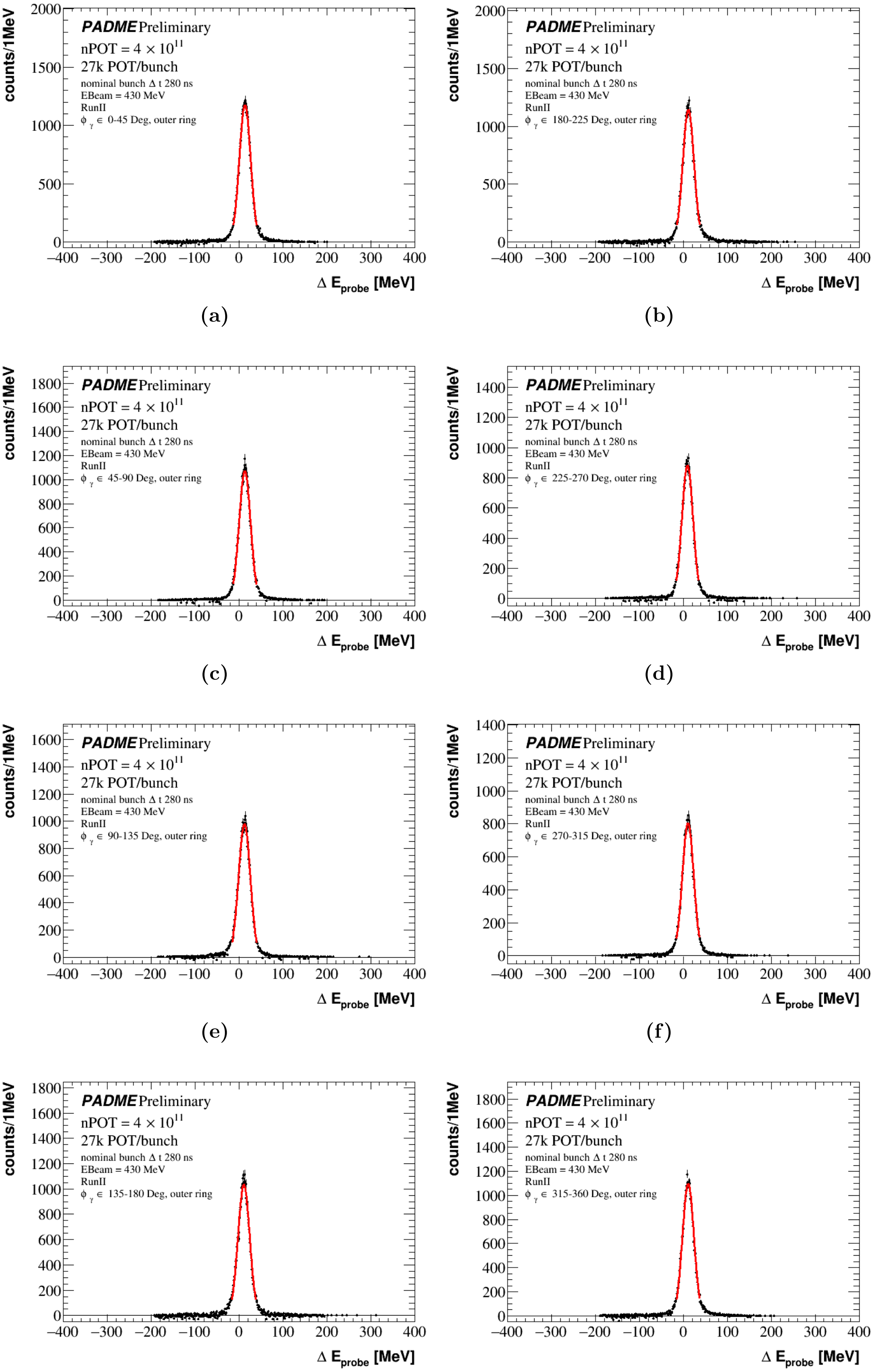

(a) (b) (c) (d) (e) (f) (g) (h)

Figure A.5: *Fit on outer ΔE_{probe} distribution for each phi slice.*

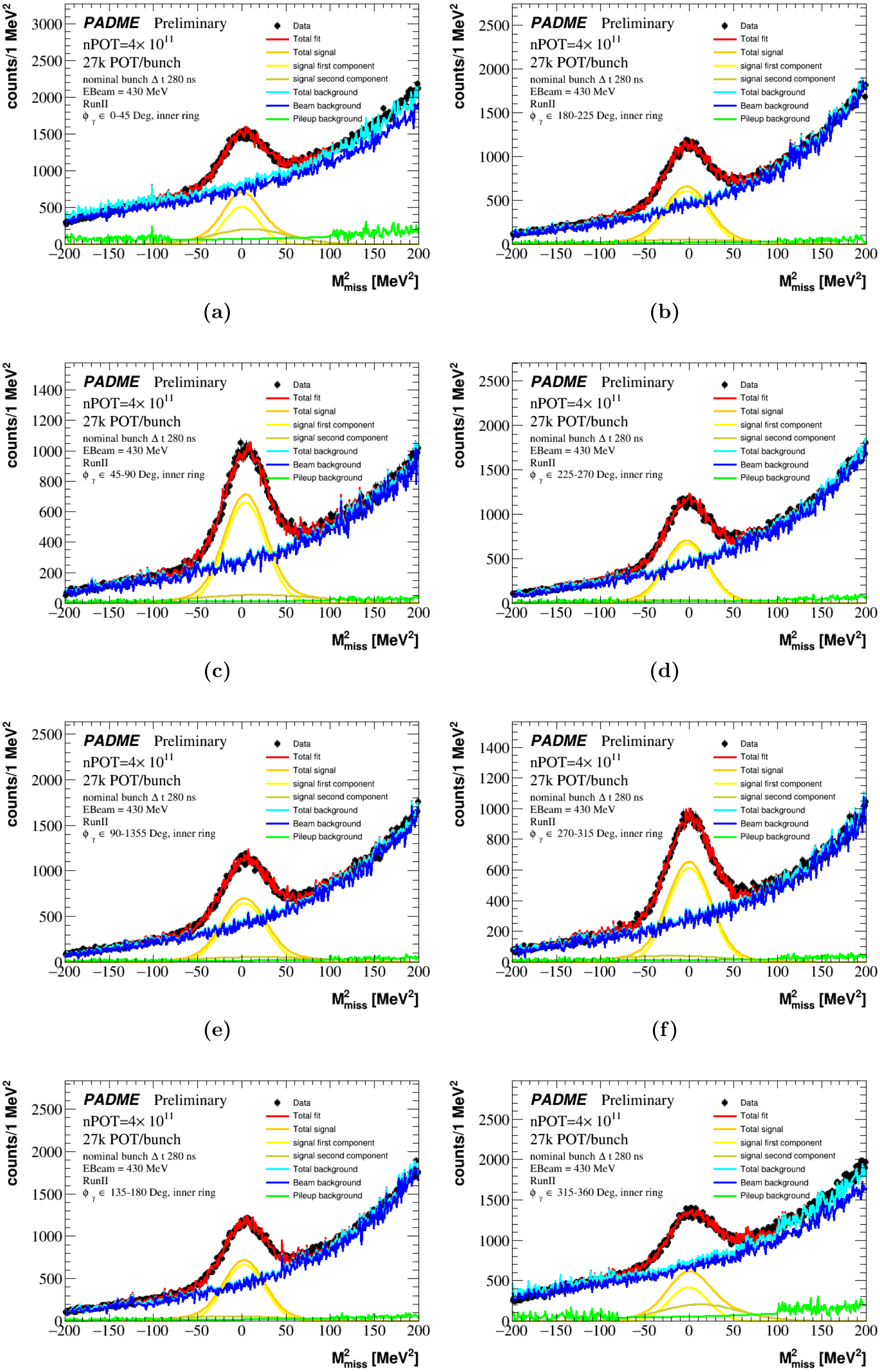

(a) (b) (c) (d) (e) (f) (g) (h)

Figure A.6: *Fit on inner M^2_{miss} distribution for each phi slice.*

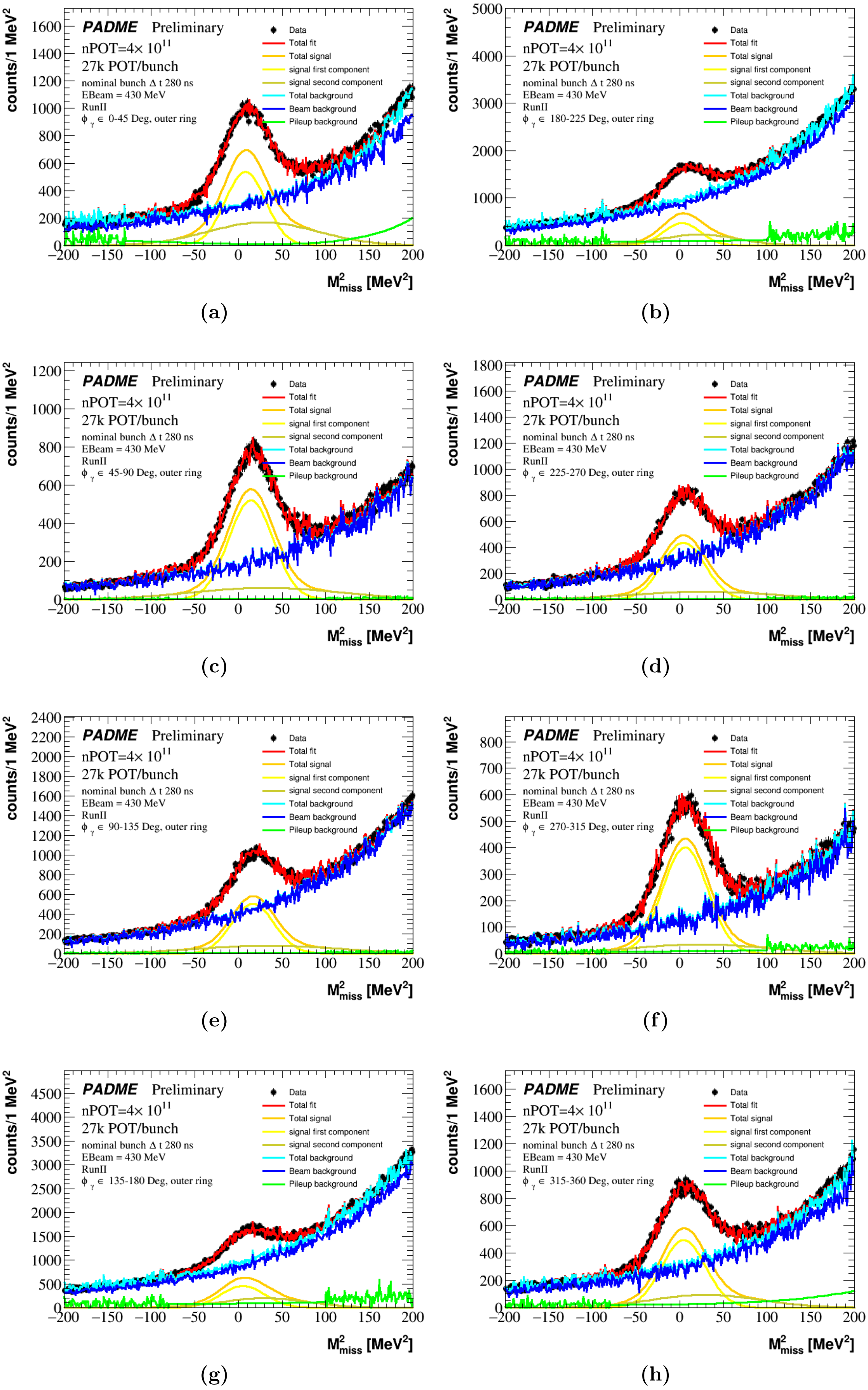

(a) (b)

(c) (d)

(e) (f)

(g) (h)

Figure A.7: *Fit on outer M^2_{miss} distribution for each phi slice.*

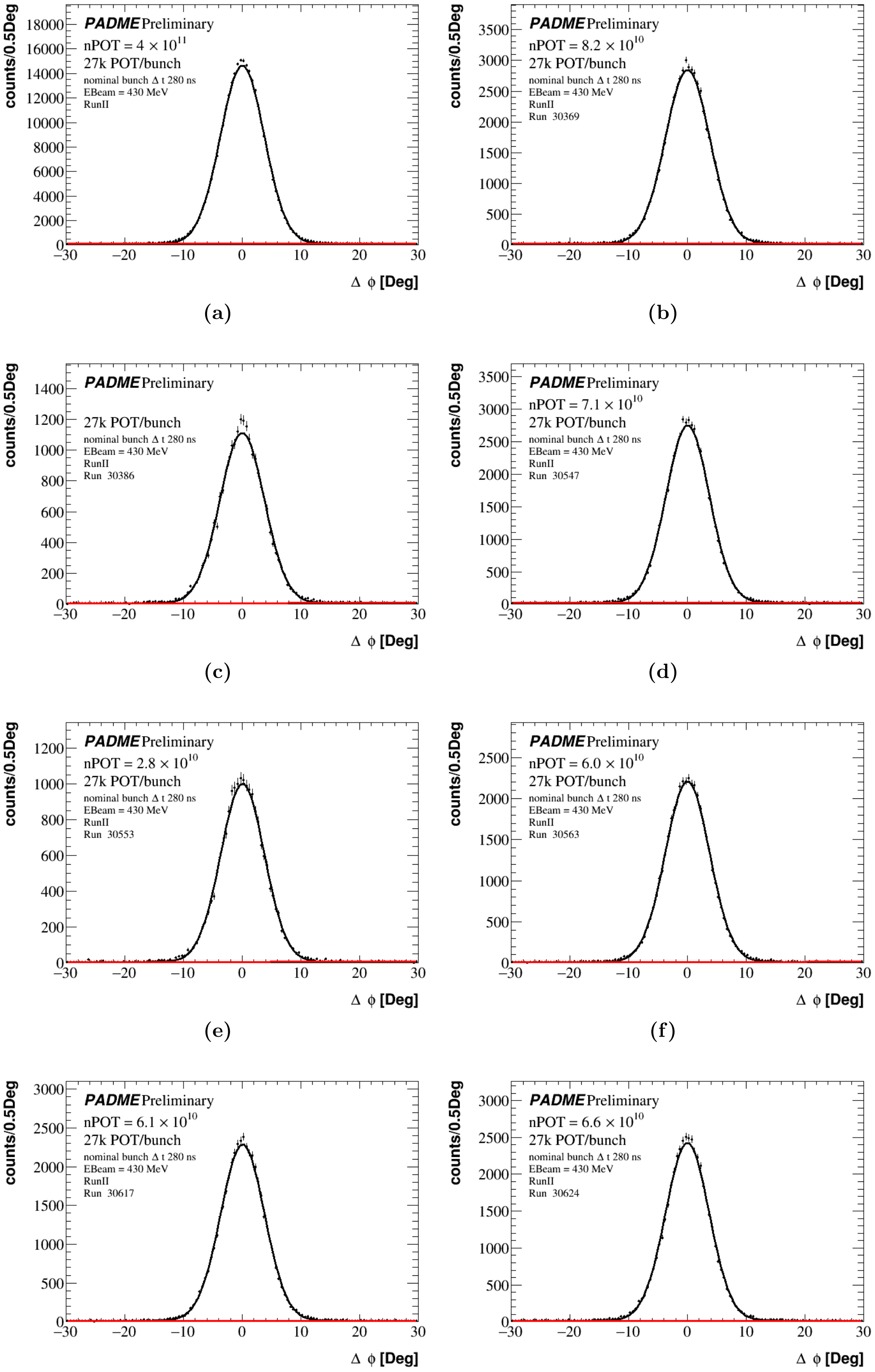

(a) (b) (c) (d) (e) (f) (g) (h)

Figure A.8: *Fit on $\Delta\phi$ distribution for each run.*

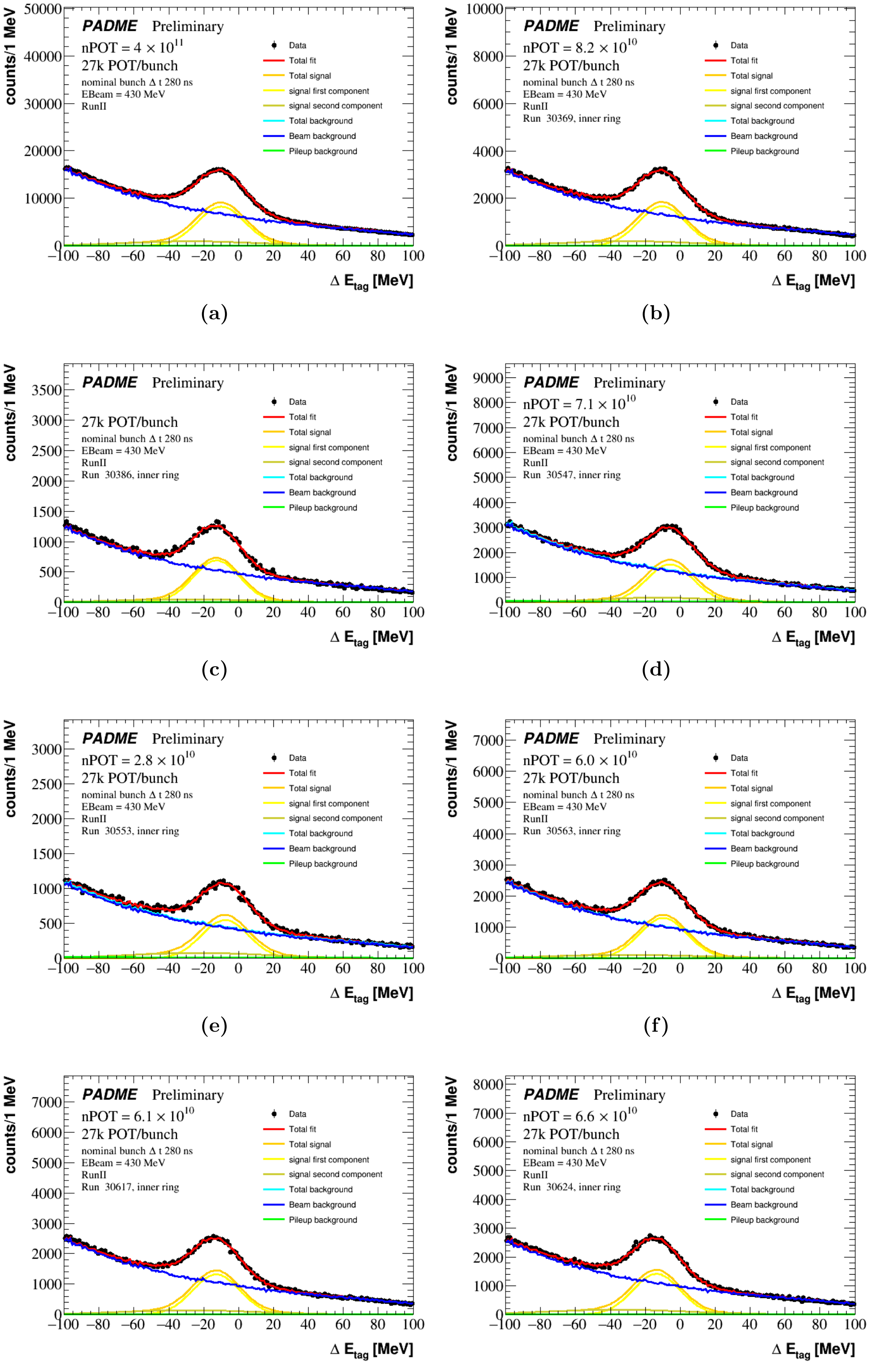

(a) (b) (c) (d) (e) (f) (g) (h)

Figure A.9: *Fit on inner ΔE_{tag} distribution for each run.*

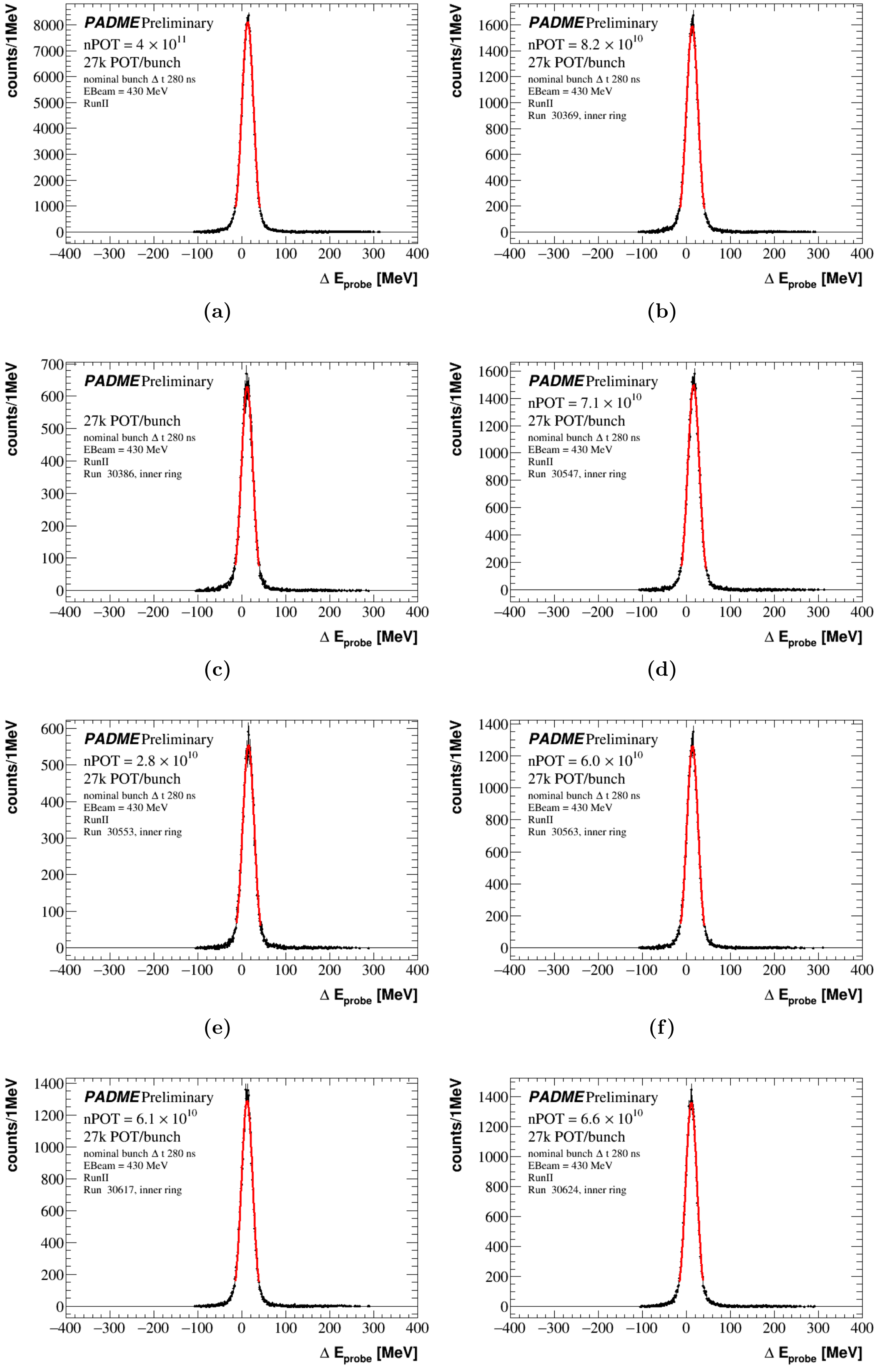

(a) (b) (c) (d) (e) (f) (g) (h)

Figure A.10: *Fit on inner* ΔE_{probe} *distribution for each run.*

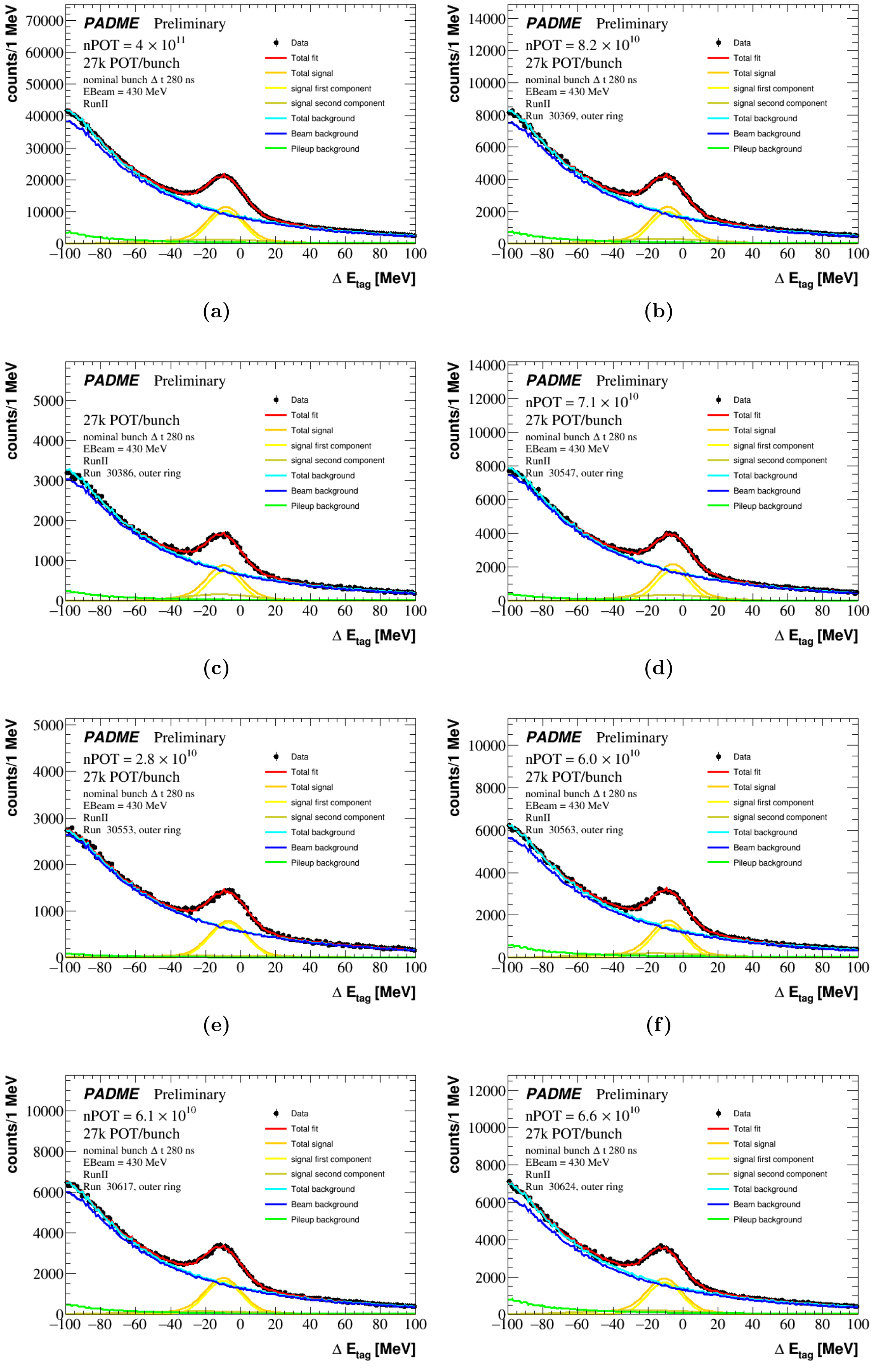

(a) (b)

(c) (d)

(e) (f)

(g) (h)

Figure A.11: *Fit on outer ΔE_{tag} distribution for each run*

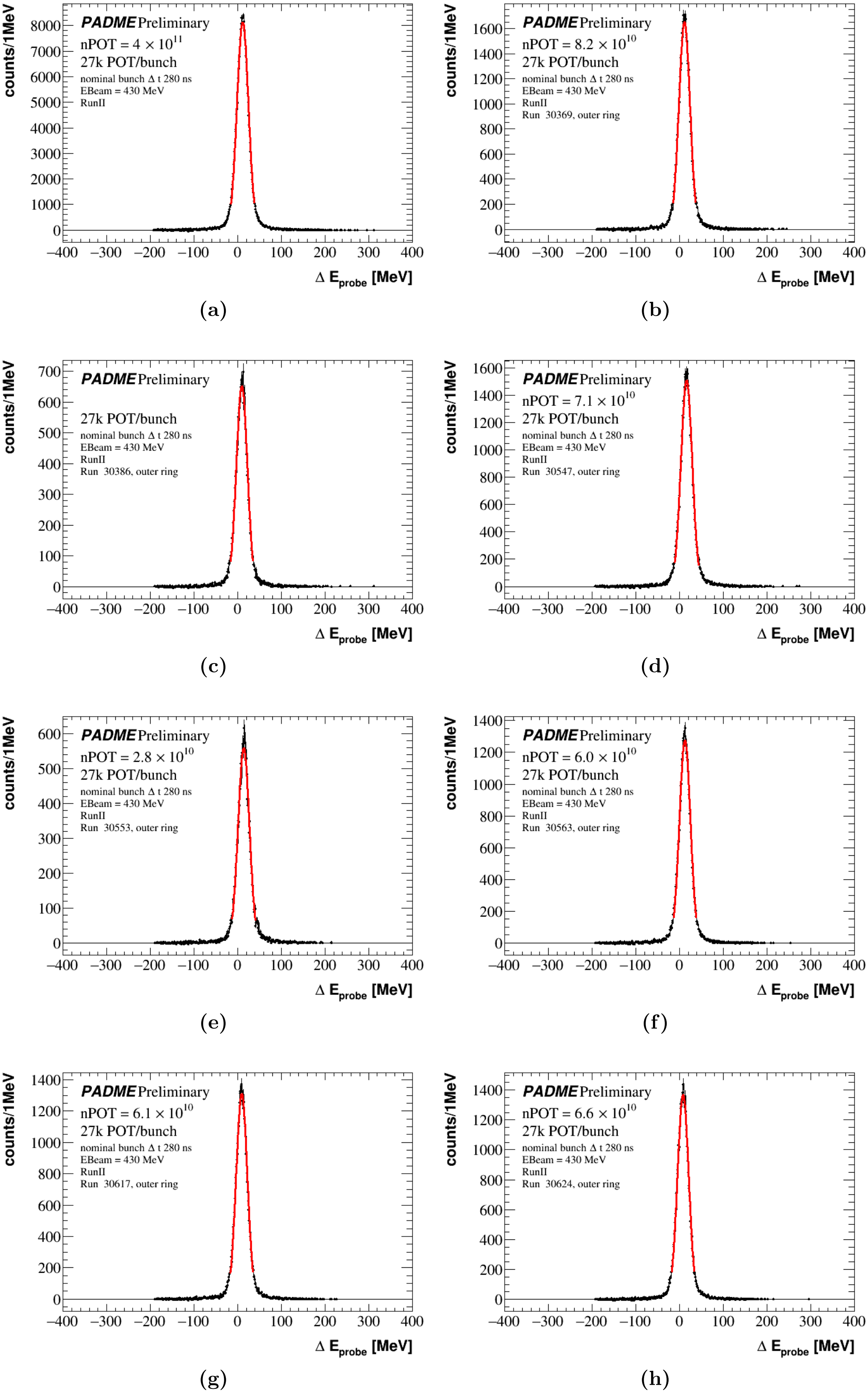

(a) (b) (c) (d) (e) (f) (g) (h)

Figure A.12: *Fit on outer ΔE_{probe} distribution for each run.*